University of Alberta

ENHANCED AIRWAY DEPOSITION OF HIGH ASPECT RATIO PHARMACEUTICAL AEROSOLS THROUGH MAGNETIC FIELD ALIGNMENT FOR LOCALIZED TARGETING WITHIN THE LUNG

by

Andrew Robert Martin ©

A thesis submitted to the Faculty of Graduate Studies and Research
in partial fulfillment of the requirements for the degree of

Doctor of Philosophy

Department of Mechanical Engineering

Edmonton, Alberta
Fall 2008

Library and
Archives Canada

Published Heritage
Branch

395 Wellington Street
Ottawa ON K1A 0N4
Canada

Bibliothèque et
Archives Canada

Direction du
Patrimoine de l'édition

395, rue Wellington
Ottawa ON K1A 0N4
Canada

Your file Votre référence
ISBN: 978-0-494-46380-2
Our file Notre référence
ISBN: 978-0-494-46380-2

NOTICE:
The author has granted a non-exclusive license allowing Library and Archives Canada to reproduce, publish, archive, preserve, conserve, communicate to the public by telecommunication or on the Internet, loan, distribute and sell theses worldwide, for commercial or non-commercial purposes, in microform, paper, electronic and/or any other formats.

The author retains copyright ownership and moral rights in this thesis. Neither the thesis nor substantial extracts from it may be printed or otherwise reproduced without the author's permission.

AVIS:
L'auteur a accordé une licence non exclusive permettant à la Bibliothèque et Archives Canada de reproduire, publier, archiver, sauvegarder, conserver, transmettre au public par télécommunication ou par l'Internet, prêter, distribuer et vendre des thèses partout dans le monde, à des fins commerciales ou autres, sur support microforme, papier, électronique et/ou autres formats.

L'auteur conserve la propriété du droit d'auteur et des droits moraux qui protège cette thèse. Ni la thèse ni des extraits substantiels de celle-ci ne doivent être imprimés ou autrement reproduits sans son autorisation.

In compliance with the Canadian Privacy Act some supporting forms may have been removed from this thesis.

While these forms may be included in the document page count, their removal does not represent any loss of content from the thesis.

Conformément à la loi canadienne sur la protection de la vie privée, quelques formulaires secondaires ont été enlevés de cette thèse.

Bien que ces formulaires aient inclus dans la pagination, il n'y aura aucun contenu manquant.

Canada

Science requires both the rebel and the conservative… The trick seems to be to bring the rebel and the conservative into lifelong and uncomfortable proximity, within the community and, to some extent, within each individual as well.

— Lee Smolin, *The Trouble with Physics*

ABSTRACT

The work described in this thesis investigated the possibility that respiratory tract deposition of inhaled, high aspect ratio aerosol particles could be influenced through control of particle orientations, for the purpose of targeting aerosol drug delivery to specific locations within the lung. Initial experiments were conducted to demonstrate that high aspect ratio cromoglycic acid particles loaded with iron oxide nanoparticles would align with magnetic field lines. Collection of the iron oxide loaded particles on polycarbonate membrane filters increased with a low gradient magnetic field applied parallel to the face of the filters, and alignment of the particles in the direction of field lines was clearly visible in scanning electron micrographs of the filters. Further, more demanding, experiments were then conducted in a physical model of the small, bifurcating airways found in the lung. These experiments provided proof that magnetic alignment of high aspect ratio particles can be used to increase their deposition in small airway bifurcations.

Supplementary bench experiments were conducted to examine the delivery of high aspect ratio powders of ciprofloxacin, a broad-spectrum antibiotic, and paclitaxel, a chemotherapeutic agent, from a commercial dry powder inhaler. Powders were studied with and without the addition of iron oxide nanoparticles. The results of the experiments were mixed; while the measured lung doses penetrating a model mouth-throat geometry were reasonably high, these doses included significant fractions of agglomerates, which no longer exhibited the elongated nature of the individual particles.

Finally, experiments were performed to investigate the feasibility of measuring regional lung deposition of inhaled iron oxide nanoparticles using MRI. Mice were exposed nose-only to nebulized superparamagnetic iron oxide nanoparticles, and regional concentrations of iron in the left and right lung were quantified by measuring the longitudinal relaxation times (T_1) of the lung tissue in exposed mice, compared to a baseline group. In addition, a very small pilot study was conducted in mechanically ventilated rabbits exposed intratracheally to iron oxide loaded cromoglycic acid particles, demonstrating combined targeting by magnetic alignment and subsequent assessment using MRI. Such an approach shows considerably promise for future treatment of localized lung disease.

To my wife, Lisa, for her love and laughter.

ACKNOWLEDGEMENTS

Throughout my graduate studies, I have had the opportunity to work with, and learn from, a large number of talented researchers at the University of Alberta. Dr. Warren Finlay has been a supervisor and mentor to me for the past six years, and without his guidance, instruction, and support the work presented in this thesis would not have been possible. In planning and carrying out my research, I have benefited greatly from discussions with numerous members, past and present, of the Aerosol Research Laboratory of Alberta. In particular, my thanks go to Helena Orszanska, who made essential contributions to the experimental work described in the thesis, and who patiently answered my many questions in various areas of chemistry and pharmacy.

I would also like to thank Dr. Richard Thompson for performing all the MRI scans during the animal experiments, as well as sharing his expertise in image processing; Dr. Ming Chen for producing excellent SEM and TEM images; Nicole Olivier for providing training and advice during the mouse experiments; Dirk Kelm for machining the airway array; and Drs. Bernard Thébaud and Paul Waszak for their collaboration in the rabbit experiments. In addition, Dr. Finlay, Dr. Thompson, Dr. H.K. Chan, Dr. Carlos Lange, Dr. André McDonald, and Dr. Jason Carey all provided feedback after reading draft versions of this thesis, and their collective time and effort are very much appreciated.

Finally, as a graduate student I received funding in the form of student scholarships from the Natural Sciences and Research Council of Canada, the Alberta Ingenuity Fund, the Killam Fund, and the University of Alberta. This support is gratefully acknowledged.

TABLE OF CONTENTS

1. Introduction **1**
1.1. Inhaled Pharmaceutical Aerosols........ 1
1.2. Localized Targeting of High Aspect Ratio Particles........ 3
1.3. Lung Cancer and Inhaled Chemotherapy........ 5
1.4. Summary of Thesis........ 7

2. Background **10**
2.1. The Motion of an Aerosol Particle........ 10
2.2. Respiratory Tract Geometry........ 16
2.3. Measurement of Respiratory Tract Deposition........ 20
2.4. Modeling Respiratory Tract Deposition........ 24
2.5. Respiratory Tract Deposition of High Aspect Ratio Particles........ 35
2.6. Magnetic Fields in Matter........ 56
2.7. Magnetic Alignment of High Aspect Ratio Particles........ 61

3. Analytical Deposition Model **77**
3.1. Introduction........ 77
3.2. Description of the Model........ 78
3.3. Results and Discussion........ 82

4. Magnetic Alignment and Small Airway Deposition **88**
4.1. Introduction........ 88

4.2. Experimental Methods

4.2.1. Preparation of Drug and Magnetite Suspensions........ 88
4.2.2. Droplet Size Measurements........ 90
4.2.3. Penetration through Polycarbonate Membranes........ 91
4.2.4. Nebulization Efficiency........ 93
4.2.5. Aerosol Particle Size and Concentration........ 94
4.2.6. Design of Small Airway Array........ 97
4.2.7. Small Airway Deposition........ 102

4.3. Results

4.3.1. Droplet Size Measurements........ 104
4.3.2. Penetration through Polycarbonate Membranes........ 106
4.3.3. Nebulization Efficiency........ 109
4.3.4. Particle Size and Concentration........ 111
4.3.5. Small Airway Deposition........ 115
4.4. Discussion........ 120

5. Dry Powders Containing High Aspect Ratio Particles **128**
5.1. Introduction........ 128

5.2. Experimental Methods

5.2.1. Materials........ 131

5.2.2. Cromoglycic Acid/Lactose Powders.. 132
5.2.3. Ciprofloxacin and Paclitaxel Powders...................................... 132
5.2.4. In Vitro Lung Deposition from a Dry Powder Inhaler................. 133

5.3. Results

5.3.1. Cromoglycic Acid/Lactose Powders.. 135
5.3.2. Ciprofloxacin and Paclitaxel Powders...................................... 136
5.4. Discussion.. 145

6. MRI Measurement of Regional Lung Deposition in Animals 149
6.1. Introduction.. 149

6.2. Experimental Methods

6.2.1. Materials and Animals.. 151
6.2.2. Aerosol Exposure.. 152
6.2.3. MRI and Post-Processing... 156
6.3. Results... 159
6.4. Discussion.. 166

7. Discussion of Results and Suggestions for Future Work 172

References 182

LIST OF TABLES

2.1 Airway dimensions, Reynolds numbers, and generation volumes of the symmetric lung geometry of Finlay *et al.* (2000)........ 19
2.2 Deposition of asbestos fibers measured by Sussman *et al.* (1991) in a replicate cast of the first ten lung generations........ 37
2.3 Particle residence times and periods of rotation in the lower airways of the tracheobronchial regional and the alveolar region........ 54

4.1 Penetration efficiencies through 5 μm pore size polycarbonate membrane filters with and without magnetic fields........ 108
4.2 Nebulization efficiencies and run times for cromoglycic acid suspensions with and without magnetite........ 111
4.3 Lognormal particle size distributions and number concentrations for cromoglycic acid and magnetite-loaded cromoglycic acid aerosols........ 115

5.1 Densities, capsule loadings, and emitted, mouth-throat, and lung doses for ciprofloxacin and paclitaxel powders........ 137

6.1 Longitudinal relaxation times and iron concentrations in the right and left lung of rabbits exposed to iron oxide loaded cromoglycic acid aerosol........ 165

LIST OF FIGURES

2.1 A realistic, irregular particle together with its aerodynamic equivalent sphere.... 14
2.2 Total *in vivo* deposition fractions measured in healthy adults during oral breathing.......... 28
2.3 Total *in vivo* deposition fractions measured in a variety of special conditions...... 28
2.4 Mouth-throat and lung deposition fractions predicted for an adult.................... 30
2.5 Tracheobronchial and alveolar deposition fractions predicted for an adult 34
2.6 Coordinate system for a prolate ellipsoid moving with respect to the surrounding fluid.......... 40
2.7 The ratio between the fluid resistance forces acting perpendicular (lift) and parallel (drag) to a high aspect ratio particle.......... 42
2.8 The ratio between equivalent spherical aerodynamic diameter and actual particle diameter.......... 45
2.9 Slip correction factors for motion parallel and perpendicular to a particle's major axis.......... 47
2.10 Deposition of a high aspect ratio particle due to interception is shown schematically.......... 49
2.11 Schematic of a prolate ellipsoid in a linear shear flow.......... 51
2.12 The rotational Peclet number plotted versus particle aspect ratio for different particle diameters.......... 55
2.13 Gilbert model and Ampère model for a magnetic dipole.......... 58
2.14 The magnetic field produced by an ideal dipole, and alignment of dipoles perpendicular and parallel to a surface.......... 64
2.15 An illustration of the *H*-fields inside and outside of a high aspect ratio magnetic particle.......... 65
2.16 Schematic of the orientation of a prolate ellipsoid with respect to a linear shear flow.......... 69
2.17 The ratio between the magnetic torque, using the methods described by Skomski *et al.* (2007), and aerodynamic torque for prolate ellipsoids loaded with smaller, spherical magnetite particles.......... 71
2.18 A simple model of ideal magnetic dipoles embedded in a carrier particle........... 72
2.19 The ratio between the magnetic torque, and aerodynamic torque for carrier particles loaded with smaller, spherical magnetite particles.......... 75

3.1 Deposition probabilities for high aspect ratio particles of varying length and diameter in an airway bifurcation representing the branching between lung generations 9 and 10.......... 83
3.2 Identical to figure 3.1, but for lung generations 14 and 15.......... 84
3.3 Identical to figures 3.1 and 3.2, but for lung generations 19 and 20.......... 85
3.4 Deposition probabilities due to individual deposition mechanisms for an elongated particle in different lung generations.......... 86

4.1 TEM image of a co-suspension of cromoglycic acid (CA) and magnetite.......... 89
4.2 Schematic of the experimental setup for measuring nebulizer droplet size distributions using phase Doppler particle analysis.......... 91

4.3 An apparatus for measuring the aerosol deposition in an array of small airway bifurcations.. 95
4.4 Scale drawing of the bifurcation design.. 98
4.5 a) Side view of semicircular cross-section, bifurcating channels cut into a strip of aluminum. b) Top view of the airway array formed by stacking the aluminum strips.. 100
4.6 SEM image of CA particles collected onto a 0.2 μm polycarbonate membrane filter.. 105
4.7 Cumulative, normalized volume distributions for droplets produced by the jet nebulizers containing suspensions of CA... 106
4.8 Penetration efficiency through 5 μm pore size polycarbonate membrane filters is plotted against challenge mass for CA and CA/magnetite aerosols.................. 107
4.9 CA particles loaded with magnetite captured in the pores of a 5 μm pore size polycarbonate membrane... 110
4.10 Identical to figure 4.9b, but at higher magnification.................................... 110
4.11 An SEM image of CA particles used in determining length and diameter distributions... 112
4.12 Identical to figure 4.11, but with all sized particles marked with a black dot....... 113
4.13 Cumulative, normalized volume distributions in diameter and length for CA and CA/magnetite aerosols.. 116
4.14 Particle length versus diameter for CA aerosol, and CA/magnetite aerosol......... 117
4.15 The measured magnetic flux density over the region of space containing airways... 118
4.16 Deposition efficiency in the small airway model for CA aerosol, and for magnetite-loaded CA with and without the magnetic field............................ 119

5.1 Schematic of elongated particles with packing arrangements expected to be relatively easy, or difficult, to disperse.. 130
5.2 The percentages of the nominal (capsule) dose of CA emitted from the Aerolizer inhaler, depositing in the mouth-throat geometry... 136
5.3 The mass of ciprofloxacin on filters measured by gravimetry is compared with measurements of the mass recovered from the same filters by UV spectrophotometry.. 139
5.4 Capsule loadings, emitted doses, and estimates of the *in vitro* lung dose measured using the idealized mouth-throat geometry and an Andersen impactor are compared for the as-supplied ciprofloxacin powder.................................. 139
5.5 Filter samples of as-supplied and lyophilized paclitaxel and ciprofloxacin......... 141
5.6 A scanning electron microscope image of magnetite loaded ciprofloxacin particles penetrating the mouth-throat geometry... 143
5.7 Identical to figure 5.6, but at higher magnification.. 144
5.8 TEM image of ciprofloxacin loaded with magnetite.. 144

6.1 Schematic of the ventilator circuit used to expose rabbits to iron oxide loaded CA aerosol.. 154
6.2 Signal intensity images (for Ti = ∞) of twelve axial slices of the lung of a baseline mouse... 160

6.3 Signal intensity images (for Ti = ∞) of a specified region of interest before and after gray level thresholding to remove the vasculature.................................. 161
6.4 Average T1 relaxation times in the lungs of the baseline mice are plotted against the time after death at which the MRI scan was performed............................. 162
6.5 Concentrations of iron in the right and left lung, averaged over the six exposed mice, are plotted against the axial distance... 163
6.6 Aerodynamic size distributions weighted by mass of iron and mass of CA, as determined by cascade impaction for the iron oxide loaded CA aerosol............. 165
6.7 T_1 maps in apical, medial and basal slices of the lung for one of the targeted, exposed rabbits... 167

1. INTRODUCTION

1.1 Inhaled Pharmaceutical Aerosols

Recent reviews of respiratory drug delivery list numerous afflictions that might be better treated in years to come through the inhalation of pharmaceutical aerosols (e.g. Labiris and Dolovich, 2003; Chow *et al.*, 2007; Patton and Byron, 2007). Certainly, this excitement is well founded. While the inhalation route is currently preferred in management of asthma and chronic obstructive pulmonary disease (COPD), it is likely that pharmaceutical aerosols will be used to treat a growing variety of respiratory ailments in the future. Inhalation offers direct access to the lung, potentially limiting both the amount of drug required to achieve a given clinical outcome and the level of exposure of the rest of the body to that drug. In addition, inhalation has been widely explored for systemic drug delivery. The lung allows fast and relatively complete absorption, compared with the gastrointestinal route, of many small molecules (Brown and Schanker, 1983; Schanker *et al.*, 1986), and is permeable to at least some peptides and proteins (Patton and Byron, 2007), enabling these macromolecules to enter the bloodstream without the need for injection.

The therapeutic and commercial success of inhaled bronchodilators and corticosteroids in the treatment of asthma has been well documented. It should be noted, however, that these two classes of drug generally exhibit large therapeutic indices when inhaled (Clark and Lipworth, 1997; Israel, 2000), meaning that therapeutic effects occur at much lower doses than adverse effects. Accordingly, drug developers have benefited from a large dosing window; effective doses can be overshot without severe consequence, and large intersubject and intrasubject variability in dosing has relatively minor effect on patient outcomes.

As the inhalation route is explored for a variety of more novel treatments, it is unlikely that drugs with such favorable dose-response relationships will be identified in all cases. Therefore, tighter control over dosing will be necessary, and further innovation in aerosol drug delivery will be required. For pharmaceutical aerosols, the dose of drug delivered to the lung is primarily determined by deposition of aerosol particles onto airway walls, after which drug absorption and translocation due to clearance mechanisms play secondary, though important, roles. Control of aerosol particle size and density is known to allow a certain amount of broad targeting of aerosol deposition between central and peripheral regions of the lung (ICRP 1994; Finlay 2001). Broadly targeting deposition in such a manner to airways either more or less distal to the trachea, depending on the site of disease (Zanen and Laube, 2002), is now a widely used approach in optimizing aerosol delivery systems. Unfortunately, the ability to noninvasively target deposition to one side of the lung but not the other, or to one lobe of the lung but not other lobes, remains elusive. One can imagine this second type of targeting being particularly useful in cases where disease is limited to a localized region within the lungs, as is frequently the case for pulmonary infections, and for lung cancer.

1.2 Localized Targeting of High Aspect Ratio Aerosols

In addition to their size and density, the shape of inhaled particles influences those aerodynamic properties which determine the site of deposition within the respiratory tract. Indeed, as will be discussed in detail in subsequent chapters of this thesis, it has been suggested by previous researchers (Chan and Gonda, 1989; Johnson and Martonen, 1994; Zeng *et al.*, 2000; Crowder *et al.*, 2002) that elongated, high aspect ratio particles may be especially well suited for delivery to the lung periphery. In terms of its ability to follow flow streamlines around bends in the airways, an elongated particle behaves in nearly an identical fashion to a spherical particle with diameter equal to the elongated particle's smaller dimension, or diameter. The particle's longer dimension, or length, has very little effect on this equivalent spherical diameter. Moreover, the tendency of elongated particles to align with their longer axes parallel to streamlines (Jeffery, 1922; Harris and Fraser, 1976; Balashazy *et al.*, 1990) prevents them from catching on airway walls, further limiting the effects of their length on deposition. As a result, it has been proposed that the diameters of elongated particles be chosen in the range of approximately 1-5 µm, in order to target the peripheral lung, but that particle lengths be extended so as to increase the mass of drug delivered to that region (Johnson and Martonen, 1994).

While the approach outlined above could improve broad targeting to the peripheral airways, it still does not permit localized targeting to the left or right lung, nor to individual lobes. This latter type of targeting is the focus of the work described in the present thesis. Like their spherical equivalents, high aspect ratio particles with diameters in the range of several hundred nanometers exhibit low deposition efficiencies in the lung. These particles traverse the lung passively, entering upon inhalation and, by and large, exiting upon exhalation. As described above, alignment of the particles with flow streamlines, that is, parallel to airway walls, limits their probability of interception with those walls. However, rotation of the particles away from this predominant, flow-induced orientation would increase their probability of interception, which in turn would increase their deposition efficiency. Furthermore, if the orientations of the particles could be controlled only in a specified region of the lung, the expected increase in deposition by interception would allow localized targeting to that region.

Alignment of high aspect ratio aerosols using magnetic fields has been demonstrated previously by Timbrell (1972) for the purpose of examining effects of non-spherical particle orientation in light scattering experiments. Given their very low attenuation in body tissues, low frequency magnetic fields could conceivably be used to control particle orientations within the lung. While the vast majority of drug and excipient compounds used in pharmaceutical aerosol formulations have very low magnetic susceptibilities, loading drug or excipient particles with smaller magnetic nanoparticles could improve their response to magnetic fields. This proposal will be explored in much greater detail in the second chapter of this thesis. First, however, in order to highlight a particular application for which localized targeting of inhaled aerosols would be beneficial, a brief diversion will be made to describe the current state of development of inhaled chemotherapy for the treatment of lung cancer.

1.3 Lung Cancer and Inhaled Chemotherapy

The Canadian Cancer Society estimates that in 2007 23,300 Canadians will be diagnosed with lung cancer, and 19,900 will die of it (Canadian Cancer Society/National Cancer Institute of Canada, 2007). Lung cancer remains the leading cause of cancer death among both men and women; one in twelve Canadian men and one in sixteen women are expected to develop lung cancer during their lifetimes (Canadian Cancer Society/National Cancer Institute of Canada, 2007).

Woodward *et al.* (2007) have recently reviewed the cost effectiveness of medical care for non-small cell lung cancer patients aged 65 years and older in the United States between 1983 and 1997. Over that fourteen year time period, average life expectancy after diagnosis increased by less than one month, from 1.52 years in 1983 to 1.57 years in 1997, while inflation adjusted spending rose $20,157 per patient (in 2000 dollars). Furthermore, even in those patients diagnosed early in the progression of disease with a localized cancer confined to one area of the lung, life expectancy increased only modestly, from 3.29 years in 1983 to 3.50 years in 1997. One may conclude from these data that current standard treatments are not working well, and that new therapeutic approaches are very much required.

The lung presents a rather unique opportunity among internal organs, in that it can be accessed noninvasively through the inhalation route. As a result, inhalation of therapeutic agents targets the lung directly, and limits systemic exposure to only that fraction of drug that is absorbed through the lung into the bloodstream (though drug particles filtered in the mouth and throat may be swallowed, and enter the gastrointestinal tract). As mentioned in the previous section, the inhalation route has been explored for local administration of pharmaceutical aerosols to treat a wide variety of lung diseases, including lung cancer. In fact, inhaled chemotherapy was administered to patients as long ago as 1968 (Shevchenko and Resnik, 1968), and has shown promise in more recent years (Tatsumura *et al.*, 1993; Verschraegen *et al.*, 2000; Verschraegen *et al.*, 2004). Very recently, two phase I clinical trials have been completed (Otterson *et al.*, 2007; Wittgen *et al.*, 2007). Otterson *et al.* (2007) administered nebulized doxorubicin to patients with metastatic tumors in the lung. Their study demonstrated that inhaled doxorubicin could be delivered with no significant systemic toxicity, but that pulmonary toxicity, as monitored through pulmonary function tests and radiographic imaging, limited the dose of drug that could be administered. Indeed, Otterson *et al.* (2007) concluded that the risk of pulmonary toxicity is the major obstacle preventing inhaled chemotherapy from moving forward in clinical trials. This is similar to the experience of Wittgen *et al.* (2007), who administered nebulized cisplatin to patients with primary lung cancer or metastatic cancer to the lung. While dose-limiting toxicity was not reached in this study, the majority of observed side effects occurred in the respiratory tract, and the authors noted that these effects might become more severe for doses higher than those used in the study (this is currently being explored in a subsequent trial). Wittgen *et al.* (2007) went on to comment that the low deposition efficiency of drug in targeted areas of the lung, primarily located in the peripheral airways, is a detriment to inhaled chemotherapy. This is interrelated with concerns over pulmonary toxicity, in that, ideally, improved targeting would increase the amount of drug depositing where required for therapeutic effect, while at the same time reducing unwanted deposition, and associated side effects, in non-targeted areas.

Based on the clinical experiences described above, it may be concluded that there is a need to improve the targeting of inhaled chemotherapy beyond what is currently possible using conventional aerosol delivery systems. This need has helped motivate the work described in the present thesis.

1.4 Summary of Thesis

In the present thesis, a new approach to targeting inhaled high aspect ratio particles to specific locations within the lung is described. These particles are loaded with magnetic nanoparticles, so that their orientations can be controlled using an externally applied, uniform, and relatively low strength magnetic field in order to induce deposition onto airway walls.

In chapter 2 of the thesis, background information is presented on the underlying physical mechanisms responsible for deposition of aerosol particles in the respiratory tract, and reviews various approaches to measuring and predicting this deposition. In particular, respiratory deposition of high aspect ratio particles is discussed, as this area has been studied in some depth owing to the health risks associated with inhalation of fibrous aerosols. Additionally, the effects of magnetic fields on the trajectories and orientations of magnetic particles are described, with an emphasis on how these effects might be used to control respiratory deposition.

In chapter 3, an analytical model that predicts airway deposition of high aspect ratio particles is presented. This model is employed to estimate the effect of particle orientation on deposition in various regions of the lung, in order to demonstrate the potential for control over orientation to be used to enhance deposition at targeted sites.

In chapter 4, proof of concept, experimental studies using acicular cromoglycic acid crystals as model high aspect ratio particles are described. First, cromoglycic acid particles loaded with magnetic nanoparticles are shown to align in the direction of magnetic field lines, and this alignment is used to reduce the penetration of the composite particles through polycarbonate membranes. Then, in order to assess the technique in geometries more similar to those found in the desired application, these penetration experiments are repeated in an array of bifurcating airways, with airway dimensions and air flow rates chosen so as to be representative of those found in the small airways of the lung.

With proof of concept experiments completed, chapter 5 concerns the development of inhalable powders containing high aspect ratio particles of drugs that may be suitable for clinical application of the previously described approach to targeting. Powders of both ciprofloxacin, a broad spectrum antibiotic, and paclitaxel, a chemotherapeutic agent used in the treatment of lung cancer, are studied. The lung dose delivered from a commercially available dry powder inhaler is determined *in vitro* for both powders, before and after freeze drying the powders in order to reduce their bulk densities. The freeze drying step is also employed to add magnetic nanoparticles to the powders, as is necessary to facilitate magnetic field alignment.

In chapter 6, a novel approach to measuring regional deposition patterns of inhaled iron oxide nanoparticles using magnetic resonance imaging is described. This approach is studied in mice exposed nose-only to nebulized, colloidal iron oxide. Such a technique could be useful in measuring *in vivo* deposition of the high aspect ratio particles, which already contain iron oxide nanoparticles for the purpose of magnetic alignment, in targeted versus non-targeted areas of the lung. To explore the use of iron oxide nanoparticles for combined targeting and detection by MRI, a very small pilot study was conducted in mechanically ventilated rabbits exposed intratracheally to iron oxide loaded cromoglycic acid particles.

The results obtained in the previous chapters are discussed in Chapter 7, with an emphasis on directions for future research and development. Chapter 7 ends with a brief closing summary of the thesis.

2. BACKGROUND

2.1 The Motion of an Aerosol Particle

The motion of a particle in a fluid is, in many cases, difficult to determine. Complexities arise due to the many different fluid forces that may act on the particle (Crowe *et al.*, 1998), and to interactions of the particle with neighboring particles and nearby boundaries (Happel and Brenner, 1965). Thankfully, the problem simplifies considerably in the case of aerosol particles. So long as the density of the particles is much greater than that of the surrounding air, the drag force acting on the particles will be much larger than all other fluid forces (Finlay, 2001). In addition, the concentration of aerosol particles in air is in most cases sufficiently low that particle-particle interactions can be neglected, and the dynamics of aerosol motion are such that aerosol particles are generally unable to remain in close proximity to a wall for any significant length of time before coming into contact with it (Fuchs, 1964).

In light of these simplifications, the equation of motion of a single aerosol particle may be written as

$$m\frac{\mathrm{d}\vec{v}}{\mathrm{d}t}=\vec{F}_d+\sum\vec{F}_e \qquad (2.1)$$

where m is the particle mass, v is the particle velocity, F_d is the drag force, and the summation occurs over all other external forces, F_e, acting on the particle.

Provided gravity is the only external force present, and under the further assumptions that the particle in question is spherical and the particle Reynolds number is small (*Re* << 1), equation (2.1) may be re-written as

$$m\frac{\mathrm{d}\vec{v}}{\mathrm{d}t} = m\vec{g} - 3\pi d\mu\left(\vec{v} - \vec{v}_f\right) \tag{2.2}$$

where g is the acceleration due to gravity, d is the particle diameter, μ is the fluid dynamic viscosity, and v_f is the fluid velocity.

In equation (2.2), the drag force is determined according to Stokes creeping flow solution for a rigid sphere (Stokes, 1851). While the vast majority of solid aerosol particles will not be perfect spheres, Stokes solution provides a reasonable estimate of the drag force acting on these particles so long as they are compact. (The drag force acting on nonspherical, high aspect ratio particles will be discussed in detail in section 2.5). The additional assumption of low particle Reynolds number is valid for nearly all non-ballistic aerosol particles due to their very small diameters. That said, for higher Reynolds numbers, various empirical equations exist for estimating the drag force acting on a sphere (Crowe *et al.*, 1998), and these can be used as required.

In evaluating the relative influences of particle inertia, gravity, and fluid drag on particle motions, a nondimensional form of equation (2.2) is very useful. With appropriate substitution of dimensionless variables (Finlay, 2001) equation (2.2) becomes

$$Stk\frac{\mathrm{d}\vec{v}'}{\mathrm{d}t'} = \frac{v_s}{U}\hat{g} - \left(\vec{v}' - \vec{v}'_f\right) \tag{2.3}$$

where $\hat{g}$ is a unit vector pointing in the direction of gravity, and primes are used to denote dimensionless variables. In addition

$$Stk = \frac{\rho d^2 U}{18 \mu D} \tag{2.4}$$

is the particle Stokes number, where U is a scale velocity for the fluid flow and D is a characteristic dimension of the geometry containing the flow, and

$$v_s = \frac{\rho d^2 g}{18 \mu} \tag{2.5}$$

is the particle settling velocity.

The importance of the Stokes number defined in equation (2.4) is in its ability to predict the relative influence on a particle's trajectory of particle inertia compared to the resistance of the fluid. Referring to equation (2.3), for $Stk \ll 1$, the inertial term on the left hand side of the equation will be much smaller than the drag force exerted by the fluid (the second term on the right). This means that particles will be well entrained in the flow, in that their trajectories will follow the streamlines of the fluid. If instead $Stk \approx 1$ or larger, particle inertia will be sufficiently large that particle trajectories deviate from fluid streamlines as the streamlines change direction. The mechanism by which particles stray from streamlines in such a manner to come into contact with, and deposit on, walls is known as inertial impaction. As will be discussed in later sections of this chapter, the Stokes number is an important predictor of the likelihood that an aerosol particle will deposit in the airways of the respiratory tract due to inertial impaction.

The particle settling velocity, defined in equation (2.5), also plays an important role in determining particle motions. Again referring to equation (2.3), the dimensionless settling velocity, v_s/U, indicates the relative influence of gravity compared to particle inertia and the drag force. As the Stokes number can be used to predict deposition due to inertial impaction, the settling velocity can be used to predict deposition due to gravitational sedimentation of particles onto walls, which often occurs in the peripheral airways of the lung.

A commonality exists between the Stokes number and the settling velocity, in that both of these parameters vary directly with the term ρd^2. As such, it is a convention in aerosol science to define a single particle property, the aerodynamic diameter, that captures this dependence. The aerodynamic diameter is defined so that

$$\rho_w d_{ae}{}^2 = \rho d^2 \tag{2.6}$$

where ρ_w is the density of water, and d_{ae} is the aerodynamic diameter. The aerodynamic diameter of a particle is the diameter of an idealized spherical particle, with density equal to that of water, which would exhibit identical behavior under the influence of gravity as that given particle. This concept is illustrated in figure 2.1.

The Stokes number and the settling velocity can be written in terms of the aerodynamic diameter by substituting equation (2.6) into equations (2.4) and (2.5), respectively. So long as an aerosol particle is much larger than the mean free path of molecules in air (0.067 μm at standard conditions), and that gravity is the only external force acting on the particle,

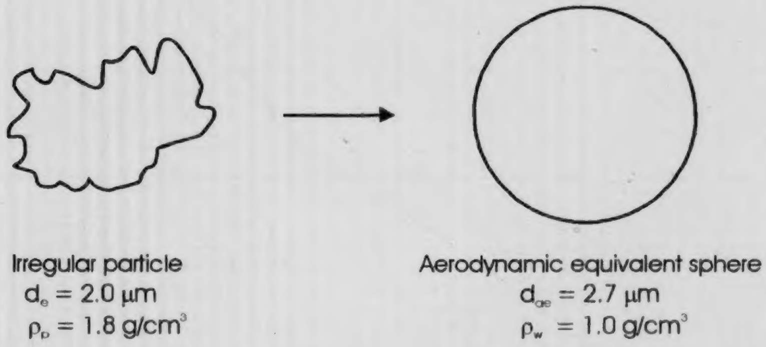

Figure 2.1. A realistic, irregular particle together with its aerodynamic equivalent sphere. From Martin (2004).

its aerodynamic diameter encompasses all particle properties that influence its motion. However, the motion of smaller particles is different in two important ways, neither of which is captured in the aerodynamic diameter. First, as the actual particle diameter (this will henceforth be referred to as the geometric diameter, to differentiate it from the aerodynamic diameter) begins to approach the mean free path of molecules in air, the drag force acting on the particle is reduced, owing to the ability of the particle to 'slip' between neighboring gas molecules in the flow. To account for this reduction, the drag force can be divided by a dimensionless correction factor, known as the Cunningham slip correction factor. This correction carries through to the Stokes number and the settling velocity, so that for small particles equations (2.4) and (2.5) should both be multiplied by the same correction factor. Various empirical equations for the slip correction factor are available (Allen and Raabe, 1985; Rader, 1990; Hinds, 1999), but if the geometric diameter is greater than 0.1 μm the following simple formula can be used (Finlay, 2001)

$$C_C = 1 + 2.52\,\lambda/d \qquad (2.7)$$

where λ is the mean free path of molecules in air.

The second manner in which the motion of small aerosol particles differs from larger particles is in their response to collisions with air molecules. Randomly occurring collisions with molecules displace small particles, causing them over time to follow nondeterministic paths in the well-known process of Brownian diffusion. While the exact paths followed by particles subject to Brownian motion cannot be predicted, it is possible to estimate the net distance over a given time that a particle will be displaced from its initial position. Einstein (1905) calculated this distance to be

$$x_{rms} = \sqrt{2D_d t} \qquad (2.8)$$

where x_{rms} is the root mean square displacement over a time t much larger than the time between collisions, and D_d is the particle diffusion coefficient

$$D_d = \frac{k_B T C_C}{3\pi\mu d} \qquad (2.9)$$

where k_B is Boltzmann's constant, and T is the temperature.

The displacement of aerosol particles due to Brownian diffusion can lead to respiratory tract deposition provided that particle geometric diameters are sufficiently small that such diffusion becomes significant over a particle's residence time in a given airway. For the micrometer scale particles typical of conventional aerosol drug delivery systems, this is generally not the case. However, for particles with at least one dimension in the submicron range (such as the high aspect ratio particles that will be described later in this thesis) diffusion can be expected to play a non-negligible role in determining respiratory tract deposition.

Brownian diffusion, gravitational sedimentation, and inertial impaction are the three primary mechanisms through which inhaled aerosol particles come to deposit onto airway walls in the respiratory tract. Accordingly, much insight into the factors affecting delivery of pharmaceutical aerosols to the lung can be gained through an understanding of these mechanisms. While the particle properties highlighted above are critical in determining regional deposition patterns, equally important is the geometry of the respiratory tract, as is described in the following section.

2.2 Respiratory Tract Geometry

The human respiratory tract is made up of a complicated series of branching, or bifurcating, airways. First and foremost, the function of the lung is to exchange gases between the blood and the atmosphere. Accordingly, the geometry of the respiratory tract has developed, through evolutionary changes, so as to allow the lung to perform this task as efficiently as possible, while at the same time providing adequate protection against foreign materials contained in inhaled air. In this latter task, the extrathoracic airways, made up of the nasal and oral cavities, the pharynx, and the larynx, provide a first line of defense. These airways essentially act as a filter, preventing large aerosol particles (greater than ~10 μm in aerodynamic diameter) from reaching the trachea. In addition, the extrathoracic airways heat and humidify inhaled air to body conditions, so as to avoid evaporation of the airway surface liquid that lines the bronchial tree.

After passing through the extrathoracic region, inhaled air enters the lung through the trachea. The airways of the lung are generally grouped into two distinct regions, with the tracheobronchial region comprised of those conducting airways through which air is transported from the trachea down to the gas-exchange region of the lung, known alternatively as the alveolar or pulmonary region. The tracheobronchial region is best described as a series of bifurcating, cylindrical tubes, lined with a layer of mucous sitting atop cilia which continuously beat in order to move the mucous, and any deposited particles, up to the throat in a process known as mucociliary clearance. Removal of particles through this mucociliary escalator typically occurs over a period of several hours. While no exchange of gases takes place in the tracheobronchial airways, their bifurcations are crucial in providing adequate airway surface area for gas exchange in the alveolar region. Indeed, Horsfield and Cumming (1967) demonstrated that the geometry of the human bronchial tree is, to a large extent, consistent with an optimum, theoretical structure predicted to best compromise between maximizing alveolar surface area and minimizing resistance to flow in the conducting airways.

The tracheobronchial region ends with the terminal bronchioles, which directly supply the respiratory bronchioles of the alveolar region. Moving deeper into the alveolar region, airways become increasingly covered with alveoli (hemi-spherical structures that protrude from the sides of airways, and expand and contract during inhalation and exhalation) until they terminate at the alveolar sacs. It is across the epithelium of these alveoli that exchange of gases between the air and blood takes place. Unlike the tracheobronchial region, the alveolar region is not protected by mucociliary clearance. Instead, alveolar macrophages engulf and clear particles in a process known as cellular phagocytosis (Crystal, 1991). As a result, insoluble particles that reach the alveolar region can remain for days, months, or years depending on their size, shape, and composition, as well as on the number of particles present.

The geometry of the respiratory tract is complex, and efforts to characterize its structures are confounded by tremendous intersubject and intrasubject variability. Nonetheless, a large number of idealized geometric models have been proposed. Phillips *et al.* (1994) have described in detail much of the influential work done in measuring and modeling respiratory tract geometry. Despite its limitations, the most widely adopted lung model remains the highly idealized, symmetric model given by Weibel (1963), and most often referred to as the Weibel A model. Under the Weibel A model, airways are classified by a generation number (beginning with zero at the trachea), which indicates the number of bifurcations separating the airway from the trachea. Airway lengths and diameters become progressively smaller as the generation number increases. Many subsequent models have adopted the general characteristics of the Weibel A model, but propose alternative airway lengths and diameters in order to correct known flaws. Such is the case for the model proposed by Finlay *et al.* (2000), which is adopted at present. This model combines the tracheobronchial airway data of Phillips *et al.* (1994) with the alveolar data of Haefeli-Bleuer and Weibel (1988). Generations 0-14 make up the tracheo-bronchial region, while generations 15-23 comprise the alveolar region. Table 1 gives airway numbers, lengths and diameters for each generation of the Finlay *et al.* (2000) model, as well as the total volume of airways (including alveoli) in each

Table 2.1 Airway Dimensions, Reynolds Numbers, and Generation Volumes of the Symmetric Lung Geometry of Finlay *et al.* (2000)

Generation	Number	Diameter [mm]	Length [mm]	Volume [cm^3]	Re
0	1	18.1	124.5	32.1	1406.9
1	2	14.1	36.1	11.4	903.0
2	4	11.2	28.6	11.2	568.4
3	8	8.85	22.8	11.2	359.7
4	16	7.06	17.8	11.1	225.4
5	32	5.65	11.3	9.0	140.8
6	64	4.54	8.97	9.3	87.6
7	128	3.64	8.28	11.0	54.7
8	256	2.86	7.45	12.2	34.8
9	512	2.18	6.53	12.5	22.8
10	1,024	1.62	5.55	11.8	15.4
11	2,048	1.21	4.54	10.7	10.3
12	4,096	0.92	3.57	9.7	6.76
13	8,192	0.73	2.77	9.5	4.26
14	16,384	0.61	2.19	10.5	2.55
15	32,768	0.49	1.34	21.8	1.59
16	65,536	0.48	1.09	34.9	0.81
17	131,072	0.39	0.91	44.2	0.50
18	262,144	0.39	0.81	73.8	0.25
19	524,288	0.35	0.68	116.2	0.14
20	1,048,576	0.33	0.68	215.8	0.07
21	2,097,152	0.30	0.68	377.8	0.04
22	4,194,304	0.28	0.65	675.0	0.02
23	8,388,608	0.24	0.73	1257.3	0.01

Lengths, diameters, and volumes are as given by Finlay (2001).

Reynolds numbers (Re) are calculated for an inhalation flow rate of 18 l/min.

The dividing line after generation 14 separates the tracheobronchial and alveolar regions.

generation, and airway Reynolds numbers for an inhalation flow rate typical of tidal breathing.

2.3 Measurement of Respiratory Tract Deposition

Given that respiratory tract deposition of inhaled aerosols is important not only in determining the delivered dose of pharmaceutical aerosols, but also in assessing the inhalation health risk of particulate matter in the ambient environment and in the workplace, there exists a relatively large data set of *in vivo* respiratory tract deposition measured in human subjects. Much of this work has been limited to measurement of the total deposition fraction (TDF) of inhaled aerosols throughout all regions of the respiratory tract. The TDF is commonly inferred from measurement of the number concentration of monodisperse aerosols in inhaled versus exhaled air using a laser aerosol photometer. TDF data is currently available in healthy adult subjects over a wide range of breathing conditions and particle sizes, ranging from tens of nanometers to tens of micrometers (Heyder *et al.*, 1986; Kim and Jacques, 2004; Kim and Jacques, 2005; Kim and Hu, 2006). More limited TDF data is available for adults with varying degrees of airway obstruction (Kim and Kang, 1997), during inhalation with alternative carrier gases, such as heliox (Darquenne and Prisk, 2004), and in microgravity and hypergravity (Darquenne *et al.*, 1997). In addition, a few researchers have made TDF measurements in healthy children (Becquemin *et al.*, 1986; Schiller-Scotland *et al.*, 1992; Bennett *et al.*, 2008).

While TDF data has helped shed light on many variables affecting the deposition of inhaled aerosols, it does not differentiate between deposition in the various regions of the respiratory tract. *In vivo* studies of regional deposition using the standard method of gamma scintigraphy are more difficult to conduct because they require subjects to inhale aerosols that have been labeled with radioisotopes. Though the radioisotopes used in such studies have short half-lives, and are considered to be safe, recruitment of volunteers can be difficult, especially if the studies involve children. Despite this difficulty, a considerable number of scintigraphy studies were completed in the late 1970s and early 1980s, measuring regional deposition of monodisperse aerosols under carefully controlled breathing patterns (Lippmann, 1977; Foord *et al.* 1978; Chan and Lippmann, 1980; Stahlhofen *et al.* 1980; Stahlhofen *et al.* 1981; Emmett *et al.*, 1982; Stahlhofen *et al.* 1983). These studies form the backbone of the present collective understanding of regional deposition patterns within the respiratory tract.

One of the limitations of scintigraphy is that gamma camera images of the body are weighted only by gamma rays emitted from radioisotopes, and therefore contain no reference to the locations of internal structures within the body other than those that can be inferred by the researcher. There is usually little difficulty in differentiating between emissions stemming from the lung and those from the extrathoracic airways and stomach (the latter being due to swallowing of radioisotopes originally depositing in the mouth and throat). Accordingly, gamma scintigraphy can provide reasonably accurate measurement of mouth-throat and lung deposition fractions, provided that appropriate corrections are made for tissue attenuation of gamma emissions in the head and body. On the contrary, separation of lung deposition into tracheobronchial and alveolar fractions is not possible using planar gamma camera images, as the boundary between these regions cannot be discerned. The studies cited in the previous paragraph instead compared lung deposition measured immediately following aerosol inhalation with that obtained 24 hours later, under the assumption that particles depositing in the tracheobronchial airways were cleared by the mucociliary escalator within those 24 hours. Lung deposition measured after 24 hours was then assumed to be exclusively alveolar deposition. While these fast-cleared and slow-cleared deposition fractions do shed light on regional deposition patterns within the lung, it is important to note that they are not precisely synonymous with tracheobronchial and alveolar fractions, as an unknown portion of tracheobronchial deposition will not be cleared from the region within 24 hours, particularly for particles a few micrometers or less in diameter (ICRP, 1994).

A more recent approach to measuring regional deposition within the lung has been to employ single photon emission computed tomography (SPECT), in which multiple planar gamma camera images obtained at different angles are combined to form a three-dimensional tomographic reconstruction. While SPECT imaging yields detailed spatial distributions of the inhaled radioisotopes deposited within the respiratory tract, again no information on the actual respiratory tract anatomy is obtained. To achieve an anatomical reference, Fleming *et al.* (2006) have compared SPECT images with magnetic resonance images taken on a separate occasion. Aerosol deposition in various locations of the lung was then mapped to an airway model, based on an assumed spatial distribution of the airways within the lung, in order to estimate deposition at the level of individual generations (Fleming, 2006). While not a direct measurement of deposition in specific airways of the lung, this procedure provides at least an estimation of the distribution of deposited aerosol over different airway generations.

Even if it was possible to obtain detailed information on aerosol deposition in each airway of the lung, the shear number of airways present would make assignment of deposition into individual generations a daunting task. With reference to Table 2.1, the lung contains, literally, many millions of airways. Even to directly identify the boundary between the tracheobronchial and alveolar regions, one would have to locate something on the order of 16,000 terminal bronchioles. With these figures in mind, it seems reasonable to conclude that direct measurement of aerosol deposition in each and every generation of the lung would be extremely difficult, regardless of the imaging method employed. Thus, in sorting measured deposition patterns into airway generations, assumptions must be made. As will be discussed in the following section, this presents a problem in validating the detailed predictions of respiratory tract deposition models, which by and large predict deposition down to the level of individual lung generations. Looking forward, it is possible that some other reference basis, other than airway generations, will have to be established in order to compare modeled versus measured distributions of aerosol deposition within the lung.

Given the difficulty in obtaining *in vivo* deposition measurements in individual airways, many researchers have instead performed experiments *in vitro* in physical replicas of the airways. Indeed, a large number of studies have been performed in replicas of the upper branches of the tracheobronchial airways (e.g. Zhou and Cheng, 2005; Zhang and Finlay, 2005; Robinson *et al.,* 2006), as well as in replicas of the nasal passages (e.g. Cheng, 1995; Haussermann, 2002; Kelly, 2004), and the mouth and throat (e.g. Grgic *et al.*, 2004; Ehtezazi *et al.*, 2005; Sosnowski *et al.*, 2006). Such *in vitro* studies allow researchers to systematically examine effects on deposition of, for example, varying airway geometry, particle properties, or inhaler design under tightly controlled experimental conditions. In this manner, the multitude of factors influencing respiratory tract deposition can be scrutinized in much finer detail than is possible with current *in vivo* approaches. Additionally, *in vitro* methods are frequently employed to study deposition of aerosols that pose potential health risks, and which cannot ethically be studied *in vivo* in human volunteers.

2.4 Modeling Respiratory Tract Deposition

In recent years, a large number of mathematical models have become available for estimating respiratory tract deposition of inhaled aerosols. These models can vary greatly in the physical phenomena they include and exclude, the manner in which they approximate the respiratory tract geometry, and the level to which they subdivide deposition into various regions within that geometry. As with any model of any system, the applicability of the various assumptions and simplifications made in defining these deposition models must be carefully considered in light of each given application before a particular model can be expected to provide meaningful predictions. Before describing respiratory tract deposition models in further detail, it seems prudent to first include some of the general discussion on models and their limitations presented by physicist and author Robert K. Adair in his book describing the physics of baseball (Adair, 1990):

> What we can do is construct plausible models of those interactions that play a part in baseball that do not violate basic principles of mechanics. Though these basic principles – such as the laws of the conservation of energy and momentum – severely constrain such models, they do not completely define them. It is necessary that the models touch the results of observations – or the results of the controlled observations called experiments – at some points so that the model can be more precisely defined and used to interpolate between known results, or to extrapolate from them… However connected with experience, model and system – map and territory – are not the same. The physicist can usually reach precise conclusions concerning the character of the model. If the model is well chosen, so as to represent the salient points of the real system adequately, conclusions derived from an analysis of the model can apply to the system to a useful degree. Conversely, conclusions – although drawn in a logically impeccable manner from premises defined precisely by the model – may not apply to the system if the model is a poor map of the system.

Mathematical models used to predict respiratory tract deposition of inhaled aerosols can, in large part, be sorted by the degree to which they touch the results of experiments. The simpler, empirical, models are those that have been fit directly to a chosen set of experimental data. Examples include the models presented by Rudolf *et al.* (1990), Yu *et al.* (1992), and Kim and Hu (2006). Most often the data set is derived from *in vivo* measurements, such as those referred to in the previous section of this chapter. Algebraic equations are provided through which deposition can be predicted based on various particle and flow parameters, including particle diameter and density, inhalation flow rate, and tidal volume.

As *in vivo* experiments allow only a small amount of regional discrimination, empirical deposition models are largely limited to prediction of total, lung, and extrathoracic deposition fractions, though models that distinguish between fast-cleared and slow-cleared lung deposition are available (Stahlhofen, 1989). Furthermore, empirical models do not generally lend themselves to extrapolation outside of the parameter range of the experimental data to which they have been fit (Finlay, 2001). In order to at least partially circumvent this latter limitation, Martin and Finlay (2007) presented a simple, empirical equation through which the total deposition fraction of inhaled micrometer-scale particles can be predicted based on the values of dynamical, dimensionless parameters governing inertial and gravitational deposition, as well as a dimensionless tidal volume (a parameter governing Brownian diffusion was not included, as diffusion does not in general affect the deposition of particles larger than 1 μm in diameter). This equation was fit to a large set of data in healthy adults breathing through their mouths (Heyder *et al.*, 1986; Kim and Hu, 2006), where particle aerodynamic diameters ranged from 1 to 15 μm, inhalation flow rates ranged from 125 to 1000 cm^3/s, and tidal volumes ranged from 350 to 2000 cm^3. In addition, formulating the equation in terms of dynamical parameters allowed for reasonably accurate extrapolation to deposition in children (Schiller-Scotland *et al.*, 1992), in microgravity and hypergravity (Darquenne *et al.*, 1997), and with different carrier gases (Darquenne and Prisk, 2004).

Figure 2.2 displays the accuracy of the equation given by Martin and Finlay (2007) in predicting *in vivo* total deposition fractions in adults, while figure 2.3 demonstrates its ability to predict deposition in the diverse cases just mentioned. In both of these figures, the sigmoid curve is given by

$$TDF = \frac{0.92}{1 + \left(4.09 \times 10^{-6}\right) e^{-2.06 \ln(X)}} + 0.08 \tag{2.10}$$

where

$$X = (Stk^{*})^{0.8} + 0.01(t^{*})^{0.4}\left(\frac{V_t}{FRC}\right)^{0.8} \tag{2.11}$$

In equation (2.11), V_t is the tidal volume, the Stokes number is defined over the entire respiratory tract as

$$Stk^{*} = \frac{C_C \rho d^2 Q}{\mu (FRC)} \tag{2.12}$$

and, similarly, a dimensionless sedimentation parameter over the entire respiratory tract is defined as

$$t^{*} = \frac{C_C g \rho d^2 (FRC)^{2/3}}{\mu Q} \tag{2.13}$$

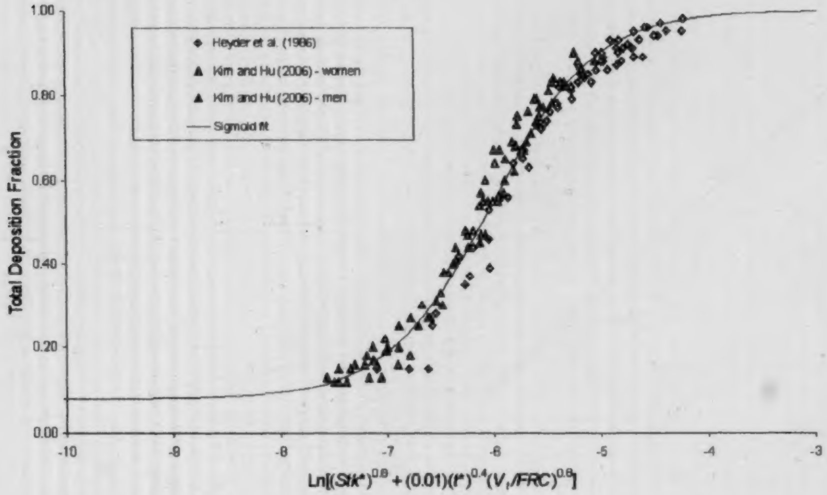

Figure 2.2. Adapted from Martin and Finlay (2007). Total *in vivo* deposition fractions measured in healthy adults during oral breathing are plotted against the sigmoid curve fit given by equation (2.10).

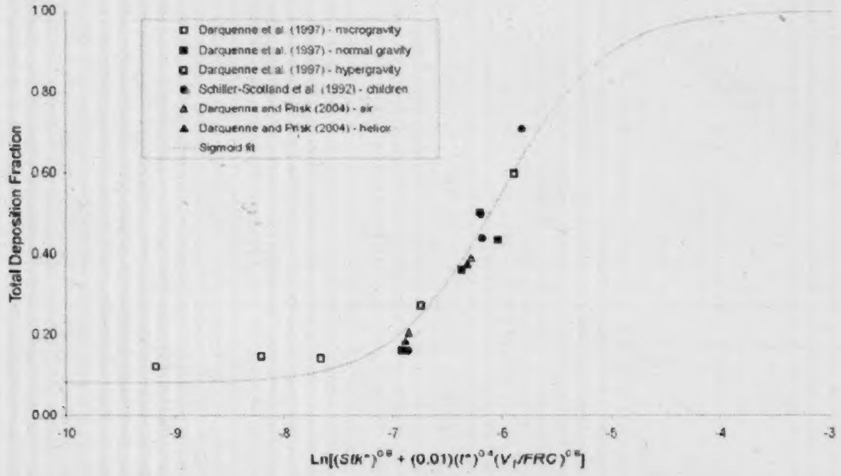

Figure 2.3. Adapted from Martin and Finlay (2007). Total *in vivo* deposition fractions measured in a variety of special conditions, with the curve fit from figure 2.2

where, in each of equation (2.12) and (2.13), Q is the inhalation flow rate, and FRC is the functional residual capacity, defined as the total volume of air in the lung at the start of an inhalation during tidal breathing.

While use of equations (2.10) through (2.13) is restricted to oral inhalation of particles greater than approximately 1 μm in aerodynamic diameter, Finlay and Martin (2008) have recently presented additional empirical equations that can be used to predict total deposition during oral inhalation of smaller particles, for which Brownian diffusion comes into play, as well as during nasal inhalation of particles greater than 1 μm in aerodynamic diameter. Empirical correlations to predict total deposition of smaller particles during nasal breathing are not currently available, due to the lack of adequate *in vivo* data upon which to base them.

Although the total deposition fraction of an inhaled aerosol is useful as a coarse measure of exposure, of further interest is the division of total deposition between the extrathoracic airways and the lung. This partitioning can be accomplished by combining empirical equations used to predict total deposition with equations for mouth-throat or nasal deposition (Finlay and Martin, 2008). Figure 2.4 displays mouth-throat and lung deposition fractions predicted in this manner for a typical adult during tidal breathing of micrometer-scale particles.

Unfortunately, *in vivo* data is not as extensive for extrathoracic deposition as for total deposition, and for the *in vivo* data that does exist (Stahlhofen *et al.*, 1989), certain key geometric parameters now recognized to influence deposition (Grgic *et al.*, 2004) were not recorded. As such, much of the present understanding of extrathoracic deposition has been garnered through *in vitro* experiments performed in physical replicas of the extrathoracic airways (examples of which were listed in section 2.3), as well as through computational fluid dynamics (CFD) simulations in numerical constructions of these airways (e.g. Zamankhan *et al.*, 2006; Xi and Longest, 2007; Liu *et al.*, 2007).

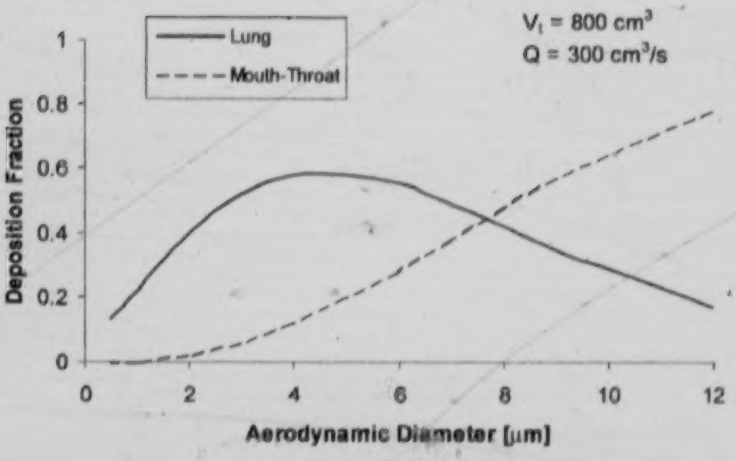

Figure 2.4. Mouth-throat and lung deposition fractions predicted for an adult with functional residual capacity of 3000 cm^3, tidal volume of 800 cm^3, and average inhalation flow rate of 300 cm^3/s. Mouth-throat deposition was predicted using the empirical equation provided by Rudolf *et al.* (1990), while lung deposition was predicted in the manner described by Finlay and Martin (2008), by combining the mouth-throat deposition fraction with the total deposition fraction given by Martin and Finlay (2007).

In circumstances where empirical equations for mouth-throat or nasal deposition fractions based on large *in vivo* data sets are not available, equations based on *in vitro* data or CFD simulations can instead be employed, so long as the approximations of these models are taken into consideration, and not trivialized. Ultimately, confidence in a given *in vitro* or numerical model must be gained through its ability to predict what limited *in vivo* data exists.

Further division of regional deposition patterns, beyond extrathoracic and lung fractions, is not possible using existing empirical deposition models. This is due to difficulties in measuring regional distributions of deposited particles within the lung, as discussed in detail in section 2.3. As an alternative, analytical, or dynamical (Finlay, 2001), models are widely used to estimate regional lung deposition down to the level of individual lung generations. Such models, dating back to the foundational work of Findeisen (1935) and Landahl (1950), have been reviewed in considerable depth by previous authors (Swift, 1996; Finlay, 2001; Finlay, 2003). In general, the lung is treated as a series of filters, with each filter representing those airways that make up a particular lung generation under some assumed, idealized lung geometry. Aerosol is then passed from one generation to the next, and the fraction of particles depositing in each generation due to different mechanisms is calculated using established analytical or empirical equations. Typically, deposition fractions due to sedimentation and diffusion are determined from analytical equations derived for aerosols passing through cylindrical tubes, whereas deposition due to inertial impaction is estimated using one of a number of empirical equations based on *in vitro* experiments performed in bifurcating airways. The total, combined deposition fraction in a given generation due to all three mechanisms is then often estimated as

$$P_{total} = \left(P_i^p + P_s^p + P_d^p\right)^{1/p} \tag{2.14}$$

where the subscripts *i*, *s*, and *d* indicated deposition fractions due to impaction, sedimentation, and diffusion, respectively, and *p* is a number greater than or equal to 1.

It is easy to appreciate how useful the information provided by regional deposition models might be in the design of delivery systems intended to target pharmaceutical aerosols to particular areas of the lung. This usefulness is muted somewhat by the highly idealized lung geometries assumed by most models, as well as by the present lack of *in vivo* data with which to validate predicted deposition patterns within the lung beyond a qualitative sense. Furthermore, equation (2.14) is clearly not rigorously accurate, as, in reality, particle trajectories may be influenced by more than one mechanism simultaneously. Equation (2.14), and others like it, do not usually lead to significant errors only because different deposition mechanisms tends to be dominant for different particle size ranges and in different regions of the lung (that is, for particles smaller than a few hundred nanometers in diameter, diffusion dominates, whereas for micrometer-sized particles, impaction dominates in the upper and central airways, and sedimentation dominates in the peripheral airways). However, Kleinstreuer *et al.* (2007) found that equation (2.14), with p = 1, significantly underpredicted numerically simulated deposition in generations 6-9 when deposition due both impaction and sedimentation was non-negligible.

Despite these limitations, certain regional deposition models, namely the ICRP (1994) model and the model of Finlay and Stapleton (1995), have been shown to predict, at least reasonably well, the dependence on aerosol size distribution of tracheobronchial and alveolar deposition fractions measured using SPECT imaging (Finlay *et al.*, 1996; Fleming *et al.*, 2006), although assumptions were made regarding the spatial distributions of airways belonging to these two lung regions in order to interpret the experimental data. In this regard, regional models can be used to gain insight into the effects of particle size and breathing pattern on the distribution of inhaled particles within the lung. As alluded to in the previous paragraph, this type of information has proved very useful over recent years in optimizing aerosol drug delivery systems. Figure 2.5 displays tracheobronchial and alveolar deposition fractions predicted using the model of Finlay and Stapleton (1995) for stable (that is, not evaporating or growing due to condensation), micrometer-scale particles inhaled by a typical adult during tidal breathing.

Figure 2.5 clearly indicates that the distribution of lung deposition between tracheobronchial and alveolar airways is strongly dependent on particle aerodynamic diameter. Accordingly, control over particle size and density allows aerosol delivery to be targeted to more central (tracheobronchial) or more peripheral (alveolar) regions of the lung. Broadly targeting deposition in such a manner is a widely used approach in aerosol delivery. For example, it is generally believed that inhaled bronchodilators should be delivered to the tracheobronchial airways for optimal effect, whereas drugs intended for systemic delivery should be delivered to the alveolar region, where absorption to the bloodstream is maximized.

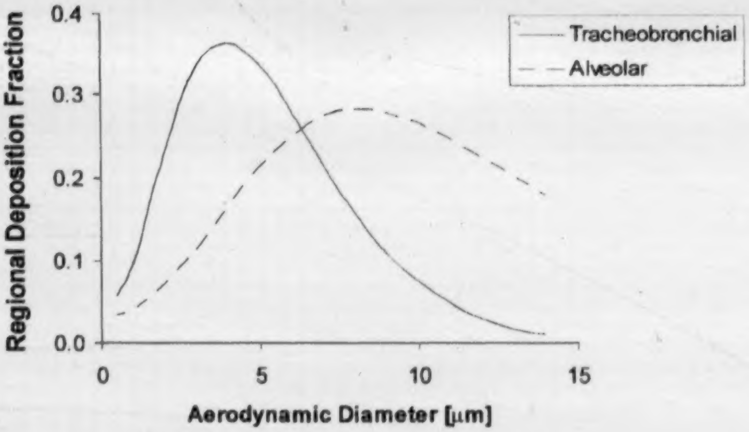

Figure 2.5. Tracheobronchial and alveolar deposition fractions predicted for an adult with functional residual capacity of 3000 cm^3, tidal volume of 800 cm^3, and average inhalation flow rate of 300 cm^3/s using the model of Finlay and Stapleton (1995).

In addition to particle size and density, the breathing pattern plays an important role in determining regional deposition patterns. With reference again to Figure 2.5, alveolar deposition would be somewhat larger, particularly for smaller particles, if the patient held his breath between inhalation and exhalation. This is because the breath hold would provide additional time for small particles to deposit by sedimentation in the peripheral regions of the lung prior to being exhaled. Furthermore, inhalation flow rates are typically much greater for patients using single breath inhalers than during normal tidal breathing, so that inertial impaction of particles in the mouth and throat increases substantially, and lung deposition is reduced. Aerosol drug delivery systems that provide user feedback in attempt to control patient breathing patterns for optimal targeting have recently been developed (Kohler *et al.*, 2005; Van Dyke, 2007), though it remains to be seen how they will be received by patients outside of controlled studies.

As discussed in the introduction to this thesis, even with optimized breathing patterns and particle sizes, current approaches to targeting pharmaceutical aerosols offer no ability to preferentially deliver drugs to specific lobes or segments of the lung. Even to enhance delivery to the right lung compared with the left, or vice versa, would be a considerable step forward. Given the present knowledge of regional deposition patterns gained through experimentation and modeling, it seems unlikely that this type of localized targeting can be achieved without either invasively administering drug to targeted sites, or employing some noninvasive, external influence to trigger particle deposition where desired.

2.5 Respiratory Tract Deposition of High Aspect Ratio Particles

Respiratory tract deposition of high aspect ratio particles (elongated particles with large length to diameter ratios) has received considerable attention owing to the health risk posed by inhaled fibers, such as asbestos. However, this same health risk prohibits inhalation studies with fibrous aerosols from being conducted in human volunteers, so that no *in vivo* data set exists for the deposition of high aspect ratio particles. Instead, researchers have performed a number of deposition studies in animal models (e.g. Timbrell and Skidmore, 1971; Morgan *et al.*, 1980; Brody *et al.*, 1981; Coin *et al.*, 1992; Oyabu *et al.*, 2004), though extrapolation from these studies to humans is confounded by the known differences in lung morphology between species (Yeh *et al.*, 1976). In at least one case, fiber lengths and diameters were measured *post mortem* in lung specimens of workers occupationally exposed to asbestos (Timbrell, 1982). Fibers with lengths on the order of tens of micrometers, but diameters of a few micrometers or less, were found throughout the lungs of the workers (Timbrell, 1982).

The results of Timbrell (1982) are consistent with those of *in vitro* studies on the deposition of fibrous aerosols. In a series of experiments (Myojo, 1987; Myojo, 1990; Myojo, 1997; Myojo and Takaya, 2001), Myojo and coworkers measured the deposition of glass fibers in two separate brass airway bifurcations with flow rates and airway dimensions chosen to represent tidal breathing through the second and third, and the third and fourth lung generations. The fibers studied had diameters of a few micrometers and smaller, and lengths ranging from approximately 10 to 100 μm (Myojo and Takaya, 2001). Even for the longest fibers studied, at most only a few percent, by count, of the fibers deposited in the bifurcations over a range of flow rates. The authors concluded that a large fraction these fibers would likely penetrate to the peripheral regions of the lung *in vivo* (Myojo and Takaya, 2001).

In a separate study, Sussman *et al.* (1991) measured the deposition of asbestos fibers in a replicate cast made from the tracheobronchial airways of a 34-year-old male. The cast included the larynx, and was trimmed back to approximately the tenth airway generation. The fibers had a reported median diameter of 0.3 μm. Very likely, fiber diameters increased with length; however, no attempt to correlate lengths and diameters was made

Table 2.2 Deposition of Asbestos Fibers Measured by Sussman *et al.* (1991) in a Replicate Cast of the First Ten Lung Generations

Inhalation Flow Rate [l/min.]	Fiber Lengths [μm]	Deposition Efficiency [% count]
15	2 - 5	4
15	5 - 10	8
15	10 - 20	14
15	> 20	23
60	2 - 5	6
60	5 - 10	20
60	10 - 20	41
60	> 20	88

in the study by Sussman *et al.* (1991). The total deposition of fibers in the cast is given in table 2.2 for two different inhalation flow rates, and for different length ranges. For all but the longest fibers at the higher flow rate, a majority of fibers penetrated through the cast.

At first glance, the deposition of high aspect ratio particles measured *in vitro* and *post mortem* may seem at odds with the experimental data and models described previously for compact particles. Whereas compact particles larger than 10 μm in aerodynamic diameter are predominantly captured in the mouth, throat, and main bronchi, high aspect ratio particles tens of micrometers in length penetrate to the periphery of the lung in high fractions. This apparent discrepancy can be resolved through consideration of the physical mechanisms through which high aspect ratio particles deposit. These are chiefly the same mechanisms as for compact particles, namely impaction, sedimentation, and diffusion; however, a fourth mechanism, interception, can also come into play, and will be discussed further below.

Given the extensive archival literature on the motion and deposition of compact, approximately spherical aerosol particles, it makes sense to consider the motion of high aspect ratio particles in a manner that is easily comparable to results for spherical particles. This involves derivation of equivalent spherical diameters for particle motions due to inertia, gravity, and diffusion, but before these can be given, it is first necessary to present a discussion of the drag force acting on a high aspect ratio particle.

By approximating the shape of a high aspect ratio particle as a prolate ellipsoid, which is a convenient mathematical form, the drag force acting on the particle under the assumption of low particle Reynolds number can be written in a form similar to the Stokes solution for the drag force acting on a spherical particle (Fuchs, 1964)

$$\vec{F}_d = -3\pi\mu d_e X_s\left(\vec{v} - \vec{v}_f\right) \tag{2.15}$$

where d_e is the diameter of the prolate ellipsoid (that is, twice the minor radius), X_s is a shape factor that depends on the aspect ratio of the ellipsoid (the ratio between the major and minor radii) and the orientation of the ellipsoid with respect to its direction of motion, and all other variables are as defined previously for spherical particles in equations (2.1) and (2.2).

Equations for the shape factor were determined by Oseen (1927) for motion parallel and perpendicular to the ellipsoid's major axis, and are given by

$$X_{s,//} = \frac{4\left(\beta^2 - 1\right)}{3\left[\frac{2\beta^2 - 1}{\sqrt{\beta^2 - 1}} \ln\left(\beta + \sqrt{\beta^2 - 1}\right) - \beta\right]} \tag{2.16}$$

and

$$X_{s,\perp} = \frac{8\left(\beta^2 - 1\right)}{3\left[\frac{2\beta^2 - 3}{\sqrt{\beta^2 - 1}} \ln\left(\beta + \sqrt{\beta^2 - 1}\right) + \beta\right]} \tag{2.17}$$

where β is the particle aspect ratio.

For large aspect ratios, Happel and Brenner (1965) provide considerably simpler equations for the shape factor, which were adopted by Harris and Fraser (1976) in their analytical model of respiratory tract deposition of inhaled fibers. These are

$$X_{s,//} = \frac{2\beta}{3\left[\ln(2\beta) - 0.5\right]} \tag{2.18}$$

and

$$X_{s,\perp} = \frac{4\beta}{3\left[\ln(2\beta) + 0.5\right]} \tag{2.19}$$

The drag force acting on a general prolate ellipsoid with long axis at some angle θ with respect to its direction of motion, as depicted in figure 2.6, can be resolved into components parallel and perpendicular to the long axis due to the linearity of equation (2.15) (Fuchs, 1964). These components are

$$F_{d,//} = -3\pi\mu U d_e X_{s,//} \cos\theta \tag{2.20}$$

and

$$F_{d,\perp} = -3\pi\mu U d_e X_{s,\perp} \sin\theta \tag{2.21}$$

where U is the magnitude of the velocity of the particle with respect to the fluid, and θ is defined in figure 2.6.

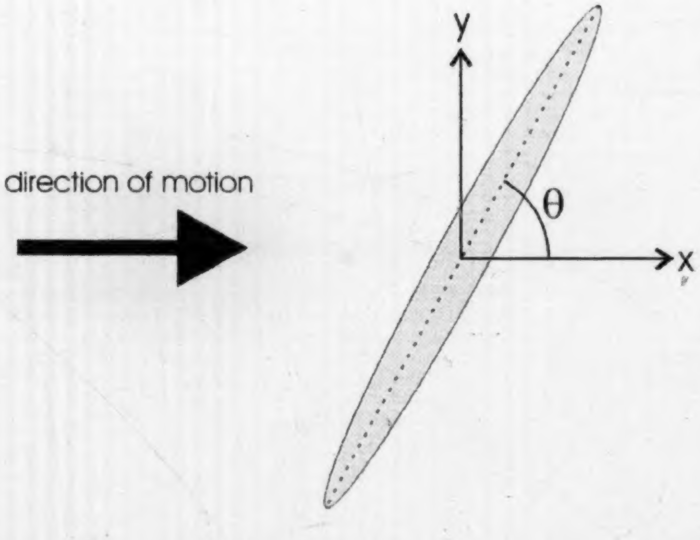

Figure 2.6. Coordinate system for a prolate ellipsoid moving with respect to the surrounding fluid.

In the general case, the net drag force resulting from equations (2.20) and (2.21) will act at some angle with respect to the particle's direction of motion. This resultant drag force can be written in terms of the coordinates defined in figure 2.6, in which the particle moves in the positive x direction with respect to the fluid

$$\vec{F}_d = -3\pi\mu U d_e \left\{ \left(X_{s,//} \cos^2\theta + X_{s,\perp} \sin^2\theta \right)\hat{\mathbf{i}} + \sin\theta\cos\theta \left(X_{s,//} - X_{s,\perp} \right)\hat{\mathbf{j}} \right\} \quad (2.22)$$

where $\hat{\mathbf{i}}$ and $\hat{\mathbf{j}}$ are unit vectors pointing in the positive x and y directions, respectively.

Throughout aerosol science, the drag force acting on a non-spherical particle is usually considered to be only that component acting opposite to the particle's direction of motion, that is, the $\hat{\mathbf{i}}$ term appearing in equation (2.22). Although the $\hat{\mathbf{j}}$ term also occurs due to the resistance of the fluid, this term can be considered as a lift force in that it acts in a direction perpendicular to the particle's motion. Figure 2.7 compares the magnitudes of lift and drag forces calculated from their respective terms in equation (2.22) for various particle aspect ratios. For θ ranging from 0 to 90°, the lift force is considerably smaller than the drag force. Previous theoretical studies of high aspect ratio aerosol deposition in the respiratory tract have altogether ignored the lift term (e.g. Harris and Fraser, 1976; Balashazy *et al.*, 1990), and in light of the present analysis, this seems to be a reasonable approximation. Furthermore, as will be described later in this section, high aspect ratio particles tend to align with their long axes parallel to the direction of flow through airways, so that both the angle θ and the lift force go to zero.

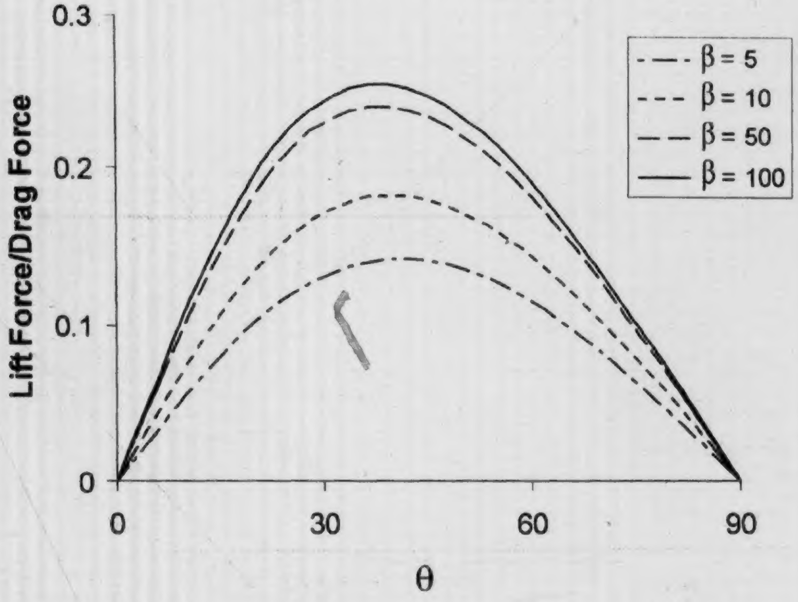

Figure 2.7. The ratio between the fluid resistance forces acting perpendicular (lift) and parallel (drag) to a high aspect ratio particle's direction of motion for various particle aspect ratios. θ is the angle between the particle's major axis and its direction of motion, as defined in figure 2.6.

With the drag force acting on a high aspect ratio particle approximated as that for a prolate ellipsoid, the settling velocity of the particle can be calculated by equating this force with that due to gravity. Then, by comparing expressions for the settling velocities of high aspect ratio and spherical particles, an equivalent spherical settling diameter can be determined for a given high aspect ratio particle. This is the diameter that gives the settling velocity of the high aspect ratio particle when substituted into equation (2.5) for the settling velocity of a spherical particle. Using the expressions for the shape factor given in equations (2.18) and (2.19), and approximating the volume of the particle as that of a cylinder, the equivalent spherical settling diameter for motion parallel to the particle's major axis is (Harris and Fraser, 1976; Prodi *et al.*, 1982; Yu *et al.*, 1986; Balashazy *et al.*, 1990)

$$d_{es,//} = \frac{3}{2} d_e \sqrt{\ln(2\beta) - 0.5} \tag{2.23}$$

and that for motion perpendicular to the particle's major axis is

$$d_{es,\perp} = \frac{3}{4} d_e \sqrt{2\ln(2\beta) + 1} \tag{2.24}$$

In addition, the equivalent spherical settling diameter for a randomly oriented particle, with average θ of arcos $\pi/4$ (Harris and Fraser, 1976), is

$$d_{es,r} = \frac{3}{2} d_e \left[\frac{0.385}{\ln(2\beta) - 0.5} + \frac{1.230}{\ln(2\beta) + 0.5} \right]^{-\frac{1}{2}} \tag{2.25}$$

As derived, equations (2.23) through (2.25) give equivalent spherical diameters for particle motion due to gravitational sedimentation; however, these diameters may also be used to describe motion due to particle inertia through the following simple argument.

By rearranging equation (2.4), the Stokes number for a spherical particle can be written as

$$Stk = v_s \frac{U}{Dg} \tag{2.26}$$

where v_s is the settling velocity defined for a spherical particle in equation (2.5), and the gravitational acceleration, g, the velocity scale, U, and the length scale, D, are all independent of particle properties.

Equation (2.26) can easily be shown to hold true for a non-spherical particle if equation (2.15) for the force of drag acting on a non-spherical particle is substituted into the general particle equation of motion given in equation (2.1), the equation is then non-dimensionalized to yield a Stokes number, and this Stokes number is written in terms of a general settling velocity for non-spherical particles. Given that all particle properties in equation (2.26) are contained within the settling velocity, and that the Stokes number determines the effects of inertia on particle motion, it can be concluded that equivalent spherical settling diameters derived theoretically for specific particle orientations are also equivalent spherical inertial diameters for those orientations. Indeed, theoretical equivalent diameters similar to those given by equations (2.23) through (2.25) have previously been shown to agree reasonably well with inertial, aerodynamic diameters measured using cascade impactors (Chan and Gonda, 1989; Cheng *et al.*, 1995).

In figure 2.8, the ratio between equivalent spherical aerodynamic (inertial or settling) diameter and particle diameter is plotted versus aspect ratio for particles oriented parallel, perpendicular, and at random with respect to their direction of motion. Regardless of orientation, the particle aspect ratio has little effect on these equivalent diameters. In fact, equivalent spherical diameters are only a few times larger than actual

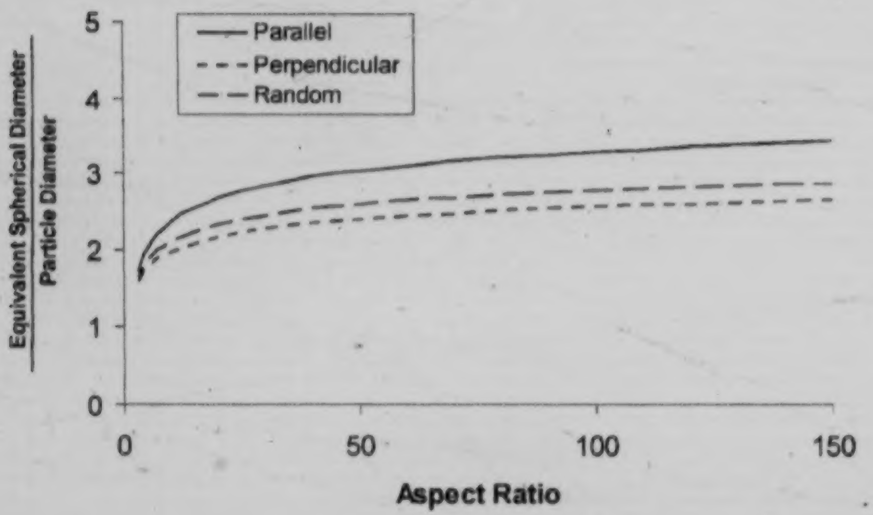

Figure 2.8. The ratio between equivalent spherical aerodynamic diameter and actual particle diameter is plotted versus aspect ratio for parallel, perpendicular, and random orientations of high aspect ratio particles with respect to their direction of motion.

particle diameters for aspect ratios larger than 100. This explains the ability of very long, thin particles to penetrate deep into the lungs, as was observed in the *post mortem* and *in vitro* studies cited at the beginning of this section. For example, an inhaled 1 μm diameter particle with a length of 100 μm has an equivalent spherical diameter close to 2 or 3 μm, depending on its orientation, and therefore has a high probability of reaching the alveolar region of the lung.

Just as equivalent spherical aerodynamic diameters can be used to predict deposition of high aspect ratio particle due to inertia and sedimentation, equivalent spherical diffusion diameters can be used to estimate deposition due to diffusion. These are the diameters that give the actual diffusion coefficients of high aspect ratio particles when substituted into equation (2.9) for the diffusion coefficient of a spherical particle. In order to determine the diffusion coefficient of a high aspect ratio particle, equation (2.9) can be written in a more general form as (Einstein, 1905)

$$D_d = \frac{k_B T}{f} \tag{2.27}$$

where k_B is again the Boltzmann constant, T is the temperature, and f is the drag force on the particle per unit velocity, which is given by (Asgharian *et al.*, 1988)

$$f = \frac{f_o}{C_C} \tag{2.28}$$

where f_o is the drag force per unit velocity in the continuum regime (that is, for particle dimensions much larger than the mean free path of molecules in air), and C_C is the slip correction factor.

Accordingly, with the drag force in the continuum regime defined above by equation (2.22), the only additional information required to determine the diffusion coefficient is the slip correction factor for high aspect ratio particles. Expressions for slip correction factors of prolate ellipsoids are given by Asgharian *et al.* (1988), following the method of Dahneke (1973), for different particle orientations. It should be noted here that when these correction factors are significantly greater than unity, they should also be used to modify the expression for the drag force used in describing motion due to inertia and sedimentation, in a manner analogous to that described previously for spherical particles. Figure 2.9 displays slip correction factors for motion parallel and perpendicular to a particle's major axis over a range of particle dimensions. For particles 1 μm and greater in diameter, the slip correction factor is not much larger than 1, and diffusion plays a negligible role in determining particle trajectories. As particle diameters become smaller, diffusion is increasingly important, given that the particle diffusion coefficient in equation (2.27) is directly proportional to the slip correction factor; however, slip correction factors fall off rapidly with aspect ratio. Also of note in figure 2.9 is that slip

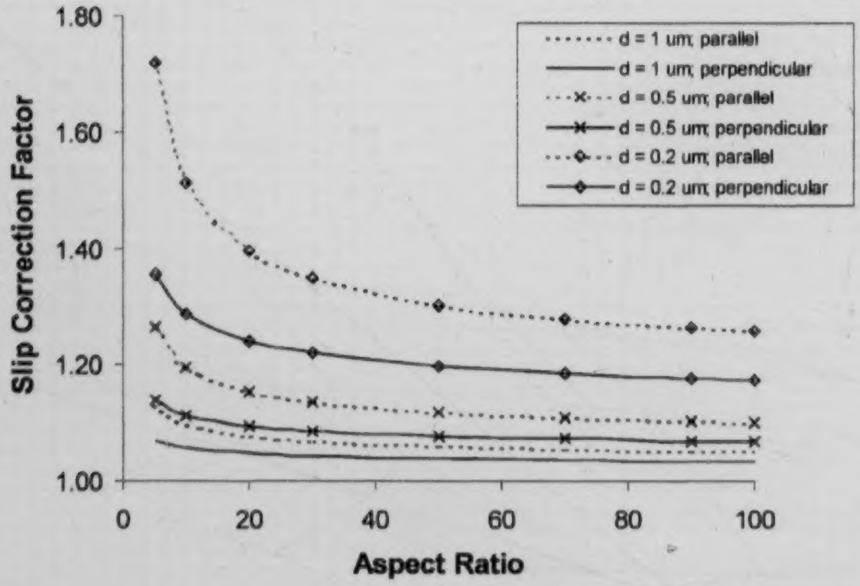

Figure 2.9. Slip correction factors from Asgharian *et al.* (1988) for motion parallel and perpendicular to a particle's major axis over a range of particle dimensions.

correction factors are considerably larger for motion parallel to a particle's major axis than for motion perpendicular to this axis, indicating that high aspect ratio particles will tend to diffuse more in the parallel direction.

By comparing equation (2.27) to equation (2.9) for the diffusion coefficient of a spherical particle, equivalent spherical diffusion diameters can be defined for various particle orientations. As expressions for these diameters become quite cumbersome, they will not be presented here, and the interested reader is instead referred to Asgharian *et al.* (1988).

Equivalent spherical aerodynamic and diffusion diameters are very useful, in that they can be substituted into correlations developed for spherical particles to predict airway deposition of high aspect ratio particles due to inertial impaction, gravitational sedimentation and Brownian diffusion. However, a fourth mechanism, interception, also influences deposition of high aspect ratio particles, and cannot be estimated using equivalent spherical diameters. Interception refers to the circumstance in which a particle rotates so that its tip comes into contact with an airway wall, even though its center of mass remains some distance away. Given the small size of respirable aerosol particles, this contact is sufficient to cause deposition, as adhesion to walls cannot be overcome by aerodynamic drag (at least for air velocities typical of those found in the respiratory tract). Figure 2.10 illustrates the deposition of a high aspect ratio particle by interception, where an equivalent aerodynamic diameter sphere does not deposit.

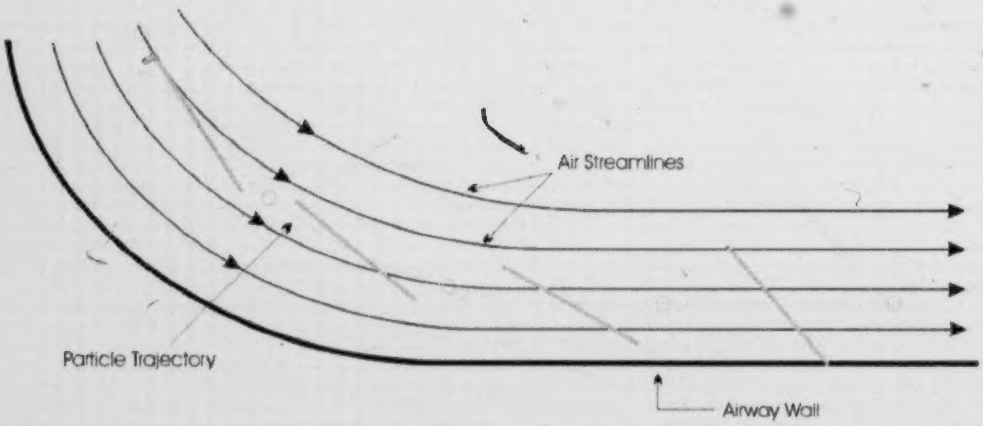

Figure 2.10. Deposition of a high aspect ratio particle due to interception is shown schematically. Although the high aspect ratio and spherical particles follow the same trajectory, rotation of the former can lead to interception with an airway wall.

Deposition due to interception is strongly influenced by the length of a particle with respect to airway diameters, as well as the particle's orientation with respect to airway walls (Asgharian and Yu, 1989; Balashazy *et al.*, 1990). As airway diameters decrease by two orders of magnitude between the trachea and the peripheral airways, for a specified particle length, interception can be expected to become increasingly important moving deeper into the lung. Accordingly, interception is often described as enhancing deposition in the peripheral lung over that expected for an aerodynamic or diffusion equivalent spherical particle.

As discussed above, the relatively weak dependence of a high aspect ratio particle's length on its equivalent spherical aerodynamic diameter allows long, thin particles to escape deposition in the extrathoracic airways and central branches of the bronchial tree, whereas a spherical particle of equivalent volume might not. For aspect ratios larger than about 5, this conclusion holds regardless of particle orientation. In contrast, interception can increase deposition of such particles in the peripheral airways above that of an equivalent sphere, and this increase *will* be highly dependent on particle orientation. These considerations led Chan and Gonda (1989) to propose that high aspect ratio particles be used to target aerosol drug delivery to the peripheral regions of the lung, and the concept has since been explored by a number of other researchers (Johnson and Martonen, 1994; Zeng *et al.*, 2000; Crowder *et al.*, 2002). In order to estimate the effect of interception on particle deposition in the peripheral airways, it is prudent to consider now the angular motion of particles in these airways.

A general solution for the angular motion of a prolate ellipsoidal particle in linear shear flow, in the absence of fluid or particle inertia, was given by Jeffery (1922). As recognized by previous researchers (Harris and Fraser, 1976; Asgharian and Yu, 1989) Jeffery's results can be used to gain insight into the angular motion of high aspect ratio particles in the small airways of the lung, provided that the particle lengths are relatively small compared to the airway diameters. For the system of coordinates defined below in figure 2.11, with the particle's long axis in the velocity-gradient (*zy*) plane, the angular velocity of the particle will be

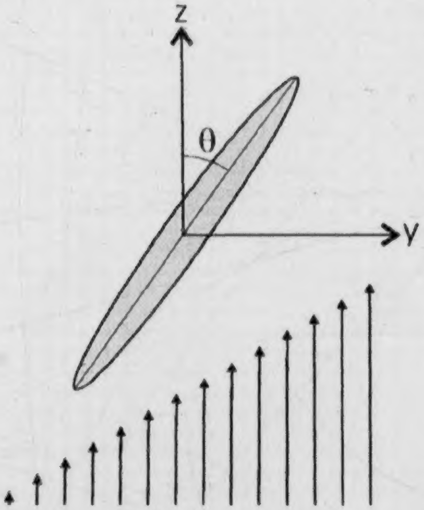

Figure 2.11. Schematic of a prolate ellipsoid in a linear shear flow.

$$\frac{\mathrm{d}\theta}{\mathrm{d}t} = G\frac{d_e^{\,2}\cos^2\theta + l_e^{\,2}\sin^2\theta}{d_e^{\,2} + l_e^{\,2}} \tag{2.29}$$

where G is the velocity gradient, and d_e and l_e are the ellipsoid's diameter and length.

From equation (2.29) it can be surmised that a particle will have maximum angular velocity when its long axis is perpendicular to the direction of the flow, where $\theta = 90°$, and minimum angular velocity when its long axis is parallel to the direction of the flow, where $\theta = 0$. This leads to the conclusion that, during the period of a rotation, the particle will spend most of the time with its long axis oriented close to the direction of the flow

(Fuchs, 1964). Such end over end rotation is actually a special case of Jeffery's solution, as, under the assumptions made by Jeffery (1922), a particle will maintain any initial angle of inclination with respect to the velocity-gradient plane *ad infinitum*. In the general, degenerate case, the description of angular motion given above applies instead to the projection of a particle's long axis in the velocity-gradient plane. However, in more recent work, Subramanian and Koch (2005) extended the problem defined by Jeffery (1922) to include small effects of fluid inertia, and found that the long axis of a rotating particle will tend to drift towards the velocity-gradient plane.

In light of the Jeffery's results, it is widely believed that in the small airways of the lung, where the flow is laminar and developed (Finlay, 2001), high aspect ratio particles will predominantly align parallel to the flow, but will undergo periodic rotations which may lead to interception with airway walls (Balashazy *et al.*, 1990). The frequency of these rotations during transit through an airway is therefore important in determining interception. Harris (1972) derived the period of rotation for a particle undergoing Jeffery (1922) motion as

$$T = 2\pi \frac{d_e^{\,2} + l_e^{\,2}}{G d_e l_e} \tag{2.30}$$

For large aspect ratios, this equation simplifies to

$$T = \frac{2\pi\beta}{G} \tag{2.31}$$

In table 2.3, the periods of rotation predicted by equation (2.31) for aspect ratios of 10 and 20 are compared to particle residence times in airway generations 7-23, spanning the lower airways of the tracheobronchial region through the entire alveolar region.

Residence times are predicted according to the idealized lung geometry given by Finlay *et al.* (2000) for an inhalation flow rate of 18 l/min. Average airway velocity gradients are calculated, assuming Poiseuille flow, from (Harris, 1972)

$$G = \frac{16\overline{U}}{3D} \tag{2.32}$$

where $\overline{U}$ is the average airway velocity, and D is the airway diameter.

From the results listed in table 2.3, it is evident that, for both aspect ratios, predicted periods of rotation are greater than airway residence times throughout the peripheral lung. This implies that particles will undergo less than one rotation during transit through an airway. To result in interception with an airway wall, this rotation must occur at a time when a particle is already close to the wall, for example, as the particle is carried past the carinal ridge of a bifurcation. In the majority of circumstances, this will not be the case, so that it can be concluded that the effect of shear in the entraining airflow on high aspect ratio particle orientations limits airway deposition due to interception.

While the angular motion of particles with diameters and lengths in the micrometer size range will be dominated by the shear alignment described above, the orientations of smaller particles can be affected by Brownian collisions with air molecules. Indeed, Brownian collisions will prevent very small particles from adopting any preferred orientation with respect to the surrounding flow. Asgharian and Yu (1989) defined a rotational Peclet number to compare the relative effects of shear alignment and Brownian rotation on particle orientation. Their rotational Peclet number can be written

Table 2.3 Particle Residence Times and Periods of Rotation in the Lower Airways of the Tracheobronchial Regional and the Alveolar Region

Generation	t_{res} [ms]	$T_{\beta=10}$ [ms]	$T_{\beta=20}$ [ms]
7	37	190	381
8	41	185	369
9	42	164	327
10	39	134	269
11	36	112	224
12	32	98	197
13	32	98	197
14	35	115	229
15	28	119	238
16	43	224	447
17	47	240	480
18	85	480	959
19	114	693	1387
20	203	1162	2324
21	336	1746	3493
22	560	2840	5680
23	923	3577	7153

as

$$Pe_r = \frac{G}{B_\omega k_B T} \tag{2.33}$$

where B_ω is the angular mobility of the particle, given for prolate ellipsoids by Gans (1928).

Through a series solution to the Fokker-Plank equation governing the orientation distribution of particles, Asgharian and Yu (1989) found that for Pe_r less than 1, Brownian rotation is dominant and particles assume a random distribution of orientations, whereas above Pe_r of approximately 100, the effect of shear becomes dominant and particles undergo the periodic rotations described above. Figure 2.12 displays values of Pe_r for different particle diameters and aspect ratios in generation 14 of the lung, for an inhalation flow rate of 18 l/min. For 0.2, 0.5, and 1 μm diameter

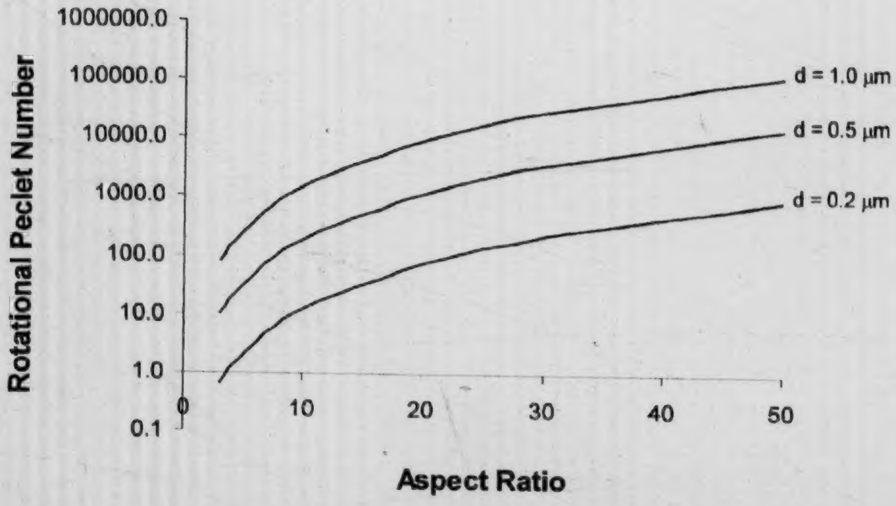

Figure 2.12. The rotational Peclet number defined by Asgharian and Yu (1989) is plotted versus particle aspect ratio for different particle diameters. The values shown are those of particles in the 14th generation of the idealized lung geometry of Finlay *et al.* (2000), for an inhalation flow rate of 18 l/min.

particles, Pe_r exceeds 100 for lengths of approximately 4.5, 4, and 3.5 μm, respectively. Moving below these lengths, Brownian collisions will begin to increasingly affect particle orientations.

From the preceding results, it can be concluded that high aspect ratio particles with diameters of hundreds of nanometers and larger, and lengths of a few micrometers and larger will by and large be aligned parallel to the direction of airflow through the small airways of the lung. This alignment will reduce deposition by interception below that which would occur for any other particle orientation. Accordingly, if particle orientations within the lung could somehow be externally controlled, interception could be increased. Such control would not only be useful in enhancing broad targeting of pharmaceutical aerosols to the peripheral airways, but, if orientation was adjusted to promote interception in only one location of the lung, the technique could allow for localized targeting to that particular location. The parameter ranges for which such an approach might be successful are examined in Chapter 3 using an analytic model of high aspect ratio particle deposition in bifurcating airways, but, first, an approach to noninvasively controlling particle orientations within the lung using external magnetic fields is outlined.

2.6 Magnetic fields in matter

The field of magnetostatics developed rapidly through the early part of the 20th century, with considerable controversy (Brown, 1962). The unification of electric and magnetic phenomena formulated by Maxwell in the previous century led many researchers to conclude that all magnetic fields stem from electric currents, whether these are currents through wires, electrons orbiting nuclei, or electrons spinning about their axes. This belief is widely held today as being physically accurate (Griffiths, 1999), though it must be kept in mind that concepts such as electrons orbiting nuclei are themselves metaphors for much more complex systems. The competing view that magnetic fields in matter result from separated north and south magnetic poles, in analogy to electric fields produced by positive and negative charges, is now generally thought to be outdated; however, magnetic poles (or positive and negative magnetic charges) are still used as mathematical concepts in describing magnetic fields in matter (e.g. Skomski and Coey, 1999; Skomski, 2007).

Whether the magnetic fields in matter are thought to arise from tiny loops of current or from magnetic poles, it is agreed that magnetic monopoles do not exist (Griffiths, 1999; Skomski and Coey, 1999). Accordingly, the basic unit of magnetism can be taken as the magnetic dipole. Figure 2.13 illustrates magnetic dipoles produced by poles (the Gilbert model), and by a current loop (the Ampère model). If the Ampère model is adopted, it can be demonstrated that, in a uniform magnetic field, a magnetic dipole will experience no net force, but will be subject to a torque tending to align it parallel with the field (because, according to the Lorentz force law, the magnetic force is proportional to the cross product of the current with the magnetic field; Griffiths, 1999). In a nonuniform field, a dipole will experience a force proportional to the field gradient as well as a torque (Griffiths, 1999).

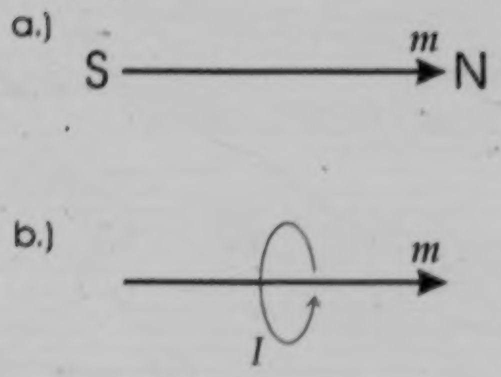

Figure 2.13. (a.) Gilbert model and (b.) Ampère model for a magnetic dipole, with dipole moment *m*.

Of course, in most applications, it is the force and torque acting on a large collection of dipoles making up a magnetic body that is of interest. Before describing this force and torque, it is necessary to provide a few brief definitions. A cause of some confusion in magnetostatics is that different authors refer to two different fields, the *B*-field and the *H*-field, as *the* magnetic field. In SI units, these two fields are related by the following expression

$$\vec{B} = \mu_0\left(\vec{H} + \vec{M}\right) \tag{2.34}$$

where μ_0 is a constant called the permeability of free space, and M is the magnetization, the net dipole moment per unit volume, of the medium.

In the absence of any magnetization, such as in air, B is directly proportional to H. Within a magnetic body, the B-field is the total magnetic field due to contributions from external sources, the H-field, and from magnetic dipoles within the body itself, the magnetization. In terms of their magnetic properties, different materials are classified according to the relationship between their magnetization and the H-field. For example, materials are called linear media if

$$\vec{M} = \chi \vec{H} \tag{2.35}$$

where the magnetic susceptibility, χ, is constant.

Linear media are further subdivided into paramagnetic and diamagnetic materials depending on whether their magnetic susceptibilities are positive or negative. Regardless of this distinction, in general linear media have very low susceptibilities, so that they are unaffected by all but very strong magnetic fields.

The materials that are most commonly associated with magnetism, such as iron, nickel, and cobalt, are classified as ferromagnetic. For ferromagnetic materials, the relationship between M and H is nonlinear, and M will asymptotically approach a maximum value, the saturation magnetization, as H increases. Furthermore, a ferromagnetic material will exhibit remnant magnetization (that is, non-zero magnetization) after being removed from an external field, owing to the ability of groups of neighboring, aligned dipoles within the material, called domains, to withstand realignment due to random thermal motions. Detailed descriptions of the domain theory of ferromagnetism can be found in Brown (1967), McCaig and Clegg (1987), and Skomski and Coey (1999). In the context of the present thesis, it will only be mentioned that very small ferromagnetic particles, on the order of tens of nanometers, each contain only a single domain, and the size of a particle limits the number of dipoles contained in that domain. Below a critical size, the domain will no longer withstand realignment due to thermal energies upon removal from an external magnetic field, and the particle is called superparamagnetic: paramagnetic due to the absence of a remnant magnetization, but *super* because the magnetization in the presence of an external field is much larger than that of normal paramagnetic materials.

If the relationship between the magnetization of a body and the external *H*-field is known, the magnetic force and torque acting on that body can be calculated from the following equations (Shine and Armstrong, 1987)

$$\vec{F}_m = \mu_0 \int \left(\vec{M} \cdot \nabla \vec{H} \right) dV \tag{2.36}$$

and

$$\vec{T}_m = \mu_0 \int \left(\vec{M} \times \vec{H} \right) dV \tag{2.37}$$

As was the case for individual magnetic dipoles, the force acting on a magnetic body depends on the field gradient, ∇H, whereas the magnetic torque depends on the field strength, *H*. As reviewed by Dobson (2006), many previous researchers have proposed that high gradient magnetic fields be used to target magnetic drug carriers from the bloodstream to specific organs using a translational magnetic force, dating back to work in the late 1970s (Widder *et al.*, 1978; Mosbach and Schroder, 1979). This approach has been proposed for targeting aerosol drug delivery much more recently (Ally *et al.*, 2005;

Dames *et al.*, 2007). Low frequency magnetic fields are attractive for noninvasive targeting, in that they pass through the tissues of the body relatively unattenuated; however, the requirement of high field gradients to produce a force on particles at specified depths within the body is a significant obstacle to overcome (Coates, 2008). Accordingly, scale-up of experiments performed in small laboratory animals to clinical application in humans has proven difficult (Dobson, 2006; Coates, 2008). As seen in equations (2.36) and (2.37), a uniform magnetic field will not produce a force on magnetized particles, but will produce a torque. Therefore, uniform, or low gradient, magnetic fields might be used to noninvasively control high aspect ratio particle orientations in the lung, thereby influencing particle deposition due to the interception mechanism as described in the previous section.

2.7 Magnetic alignment of high aspect ratio particles

It has long been known that elongated magnetic particles will align with their long axes parallel to an external magnetic field (e.g. Mendelsohn *et al.*, 1955). In order to determine the rotational motion of magnetic, axisymmetric ellipsoidal particles subject to a uniform magnetic field in a quiescent fluid, Shine and Armstrong (1987) solved equation (2.37) for the magnetic torque acting on the particles in the limiting cases of linear magnetic media and saturated ferromagnetic materials, and performed numerical calculations for the case of unsaturated ferromagnetic materials. The main difficulty in obtaining such solutions is in determining the magnetization of the particles. In general, the magnetization is parallel to, and a non-linear function (which must be measured empirically) of, the *H*-field inside a particle. However, the *H*-field inside the particle is different from that outside the particle according to the equation

$$\vec{H}_i = \vec{H} - \overline{D} \cdot \vec{M} \tag{2.38}$$

where the subscript *i* denotes the field inside the particle, and $\overline{D}$ is referred to as the demagnetization tensor, dependant only on the shape of the particle (Osborn, 1945; Brown, 1962). It should be noted that this definition of the *H*-field inside the particle can be the source of much confusion; for example, although the integrals in equations (2.36) and (2.37) are taken over the volume of a magnetized body, it is the external field, *H*, which is used. Osborn (1945) referred to the field *H* as the 'applied field' and H_i as the 'magnetizing force', and commented that the fact that these two fields are not one and the same is 'a great disadvantage in research on magnetic materials'.

For a system of coordinates defined along the principal axes of an ellipsoid, the demagnetization tensor can be diagonalized, and has a trace of unity. The component of the tensor in each direction is then referred to as a demagnetizing factor for that direction. Demagnetizing factors have been determined from solutions for the magnetic field inside a magnetized body made by assuming a fictitious distribution of magnetic monopoles on the surface of the body, and then proceeding in direct analogy to the case of an electric field inside a polarized body (Elliot, 1998). Alternatively, identical results are obtained, provided the magnetization inside the body is assumed to be uniform, by replacing the surface pole distribution with a surface current per unit length equal to the magnetization parallel to the surface (Elliot, 1998). In any case, for a sphere, the demagnetizing factor is equal to 1/3 in any direction. For a prolate ellipsoid, the demagnetizing factor along the long axis tends towards zero as the ellipsoid becomes very long and thin, and, accordingly, this axis is termed an 'easy' axis of magnetization.

Physically, demagnetization can be conceptualized by considering a collection of ideal magnetic dipoles on a surface, as depicted in figure 2.14. Each dipole produces the field illustrated in figure 2.14a. If the dipoles are oriented perpendicular to the surface, as in figure 2.14b, the fields of neighboring dipoles oppose one another, whereas if the dipoles are oriented parallel to the surface, as in figure 2.14c, each dipole field is opposed by its neighbors above and below, but augmented by its neighbors to the left and right. Accordingly, if the dipole moments are equal, the net dipole field will be greater for dipoles aligned parallel to the surface than for dipoles aligned perpendicular to the surface. In the case of a long, thin prolate ellipsoid, magnetization along the long axis results in the majority of surface dipoles being aligned parallel to, or nearly parallel to the surface of the ellipsoid, with only those dipoles at the ellipsoid's ends aligned perpendicular to the surface. In contrast, magnetization perpendicular to the long axis results in approximately half as many surface dipoles being aligned perpendicular to the surface as parallel to the surface. As a result, magnetization is 'easier', and the demagnetizing factor is smaller, along the long axis than perpendicular to it.

Equation (2.38) indicates that the *H*-field inside a particle, which determines the direction of magnetization, is reduced from that outside the particle by a demagnetizing field, $-\overline{D} \cdot \vec{M}$. Anisotropy of the demagnetizing field is responsible for the magnetic torque that aligns high aspect ratio particles with external magnetic fields. As illustrated in

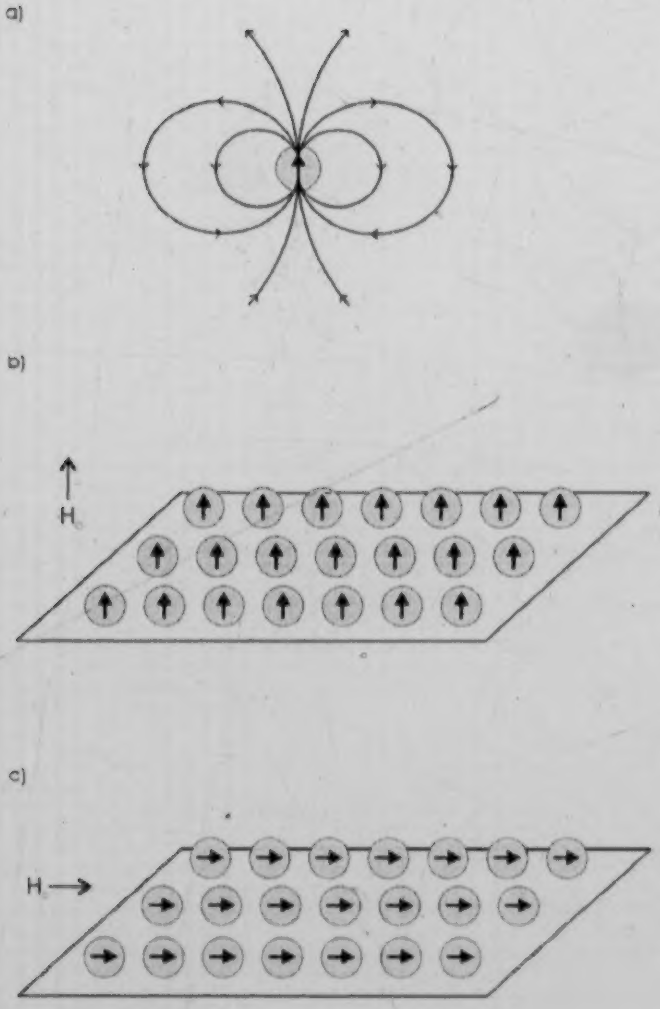

Figure 2.14. (a) The magnetic field produced by an ideal dipole. (b) Alignment of dipoles perpendicular to a surface. The fields of neighboring dipoles will oppose one another in this arrangement. (c) Alignment of dipoles parallel to a surface. Neighboring dipole fields oppose or augment one another depending on the relative positions of their source dipoles, resulting in a greater net dipole field, or magnetization, than that produced in the perpendicular arrangement.

figure 2.15, demagnetization reduces the component of the *H*-field much more significantly along the short axis of a particle than along the long axis (Brown, 1962; Shine and Armstrong, 1987). Consequently, the *H*-field, and the magnetization, inside the particle is not parallel to the field outside the particle, and a torque is produced according to equation (2.37) that tends to align the particle's long axis with the external field.

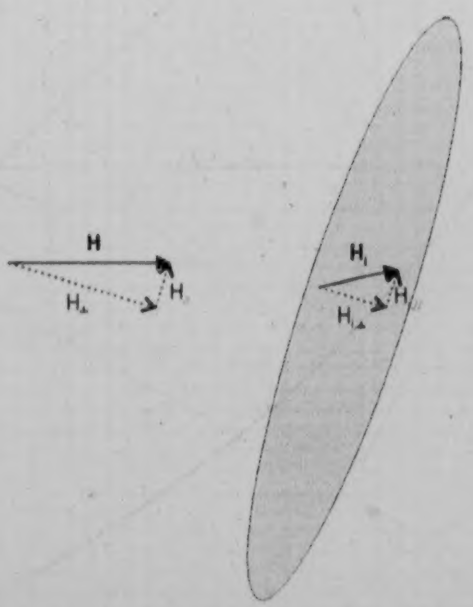

Figure 2.15. An illustration of the *H*-fields inside and outside of a high aspect ratio magnetic particle. The demagnetizing field reduces the *H*-field to a much greater extent along the particle's shorter axis than along the longer axis, resulting in a net internal field H_i that points in different direction from the external field *H*.

For applications in drug delivery, it is safe to assume that high aspect ratio particles of interest will have very low magnetic susceptibilities, and exhibit little if any response to all but extremely strong magnetic fields. However, it is possible that low susceptibility particles can be made magnetically responsive by loading them with smaller magnetic particles. For example, Zauscher and Humphrey (1997) demonstrated that alignment of wood fibers with magnetic fields on the order of 100 mT was feasible if the fibers were first coated with smaller, compact nickel particles. In a similar vein, Kim *et al.* (2005) have reported aligning plate-like particles loaded with iron oxide nanoparticles using a 20 mT magnetic field, while Osterloh *et al.* (2002) aligned needle-shaped particles loaded with iron oxide nanoparticles using a 90 mT field. Also, Haik *et al.* (2005) reported alignment of carbon nanotubes with iron oxide nanoparticles adsorbed to their surfaces using 500 mT magnetic fields.

In estimating the magnetization of composite particles comprised of small magnetic particles embedded in larger carriers, Skomski *et al.* (2007) suggested simply approximating the composite particle as a homogeneously magnetized body, with magnetization of

$$M_p = f_m M_m \tag{2.39}$$

where M_p and M_m are the magnetizations of the composite particle and the magnetic particles, respectively, and f_m is the volume fraction of the magnetic particles in the composite particle.

Furthermore, Skomski *et al.* (2007) proposed that demagnetizing factors for such composite particles be calculated according to

$$D_p = D_m(1 - f_m) + D_c f_m \tag{2.40}$$

where D_p is the demagnetization factor of the composite particle along a particular direction, and D_m and D_c are the corresponding demagnetizing factors of the magnetic and carrier particles.

In order to estimate the magnetic torque exerted on composite particles, the magnetization and demagnetizing factors determined from equations (2.39) and (2.40) can be substituted into solutions given by Shine and Armstrong (1987) for the magnetic torque acting on prolate ellipsoids. However, given that demagnetizing factors are determined from either surface distributions of magnetic poles or surface currents, it is uncertain whether they should be used for composite particles with no magnetic material, or discontinuous patches of magnetic material, at their surfaces. For example, in the limiting case of a single magnetic sphere encapsulated in a larger, nonmagnetic ellipsoid, equation (2.40) would yield different demagnetizing factors along long and short axes of the ellipsoid, leading to a nonzero magnetic torque on the composite particle. It seems unlikely that such a torque would occur in reality.

If these concerns are, for the moment, overlooked, the magnetic torque acting on a prolate ellipsoid estimated using Skomski *et al.*'s (2007) approach can be compared to the hydrodynamic (or aerodynamic) torque exerted on the ellipsoid in a linear shear flow in order to estimate whether or not magnetic torques will be large enough to alter the shear alignment expected for high aspect ratio particles in the peripheral airways of the lung. The aerodynamic torque was given by Jeffery (1922) for low Reynolds numbers as

$$\vec{T}_{ae} = \mu\left\{\vec{K}_1 \cdot \left(\vec{\omega}_f - \vec{\omega}_p\right) + \vec{K}_2 \cdot \vec{d}_f\right\} \tag{2.41}$$

where ω_f and ω_p are the angular velocities of the fluid and the particle, the components of d_f relate to the shear strain of the fluid (Zhang *et al.*, 2001), and the components of tensors K_1 and K_2 depend only on the geometry of the particle, where these tensors can be diagonalized for a coordinate system corresponding to the principal axes of the particle.

Considering a prolate ellipsoid fixed in space so that it cannot rotate, with its long axis in the velocity-gradient plane as depicted in figure 2.16, the component of the torque perpendicular to the plane is:

$$T_{ae,x} = \frac{2\pi\mu G d_e^{\,2} l_e \left(d_e^{\,2}\cos^2\theta + l_e^{\,2}\sin^2\theta\right)}{3\left(d_e^{\,2}\beta_o + l_e^{\,2}\gamma_o\right)} \tag{2.42}$$

where G is the fluid velocity gradient, d_e and l_e are the diameter and length of the ellipsoid, the angle θ is defined in figure 2.16, and β_o and γ_o are as given by Gallily and Cohen (1979):

$$\beta_o = \frac{\beta^2}{\beta^2 - 1} + \frac{\beta}{2\left(\beta^2 - 1\right)^{3/2}}\ln\left(\frac{\beta - \sqrt{\beta^2 - 1}}{\beta + \sqrt{\beta^2 - 1}}\right) \tag{2.43}$$

and

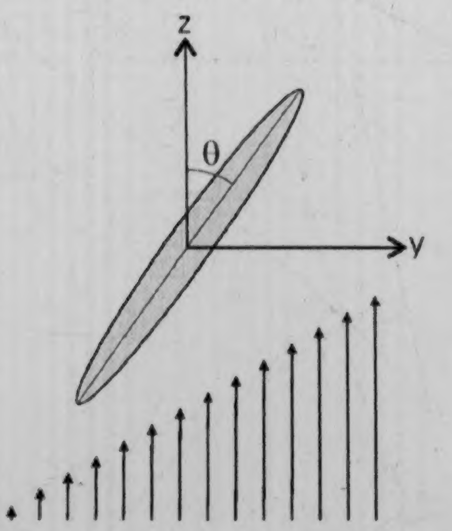

Figure 2.16. Schematic of the orientation of a prolate ellipsoid with respect to a linear shear flow.

$$\gamma_o = \frac{-2}{\beta^2 - 1} - \frac{\beta}{\left(\beta^2 - 1\right)^{3/2}} \ln\left(\frac{\beta - \sqrt{\beta^2 - 1}}{\beta + \sqrt{\beta^2 - 1}}\right) \tag{2.44}$$

where β is the ellipsoid's aspect ratio.

For θ = 90°, equations (2.42) through (2.44) can be used to estimate an upper limit for the aerodynamic torque exerted on an elongated particle aligned with an externally applied magnetic field. To maintain alignment, the magnetic torque on the particle should exceed this limit.

As described above, the magnetic torque can be estimated by substituting equations (2.39) and (2.40) for the magnetization and demagnetizing factors of composite particles into solutions derived for magnetic particles by Shine and Armstrong (1987). For an ellipsoid in a very strong, saturating magnetic field, with orientation defined in figure 2.16, the magnetic torque can be estimated, to the lowest order approximation, as

$$T_{m,x} = \mu_0 M_s^{\,2} V\left(D_{min} - D_{maj}\right)\sin\phi\cos\phi \qquad (2.45)$$

where M_s is the saturation magnetization, V is the volume of the ellipsoid, D_{min} and D_{maj} are the demagnetizing factors along the minor and major axes of the ellipsoid, and ϕ is the angle between the ellipsoid's major axis and the saturating magnetic field.

Figure 2.17 compares the magnetic torque predicted by equation (2.45), with the magnetization and demagnetizing factors for composite particles estimated from equations (2.39) and (2.40), with the aerodynamic torque predicted by equation (2.42). The composite particle is comprised of a prolate ellipsoid carrier with zero magnetic susceptibility loaded with spherical magnetite particles having a saturation magnetization of 4.7 x 10^5 A/m. The fluid velocity gradient is 548 s^{-1}, representing Poiseuille flow through the terminal bronchioles of the lung for a flow rate typical of tidal breathing. In estimating the magnitudes of both torques, sines and cosines of angles are given an order of 1. For a given volume fraction of magnetite in the composite particle, the ratio between the magnetic and aerodynamic torques is a function of the particle aspect ratio. Figure 2.17 indicates that, even for an aspect ratio of 100, the magnetic torque is expected to exceed the aerodynamic torque above a volume fraction of 0.07. This implies that magnetic alignment of high aspect ratio particles in the lung is feasible over a fairly wide range of parameters.

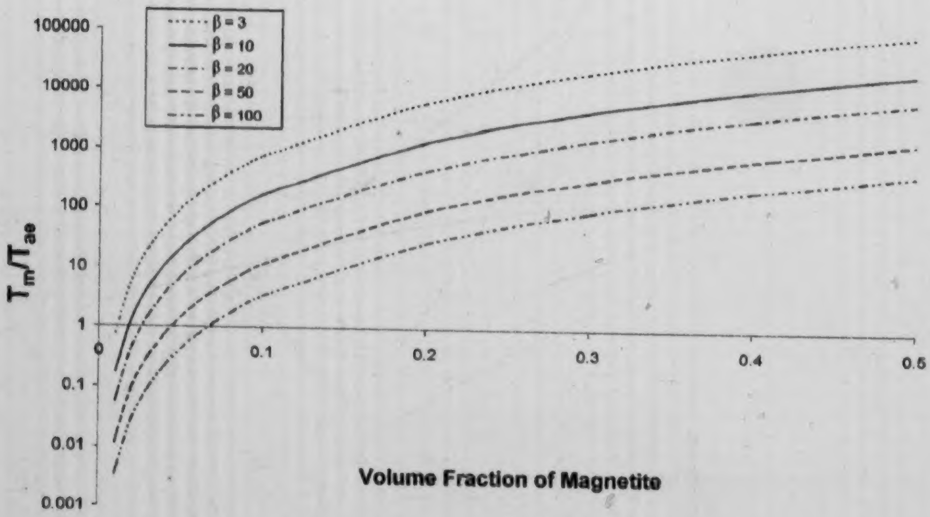

Figure 2.17. The ratio between the magnetic torque and aerodynamic torque for prolate ellipsoids loaded with smaller, spherical magnetite particles for a velocity gradient of 548 s^{-1} and a saturation magnetization of 4.7 x 10^5 A/m. The magnetization and demagnetizing factors of the composite particles were determined using the methods described by Skomski *et al.* (2007).

Given the concerns raised earlier over the use of demagnetizing factors for composite particles, a very simple model of ideal dipoles can be employed as an alternative approach to determining magnetic torques on idealized composite particles. Consider the composite particle depicted in figure 2.18, in which a row of magnetic particles, modeled as ideal dipoles, is embedded in a high aspect ratio carrier. The dipole field produced by each dipole is given in spherical coordinates by (Griffiths, 1999)

$$\vec{H}_{dip} = \frac{MV_m}{4\pi r^3}\left(2\cos\theta\hat{\mathbf{r}} + \sin\theta\hat{\boldsymbol{\theta}}\right) \tag{2.46}$$

where M is the magnetization of the magnetic particle modeled by the dipole, V_m is the volume of the magnetic particle, r is the distance from the origin (the center of the dipole), and θ is the zenith angle.

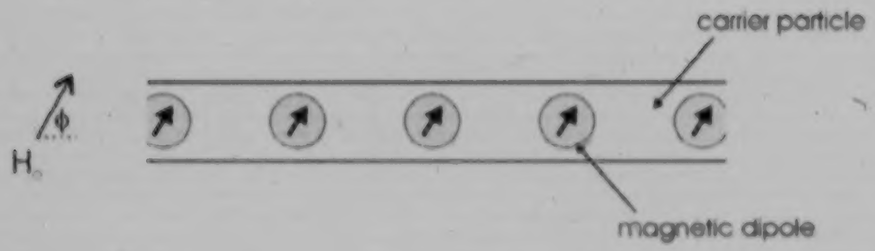

Figure 2.18. A simple model of ideal magnetic dipoles embedded in a carrier particle.

At the midpoint between any two dipoles, the vector sum of the fields produced by the two nearest dipoles can be determined. Assuming that the dipoles are equally spaced, and that the magnetic particles they model are of equal volume and spherical, the components of the net dipole field parallel and perpendicular to the carrier particle's long axis are:

$$H_{dip,//} = \frac{4}{3} M \cos\phi \left(\frac{d_m}{L}\right)^3 \tag{2.47}$$

and

$$H_{dip,\perp} = -\frac{2}{3} M \sin\phi \left(\frac{d_m}{L}\right)^3 \tag{2.48}$$

where d_m is the diameter of the magnetic particles and L is the spacing between the centers of neighboring particles. The negative sign in equation (2.48) indicates that this field points in the direction opposite to that of the perpendicular component of the dipole moments.

As the field produced by a dipole decreases with the cube of the distance from the dipole, equation (2.46), including a larger number of dipoles than the two used in the derivation of equations (2.47) and (2.48) results in only small changes to these expressions. In light of equation (2.34) for the total magnetic field, B, inside a magnetized body, the dipole field given by equations (2.47) and (2.48) can be thought of as the magnetization of the composite particle. The magnetic torque acting on the composite particle can then readily be estimated from equation (2.37) if the dipole field given by (47) and (48), calculated at the midpoint between magnetic particles, is assumed to be a reasonable, order of magnitude estimate of the field over the entire volume of the composite particle. With this assumption, the magnetic torque is

$$T_m = 2\mu_o VHM\left(\frac{d_m}{L}\right)^3 \sin\phi\cos\phi \qquad (2.49)$$

This equation for the magnetic torque bears a strong resemblance to that derived above, equation (2.45), using the concept of demagnetization and the approximations for composite particles proposed by Skomski *et al.* (2007). Whereas equation (2.45) depended on M_s^2, equation (2.49) depends on HM; however, equation (2.45) was derived using Shine and Armstrong's (1987) perturbation solution for a magnetic ellipsoid in a very strong, saturating field, where $H >> M$. Usually, ferromagnetic materials begin to asymptotically approach their saturation magnetization at much lower field strengths, where this inequality does not hold. Indeed, in their general, numerical solutions, Shine and Armstrong (1987) found that the magnetic torque *was* dependent on the H-field strength, with this dependence becoming decreasingly important as the ellipsoid became saturated (that is to say, the magnetic torque approached that calculated for $H>>M$ at much lower field strengths). If the same holds true for composite particles, equation (2.45) will overestimate the magnitude of the magnetic torque when $H<<M$, whereas equation (2.49) will overestimate the magnetic torque when $H>>M$, though this latter situation rarely arises in practice.

Of course, a further difference between the two equations for the magnetic torque is that equation (2.49) depends on the spacing of magnetic particles within the carrier, whereas equation (2.45) depends on the volume fraction of magnetic particles, through its effect on the magnetization and demagnetizing factors of the composite particle. Figure 2.19 compares magnetic torques, predicted using equation (2.49), to aerodynamic torques, from equations (2.42) through (2.44), over a range of magnetic loadings, d_m/L, and

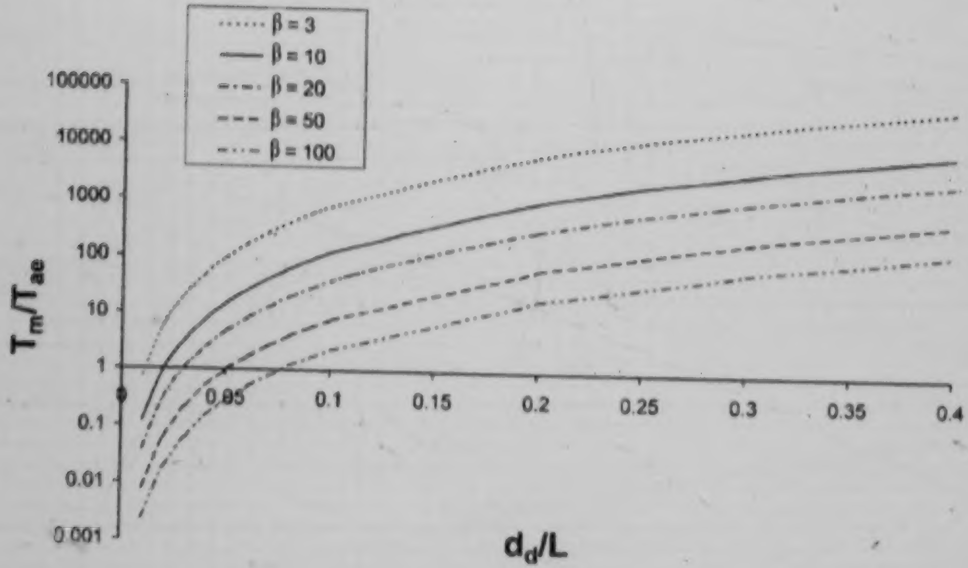

Figure 2.19. The ratio between the magnetic torque and aerodynamic torque for carrier particles loaded with smaller, spherical magnetite particles is plotted for various aspect ratios and magnetite loadings, where d_d is the diameter of the magnetite particles, and L is the spacing between the centers of neighboring magnetite particles. Calculations were performed for a velocity gradient of 548 s^{-1}, a magnetization of 4.7 x 10^5 A/m, and a field strength of 8.0 x 10^4 A/m.

particle aspect ratios, again for a fluid velocity gradient of 548 s^{-1}, typical of the terminal bronchioles, and a magnetization of 4.7 x 10^5 A/m, typical of magnetite near saturation. In addition, an *H*-field of 8.0 x 10^4 A/m was used in the calculations, which is representative of field strengths required to approach saturation of magnetite nanoparticles (Hou *et al.*, 2003; Cheng *et al.*, 2005).

As seen earlier in figure 2.17 for an alternative formulation of the magnetic torque, figure 2.19 indicates that the magnetic torque is predicted to exceed the aerodynamic torque for a large range of aspect ratios and magnetite loadings. Based on the discussions and calculations presented above, it is anticipated that high aspect ratio particles loaded with fairly small amounts of magnetite will align in the small airways of the lung with externally applied magnetic fields. Furthermore, noninvasive control over particle orientations is expected to allow for deposition of high aspect ratio pharmaceutical aerosols to be increased in targeted regions through the influence of particle orientation on interception. In the following chapter, the extent to which particle deposition can be increased through magnetic alignment in different generations of the lung, and for different particle sizes, will be explored using existing analytical deposition models for high aspect ratio aerosols in bifurcating airways.

3. ANALYTICAL DEPOSITION MODEL

3.1 Introduction

Analytical models used to predict respiratory tract deposition of inhaled aerosols were discussed in considerable detail in chapter 2. Such models predict deposition due to different underlying physical mechanisms at the level of individual lung generations. Results for spherical particles have been extended to high aspect ratio particles, mainly using the concept of equivalent spherical diameters, by several previous research groups interested in predicting the deposition patterns of inhaled fibers (Harris and Fraser, 1976; Asgharian and Yu, 1988; Balashazy *et al.*, 1990; Sturm and Hoffmann, 2006). As noted in chapter 2, a significant limitation of analytical models is in the lack of a rigorous approach to combining predicted deposition fractions due to different mechanisms into one total deposition fraction. Given that the vast majority of *in vitro* studies in bifurcating airways have been conducted in models representing the first few branches of the tracheobronchial tree, in which deposition due to inertial impaction is dominant, empirical approaches to combining deposition fractions have not been experimentally validated in situations where no one deposition mechanism dominates.

Despite this limitation, analytical models allow at least an estimate, as opposed to a definitive quantification, of the relative influences of different physical mechanisms on airway deposition for varying particle properties, flow conditions, and airway geometries. In this chapter, a model for predicting deposition of high aspect ratio particles in bifurcating airways will be briefly described, and then predictions will be made regarding the influence of particle orientation on deposition in different generations of the lung. As small airways in the lung are essentially randomly oriented, it is likely that magnetic alignment of particles in one specific direction will result in random particle orientations with respect to airways. Therefore, in order to estimate effects of magnetic alignment on deposition, predictions made for particles oriented at random with respect to airways will be compared with those made for particles oriented parallel to airways, which is the predominant orientation due to shear alignment in the absence of a magnetic field.

3.2 Description of the Model

Deposition of aerosol particles in cylindrical tubes due to gravitational sedimentation can be predicted from the analytical solution given by Heyder and Gebhart (1977). For fully developed, Poiseuille flow through a tube, the fraction of particles depositing in the tube is given by

$$P_{sed} = \frac{2}{\pi}\left(2\kappa\sqrt{1-\kappa^{2/3}} - \kappa^{1/3}\sqrt{1-\kappa^{2/3}} + \arcsin\kappa^{1/3}\right) \tag{3.1}$$

where

$$\kappa = \frac{3v_s L\cos\theta}{4UD} \tag{3.2}$$

in which v_s is the particle settling velocity, U is the average flow velocity through the tube, L is the tube length, D is the tube diameter, and θ is the angle between the tube and the horizontal. Equation (3.1) may be used under the condition that $v_s\sin\theta << U$, which is likely to be satisfied for respirable-sized particles, less than approximately 10 μm in aerodynamic diameter, throughout the lung (Finlay, 2001).

In order to predict sedimentation in peripheral airways of the lung, which are randomly oriented with respect to gravity, P_{sed} should be averaged over all possible angles θ with respect to the horizontal, weighted by the probability of finding an airway at angle θ. For small κ, this weighted-average value of P_{sed} happens to be equal to P_{sed} at $\theta = \arccos(\pi/4)$ (Finlay, 2001), so that deposition fractions in randomly oriented airways can be obtained using $\theta = \arccos(\pi/4)$ in equation (3.1).

For high aspect ratio particles, the settling velocity in equation (3.2) can be determined for a particle at arbitrary orientation with respect to gravity by equating the force of gravity with the drag force, the $\hat{\mathbf{i}}$ component given by equation (2.22) in section 2.5, and then solving for velocity. In the present model, the drag force was modified slightly through inclusion of a slip correction factor for prolate ellipsoids given by Asgharian *et al.* (1988). Particles aligned parallel to randomly oriented airways will have a random orientation with respect to gravity; therefore, an average value of $\arccos(\pi/4)$ should be used for the angle between the particles' long axes and their direction of motion in calculating their settling velocities (Harris and Fraser, 1976). While particles aligned with a magnetic field will have a specific orientation with respect to gravity, in the general case the magnetic field could be generated in any direction, so that a random orientation is assumed in calculating the settling velocities of these particles as well.

Airway deposition due to Brownian diffusion can also be determined from general, analytical solutions in cylindrical tubes. For Poiseuille flow, the solution obtained by Gormley and Kennedy (1949) gives

$$P_{diff} = 6.41\Delta^{2/3} - 4.8\Delta - 1.123\Delta^{4/3} \tag{3.3}$$

where

$$\Delta = \frac{D_d L}{UD^2} \tag{3.4}$$

in which D_d is the particle diffusion coefficient, and equation (3.3) is accurate for $\Delta < 0.1$.

As described in section 2.5, Asgharian *et al.* (1988) determined expressions for the diffusion coefficient of prolate ellipsoids at various orientations. In the present model, these diffusion coefficients are adopted for use in equation (3.4). Particles aligned in parallel with flow streamlines must diffuse in a direction perpendicular to their long axes in order to reach an airway wall; therefore, for this case, the diffusion coefficient for Brownian motion perpendicular to a particle's long axis is used. For particles aligned with a magnetic field at some random orientation with respect to a collection of airways, the diffusion coefficient for random particle orientation is employed.

Methods to predict airway deposition due to impaction and interception have been reported in the past using either theoretical equations (Cai and Yu, 1988) or empirical fits to *in vitro* data (Myojo and Takaya, 2001). The latter equations were fit to deposition data taken for relatively large glass fibers in bifurcations representing the second and third, and third and fourth, lung generations, so that extrapolation to smaller particle sizes and more peripheral lung generations would be somewhat questionable. Accordingly, in the present model the theoretical equations of Cai and Yu (1988) are adopted. The deposition fraction due to impaction was derived by Cai and Yu (1988) through consideration of particle stopping distances in the direction perpendicular to the inner wall of a daughter airway. All particles within one stopping distance from the inner wall as they entered a daughter airway were assumed to deposit. Additional deposition due to interception was estimated by extending the stopping distance by an interception length dependent on the length and orientation of the particle, and the geometry of the bifurcation. Combined deposition due to impaction and interception then took the general form

$$P_{\mathrm{int+imp}} = f\left(\alpha, \frac{D}{D_0}\right)Stk + g\left(\alpha, \frac{D}{D_0}\right)\frac{l}{D} \qquad (3.5)$$

where α is the branching angle between the daughter airways and the parent airway, D is the daughter airway diameter, D_0 is the parent airway diameter, l is the particle length, Stk is a particle Stokes number dependent on particle orientation, the form of f varies for Poiseuille versus plug flow, and the form of g varies for Poiseuille versus plug flow, as well as for particle orientation with respect to the airways. The first term in equation (3.5) is the predicted deposition fraction due to inertial impaction, whereas the second term is that due to interception.

The present model uses the equations given by Cai and Yu (1988) for Poiseuille flow. In calculating particle Stokes numbers, appropriate slip correction factors are included, as was the case for particle settling velocities. Predictions are made for particles aligned parallel to flow streamlines, and for particles at random orientation with respect to the airways.

The total deposition fraction, due to all mechanisms combined, is determined here simply as the sum of deposition fractions due to individual mechanisms. Total deposition fractions are reported in the following section over a range of particle sizes for particles oriented either parallel to flow streamlines, or at random. The latter case is representative of the average deposition estimated for particles aligned with a magnetic field produced across a collection of randomly oriented airways. Predictions are made for deposition occurring at the carinal ridge and in the daughter airways of bifurcations representing the branching between lung generations 9-10, 14-15, and 19-20. For the bifurcation representing generations 9-10, a branching angle of 40° is used, whereas for the other two bifurcations, a branching angle of 50° is used (Hammersley and Olson, 1992). The lengths and diameters of the airways are those given by the idealized lung model of Finlay *et al.* (2000), and the flow rate entering the parent airway is determined for an inhalation flow rate of 300 cm^3/s under the assumption of symmetric branching, and ventilation, throughout the lung.

3.3 Results and Discussion

Figures 3.1a, 3.2a, and 3.3a display predicted deposition fractions in bifurcations representing lung generations 9-10, 14-15, and 19-20, respectively. Predictions are given for unit density particles with diameters of 0.2, 0.5, and 1 μm, and lengths ranging from 1 to 40 μm. For particles oriented parallel to flow streamlines, increasing length has only a small effect on deposition, due to the relatively weak dependence of high aspect ratio

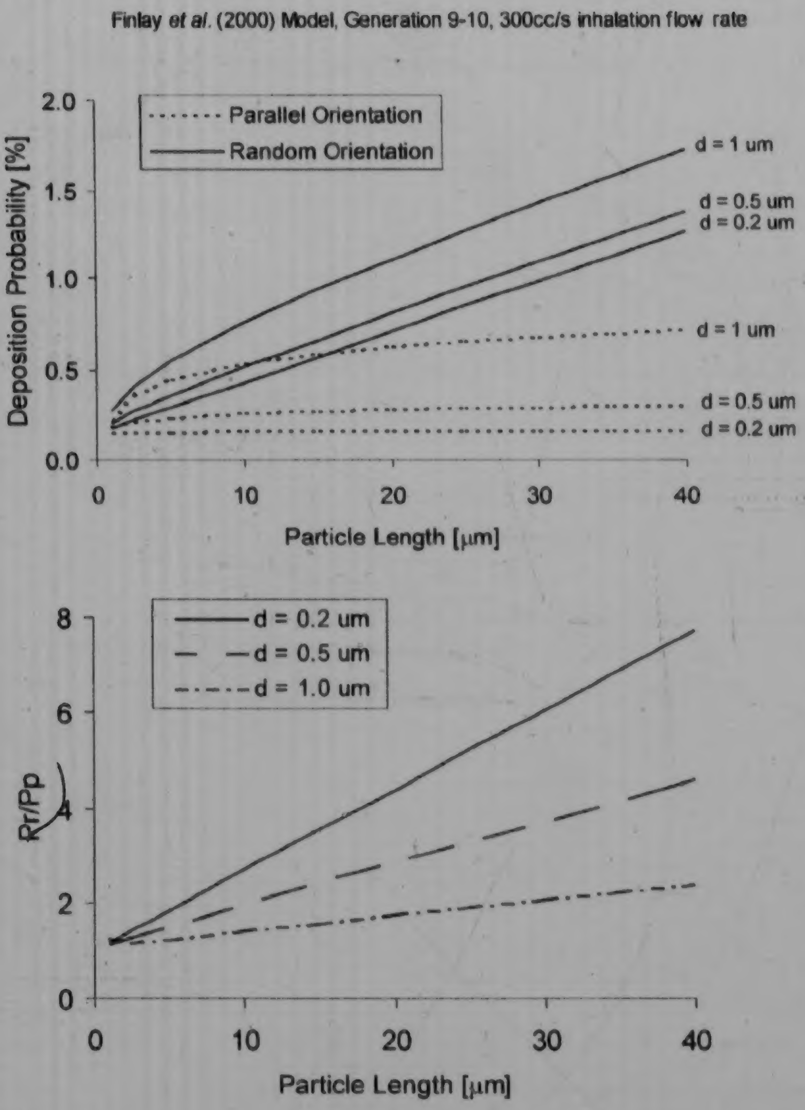

Figure 3.1. Deposition probabilities for high aspect ratio particles of varying length and diameter in an airway bifurcation representing the branching between lung generations 9 and 10. Absolute probabilities for both parallel and random particle orientations are plotted in the upper graph, whereas the lower graph displays the ratio between predicted probabilities for these two orientations.

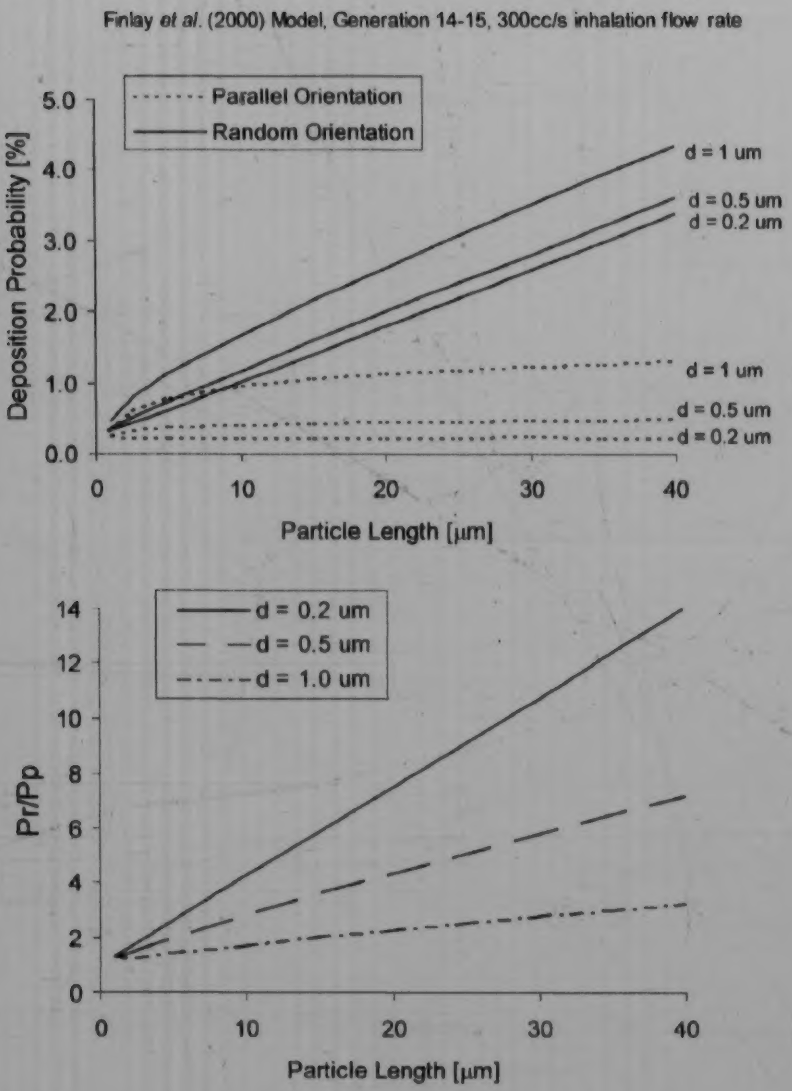

Figure 3.2 Identical to figure 3.1, but for lung generations 14 and 15.

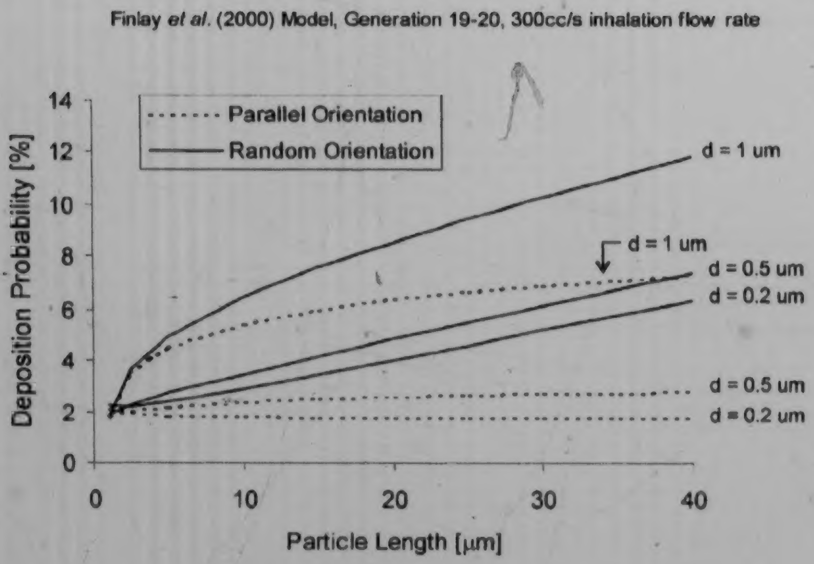

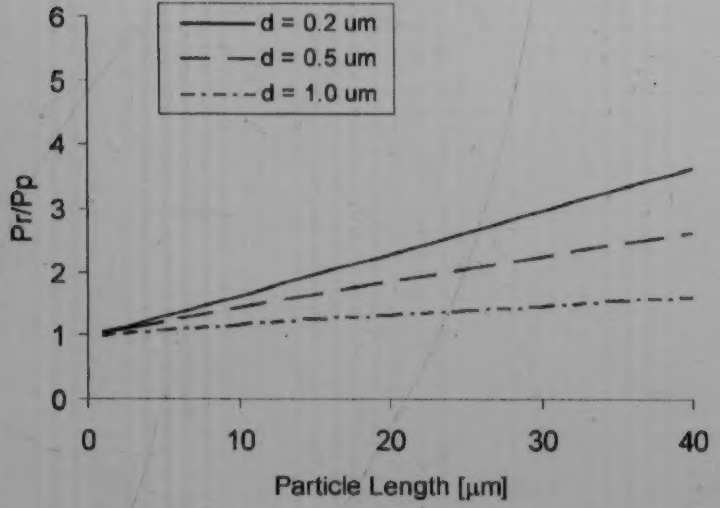

Figure 3.3. Identical to figures 3.1 and 3.2, but for lung generations 19 and 20.

particle Stokes numbers, settling velocities, and diffusion coefficients on particle length. In contrast, deposition of randomly oriented particles increases almost linearly with length, owing to the interception mechanism. As an example, figure 3.4 displays deposition fractions due to individual mechanisms in the three modeled bifurcations for a particle with diameter of 0.5 μm and length of 10 μm. Clearly, deposition changes very little between the two orientations studied for all mechanisms except for interception. Figure 3.4 also indicates that the effect of interception on deposition relative to other mechanisms will reach a maximum somewhere around the boundary between the

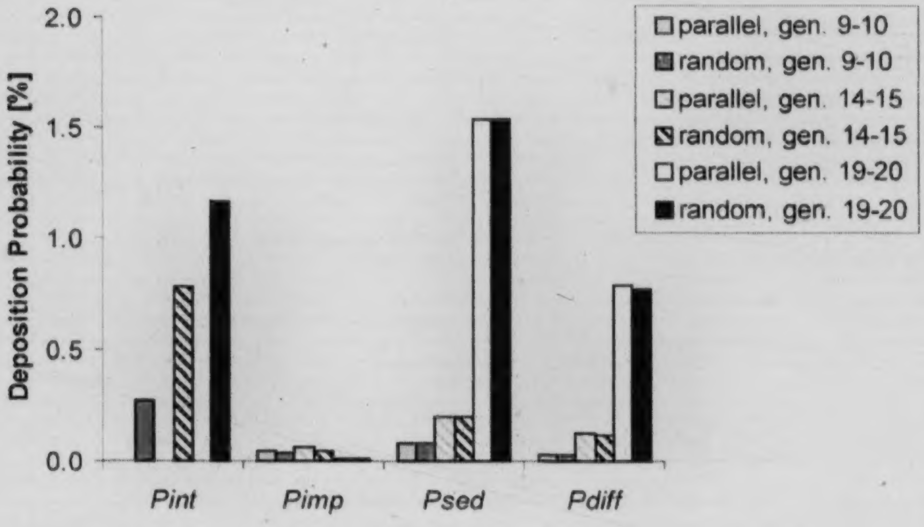

Figure 3.4. Deposition probabilities due to interception (P_{int}), impaction (P_{imp}), sedimentation (P_{sed}), and diffusion (P_{diff}) for a particle with diameter of 0.5 μm and length of 10 μm in different lung generations.

tracheobronchial and alveolar regions of the lung, which is located between generations 14-15 in the Finlay *et al.* (2000) model. In more proximal generations (that is, closer to the trachea) airway diameters are significantly larger, so that interception is reduced, whereas in more distal generations, particle residence times in airways become much longer, allowing time for particles to deposit in greater fractions due to sedimentation and diffusion. In considering this latter effect, however, it should be kept in mind that the present predictions have been made for an inhalation flow rate consistent with tidal breathing. For the higher inhalation flow rates often observed in patients using single breath inhalers, particle residence times in distal airways would decrease, as would the relative effects of sedimentation and diffusion on deposition.

Of particular interest to the present thesis is the ratio between deposition fractions predicted for randomly oriented particles and particles aligned in parallel with flow streamlines. This ratio is plotted in figures 3.1b, 3.2b, and 3.3b for the three different bifurcations. The results discussed above for the 0.5 μm by 10 μm particle of figure 3.4 are qualitatively the same over a fairly broad range of particle sizes. That is to say, ratios between deposition fractions for random and parallel orientations are predicted to be larger in the bifurcation representing generations 14 and 15 than in the other two bifurcations considered. Even so, if particle diameters and lengths are optimized, control over particle orientations is predicted to increase deposition by a considerable amount in airways spanning a large portion of the peripheral lung. Consequently, the use of magnetic alignment to alter high aspect ratio particle orientations appears to be a feasible means through which to influence their deposition in the lung.

4. MAGNETIC ALIGNMENT AND SMALL AIRWAY DEPOSITION

4.1. Introduction

Based on the theoretical predictions presented in the previous chapter, control over the orientation of high aspect ratio particles in the small, peripheral airways of the lung is expected to influence their deposition. Given that elongated particles in shear flow have a natural tendency to align parallel to the direction of flow through an airway, and therefore also parallel to airway walls, alignment with a magnetic field to any other orientation can be expected to increase deposition due to interception. As proposed in chapter 2, control over particle orientations in the peripheral airways of the lung can likely be achieved by loading the high aspect ratio particles with smaller, magnetic particles, and then using an externally applied, low-gradient magnetic field to align the composite particles. The present chapter describes *in vitro*, proof of concept experiments used to explore this approach.

4.2. Experimental Methods

4.2.1. Preparation of Drug and Magnetite Suspensions

In these initial studies, cromoglycic acid was identified as a model drug, owing to the availability of published methods for preparing high aspect ratio cromoglycic acid crystals in a size range appropriate for aerosol delivery (Chan and Gonda, 1989). Cromolyn sodium salt (minimum 95%) was purchased from Sigma-Aldrich Canada (Oakville, ON). High aspect ratio particles of cromoglycic acid (CA) were prepared by crystallization according to the method of Chan and Gonda (1989). Dried CA powders were dispersed by pipette in deionized water to yield suspensions containing 2 mg CA/ml water. Superparamagnetic magnetite particles were prepared by precipitation following the method of Cheng *et al.* (2005). Transmission electron micrographs confirmed that the magnetite particles were reasonably monodisperse in diameter, with a mean diameter of about 10 nm, as was also reported by Cheng *et al.* (2005). Magnetite was added to the CA suspensions by one of two methods: in the first, dilute suspensions of magnetite in deionized water were sonicated for 30 minutes to deaggregate the magnetite particles as much as possible, then these suspensions were used to disperse the CA powders. In the second method, the magnetite was added in the last stage prior to crystallization of CA, and then the combined CA/magnetite powders were dispersed in deionized water. In either case, the concentration of magnetite in suspension ranged from approximately 0.2 to 0.4 mg/ml over several preparations. Figure 4.1 is a TEM image of a drop of

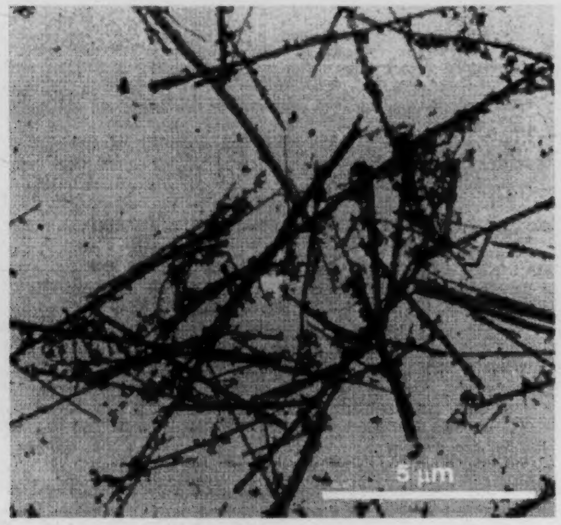

Figure 4.1. TEM image of a co-suspension of CA and magnetite. The long particles are CA, while the black dots are clusters of magnetite nanoparticles.

CA/magnetite (added pre-crystallization) suspension allowed to dry on a TEM grid.

4.2.2. Droplet Size Measurements

CA and CA/magnetite suspensions were aerosolized using Hudson Updraft II jet nebulizers (Hudson Respiratory Care, Inc., Temecula, CA) driven by a PulmoAide compressor (5650C; DeVilbiss Canada, Barrie, ON). Although some very long CA particles, with lengths on the order of tens of micrometers, were observed in scanning electron microscope (SEM) (S-2500; Hitachi, Japan) images of dried suspensions, it was anticipated that the droplet sizes produced by the nebulizer would limit the length of CA particles that could be aerosolized. In order to examine the sizes of CA particles contained in droplets produced by the nebulizers, droplets were collected at nebulizer mouthpieces onto 0.2 μm pore size polycarbonate membranes (Isopore GTTP04700; Millipore, Billerica, MA) for subsequent analysis by SEM. The droplet size distribution produced by the nebulizers was measured by phase Doppler anemometry (PDA; Dantec Measurement Technology, Denmark). In order to limit evaporation of droplets during transit from the nebulizer to the PDA measurement volume, the nebulizer T-piece was plugged with a rubber stopper at one end, and the other end was connected to a closed, windowed measurement chamber. This experimental setup is shown schematically in figure 4.2. For three different nebulizers, each containing 3 ml of the CA suspension, droplet sizes were measured over ten seconds at the start of every minute until nebulization ceased.

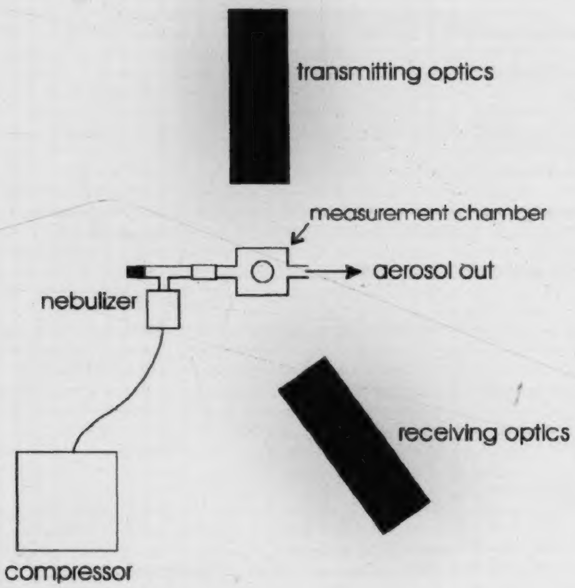
transmitting optics
measurement chamber
aerosol out
nebulizer
receiving optics
compressor

Figure 4.2. Schematic of the experimental setup for measuring nebulizer droplet size distributions using phase Doppler particle analysis.

4.2.3. Penetration through Polycarbonate Membranes

At an early stage in these studies, before conducting time intensive measurements of particle size distributions and deposition experiments in model airway bifurcations, some demonstration of magnetic alignment of the composite CA/magnetite aerosols was desired. For this purpose, formulations of CA, CA with magnetite added post-crystallization, and CA with magnetite added pre-crystallization, were nebulized using jet nebulizers (Up-Draft II; Hudson Respiratory Care, Inc., Temecula, CA) driven by compressor (PulmoAide 5650C; DeVilbiss Canada, Barrie, ON), and drawn along with ambient, drying air at 10 l/min. into a large volume (~ 16 l) delivery chamber. Evaporation of the nebulized droplets left behind an aerosol of CA particles, and, for the two formulations containing magnetite, allowed free magnetite particles not attached to CA particles in suspension to adhere to them upon drying of the droplet, although a very small fraction of the magnetite in suspension was likely nebulized in extremely small droplets that do not contain CA particles.

As a test of particle alignment with an external magnetic field, aerosols produced from each of the three formulations were drawn from the delivery chamber through polycarbonate track-etched membrane filters with pore size of 5 μm and diameter of 47 mm (Isopore TMTP; Millipore, Billerica, MA). The membrane filters were sealed tightly within an in-house filter casing, and the flow rate through the membrane was monitored to within 0.21 ± 0.02 l/min. with a low flow rate rotameter (FL-2010; OMEGA Canada, Laval, QC). A bacterial air filter (Respirgard; Vital Signs, Inc., Totowa, NJ) was placed downstream from the membrane to capture the aerosol that penetrated the membrane.

The masses of CA collected on the membrane and the bacterial filter were measured by washing with 0.01 N sodium hydroxide, to convert the CA to its sodium salt, and subsequent assay by UV spectrophotometry (8452A; Hewlett-Packard, Palo Alto, CA) at a wavelength of 326 nm. Penetration efficiency, calculated as the mass of CA recovered from the bacterial filter as a percentage of the total challenge mass recovered from both filters, was determined for each formulation, with and without the presence of a magnetic field across the membrane filter. The magnetic field was produced parallel to the face of the membrane by placing neodymium permanent magnets (2" x 2" x 0.5" N42; Indigo Instruments, Waterloo, ON) on either side of the filter casing. The flux density at the center of the membrane was measured using a gauss meter (F.W. Bell 5180; Sypris Test and Measurement, Orlando, FL) to be 90 mT. As penetration efficiencies were dependent on the total challenge mass recovered from both filters, the challenge mass was varied over multiple experimental runs by allowing the sample time to range from 20 to 90 minutes. In addition to measurement of penetration efficiencies, images of the membrane filters were obtained by SEM, so as to observe particle orientations with and without the magnetic field present.

4.2.4. Nebulization Efficiency

In order to determine any effect of added magnetite on nebulization efficiency, CA and CA/magnetite suspensions were aerosolized again using Hudson Updraft II jet nebulizers driven by a PulmoAide compressor. In this and subsequent sections, the CA/magnetite suspension studied is that prepared with the magnetite added prior to crystallization of CA. Nebulization efficiency, defined here as the mass percentage of CA successfully nebulized, compared to the initial mass of CA in the nebulizer, was determined for 3 ml nebules. A T-piece was attached to the nebulizer, and an absolute filter (Respirgard; Vital Signs, Inc., Totowa, NJ) was placed at one end. A continuous flow of 10 l/min. was maintained by vacuum pump through the T-piece towards the filter, ensuring that no aerosol escaped through the opposite end. Nebulizers were run until their output became intermittent, and the same three nebulizers were tested for each formulation. The masses of CA captured on the filter, and remaining in the nebulizer and T piece, were determined by UV spectrophotometry.

4.2.5 Aerosol Particle Size and Concentration

The particle size distribution and number concentration of CA and CA/magnetite aerosols were determined from samples taken from essentially the same delivery apparatus as used for the membrane penetration experiments, with the addition of an aerosol neutralizer (3054; TSI, St. Paul, MN) inline between the nebulizer and chamber. Suspensions of CA and CA/magnetite were nebulized, and drawn by vacuum pump along with ambient, drying air at 10 l/min. into the delivery chamber for 1.5 minutes. With reference to figure 4.3, after filling the delivery chamber with aerosol, valves connecting to the nebulizer and the vacuum pump were closed, and a butterfly valve at the base of the chamber was opened. Aerosol was then sampled from the base of the chamber onto a 0.2 μm pore polycarbonate membrane (Isopore GTTP04700; Millipore, Billerica, MA) for 1 hour at a flow rate of 0.21 l/min., maintained through the delivery chamber using dry, compressed air and a needle valve, and monitored using a low flow rate rotameter (FL-2010; OMEGA Canada, Laval, QC). Over the period of the sampling, the needle valve was adjusted as required to hold the flow rate to within 0.21 ± 0.02 l/min.

After collecting aerosol from the delivery chamber, samples of the polycarbonate membranes were prepared for analysis by SEM. For both the CA and CA/magnetite aerosols, three pieces were cut from the membrane, from locations chosen at random, and mounted to SEM stubs using two-sided carbon adhesive tabs. These samples were sputter coated with a thin layer of gold prior to SEM analysis. Images of the samples were taken at 3000x magnification, again from locations chosen at random, and stored digitally.

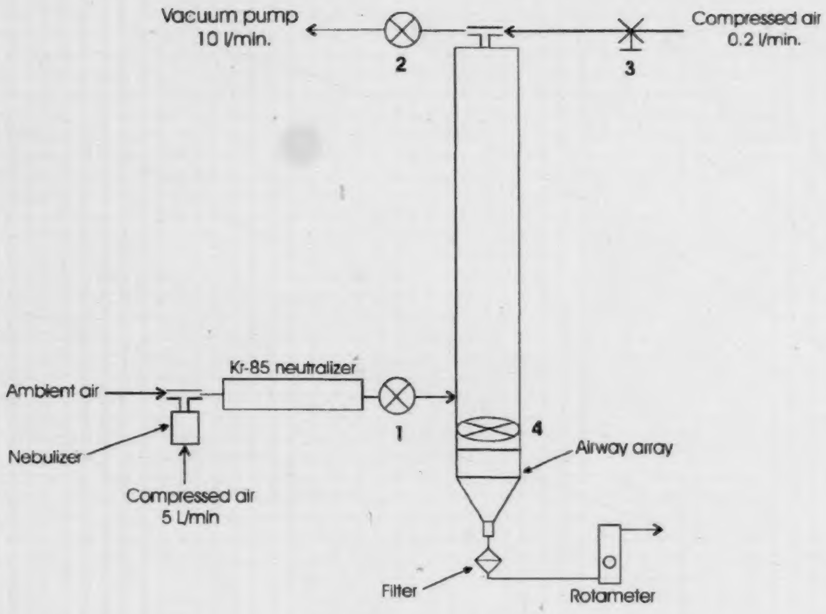
Vacuum pump
10 l/min.
2
Compressed air
0.2 l/min.
3
Kr-85 neutralizer
Ambient air
Nebulizer
Compressed air
5 L/min
1
4
Airway array
Filter
Rotameter

FIGURE 4.3. An apparatus for measuring the aerosol deposition in an array of small airway bifurcations. To fill the delivery chamber with aerosol, valves 1 and 2 were open, and valves 3 and 4 were closed. To drain the chamber, this was reversed. For particle size measurements, the airway array was removed, and valve 4 at the base of the chamber was opened. Aerosol was then sampled from the base of the chamber onto a 0.2 μm pore polycarbonate membrane.

For three SEM images from each of the three membrane samples, the length and diameter of each particle was manually measured using digital image analysis software (Scion Image; Scion Corporation, Frederick, MD). The particles were assumed to lie parallel to the face of the membrane. Particle sizing rules were similar to those established for asbestos samples by Platek et al. (1992). Each particle was marked immediately after being sized so as to avoid sizing the same particle twice. Where a particle was not perfectly straight, its length was measured as the arc length along its central axis from one tip to the other. Diameter was measured perpendicular to the central axis at the midpoint along a particle's length, except in rare cases where the particle had two regions of clearly different diameter. In these latter cases, an average of the two diameters was taken. Overlapping particles were sized separately only if both ends of each particle were clearly visible.

After sizing, the volume of each particle was calculated, under the approximation that the particles were cylindrical. Volume-weighted size distributions were then fit with lognormal curves by nonlinear regression to yield a volume median length (VML), volume median diameter (VMD), and geometric standard deviations in both length and diameter (σ_L and σ_D, respectively) for each SEM image. In addition, the particle number concentration in the sampled air was calculated for each image from the number of particles counted, the volume of sampled air, and the ratio between the image area and the total area of the membrane exposed to the aerosol. The mean values of these parameters for the three different membrane samples were compared by one-way

ANOVA for independent samples in order to gauge their variation over different locations on the membrane.

4.2.6 Design of Small Airway Array

In order to provide experimental evidence that magnetic alignment can be used to increase small airway deposition of high aspect ratio particles, *in vitro* aerosol deposition experiments were performed in an array of small, bifurcating airways. As designed, parent and daughter airway diameters were 0.5 mm, and the branching angle of each daughter airway was 50°. The length of the parent airways was 8 mm, and that of the daughter airways was 2 mm. The radius of curvature between the parent and daughter airways was 1 mm, while that of the carinal ridge was 0.05 mm. These airway dimensions were chosen to be representative of those found in the terminal bronchioles of the human lung (Olson, 1971; Horsfield et al., 1971; Hammersley and Olson, 1992; Finlay, 2001; Sauret, 2002), with the exception of the parent to daughter diameter ratio, and the length of the parent airway. A parent to daughter diameter ratio of 1 is somewhat lower than is anatomically realistic; however, an equal diameter for the parent and daughter airways simplified machining of the airways considerably. Likewise, the long parent airways were required in order to maintain the dimensions of the model above a minimum workable size. Figure 4.4 is a scale drawing of the bifurcation design.

A major challenge in the experimental design was to step down from the relatively high flow rate required to nebulize and dry the aerosols (10 l/min.) to much smaller flow rates typical of the peripheral airways in the lung. The flow rate through a terminal bronchiole

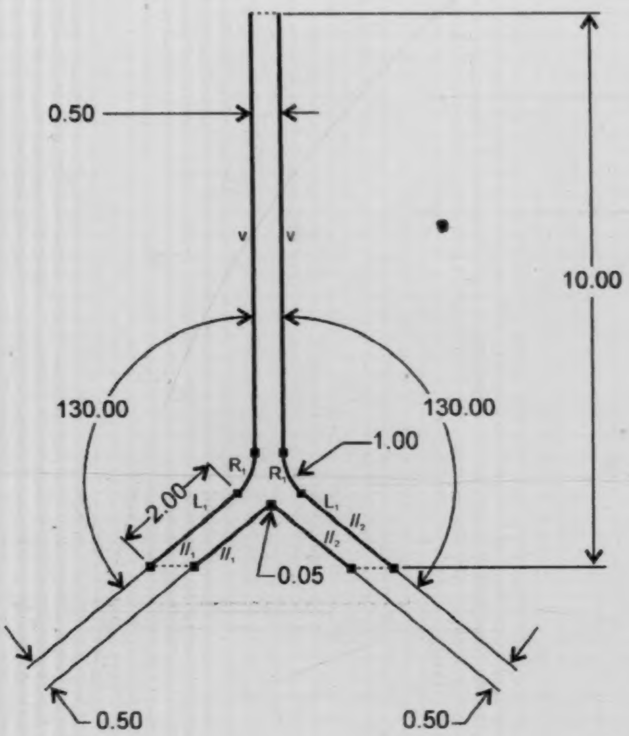
0.50
v
v
10.00
130.00
130.00
1.00
R1
R1
2.00
L1
L1
//1
//1
//2
//2
0.05
0.50
0.50

Figure 4.4. Scale drawing of the bifurcation design. All lengths are in millimeters, and angles are in degrees.

during tidal breathing is approximately 0.02 cm^3/s, or 1.1 x 10^{-3} l/min. As such, to divert such a small fraction of the aerosol-laden flow produced by the nebulizer through a single bifurcation would be extremely wasteful. For this reason, aerosol was collected from the nebulizer into a large volume delivery chamber, and then drawn from the chamber at a much lower flow rate through a parallel array of bifurcations. Using an array of bifurcations, as opposed to a single bifurcation, served the dual purpose of allowing a higher flow rate to be used to draw aerosol from the chamber, while ensuring that the total deposited mass of CA recovered from all bifurcations in the array was large enough to assay by UV spectrophotometry. While aerosol was certainly lost in the delivery chamber, the losses were estimated to be considerably lower than if a small fraction of flow drawn from the nebulizer was diverted continuously through the array.

To build the airway array, a row of nine semicircular cross-section, bifurcating channels was cut into both sides of thirteen 3 mm thick strips of aluminum, and into one side of each of two thicker end pieces, using a computer numerical control (CNC) milling maching. As seen in figure 4.5a, on a given strip, each parent airway was separated by 5 mm from its neighbors on either side. The strips of aluminum were stacked together to form a 9 by 14 array of circular cross-section bifurcations, depicted schematically in figure 4.5b. Brass dowels were used to align the stacked strips. The surfaces of the strips were lapped, and screws at either end of the dowels held the stack together to ensure an airtight seal between neighboring surfaces.

After machining the channels, their dimensions were measured by analysis of digital images taken through a stereomicroscope coupled with a digital camera (DXM 1200; Nikon, Japan) at 100x magnification. Within the resolution of the measurements (± 0.01 mm for lengths and ± 2° for angles) neither the airway lengths nor the branching angles varied from the design parameters. Measurements of channel widths and radii of

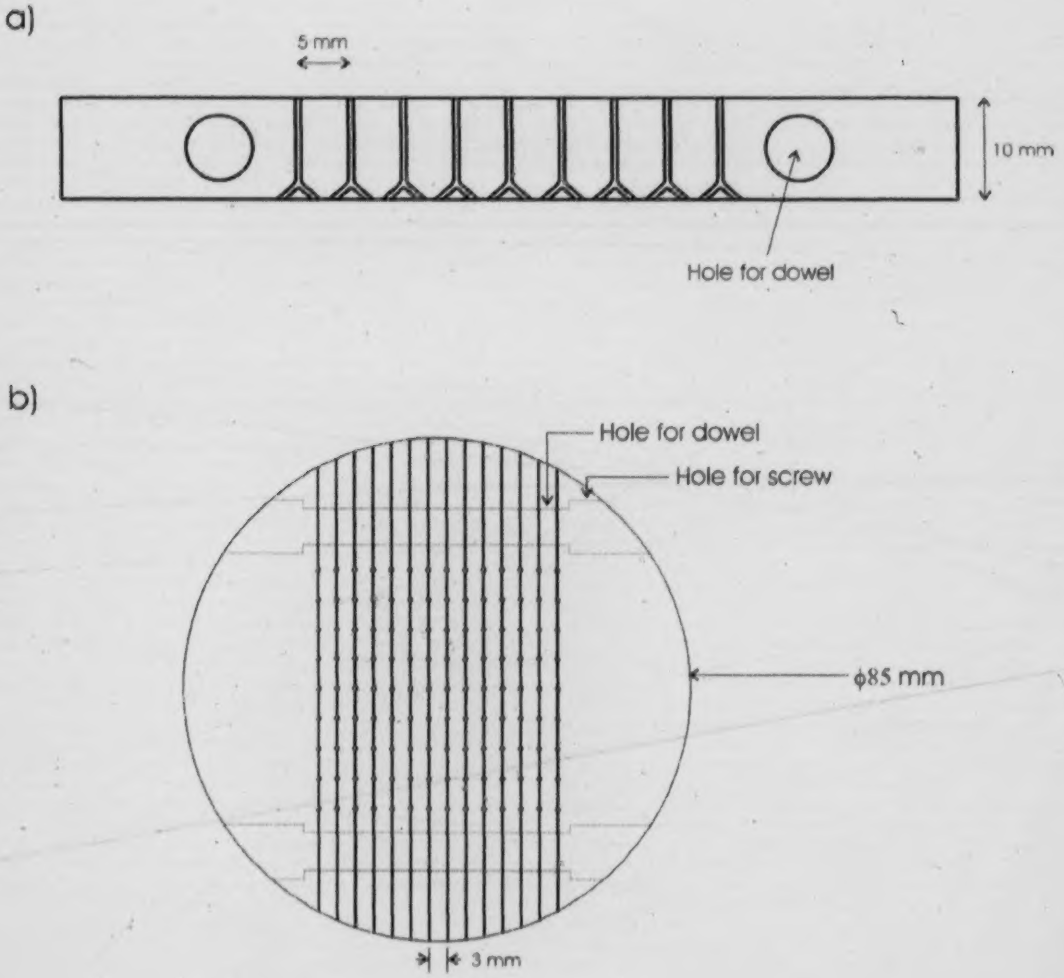
a)
5 mm
10 mm
Hole for dowel
b)
Hole for dowel
Hole for screw
ϕ85 mm
3 mm

FIGURE 4.5. a) Side view of semicircular cross-section, bifurcating channels cut into a strip of aluminum. b) Top view of the airway array formed by stacking the aluminum strips.

curvature were taken for two bifurcations from each of five strips chosen at random. The average parent airway width was 0.53 ± 0.03 mm (mean ± one standard deviation, n = 10), while the average daughter airway width was 0.51 ± 0.02 mm (n = 20). The average radius of curvature between parent and daughter airways was 0.79 ± 0.07 mm (n = 20). Carinal ridges were observed to be very sharp, to an extent that their radii of curvature could not be accurately measured. The depths of the channels were measured by stacking and securing the strips to form the airway model, and then, from a top view of the model, measuring the diameter of airways formed between channels of opposing strips in the direction perpendicular to the faces of the strips. The average airway diameter measured in this manner was 0.52 ± 0.04 mm (n = 36).

As described in chapter 2, Finlay *et al.* (2000) have previously proposed a symmetric model of the human lung geometry based on tracheobronchial airway data analyzed by Phillips *et al.* (1994) and alveolar data from Haefeli-Bleuer and Weibel (1988). In this model, the terminal bronchioles occur at the 14th generation of the lung, where the generation number of a particular airway refers to the number of branches separating that airway from the trachea. Assuming that the bifurcations in the airway array used in the present study represent branching from the 14th to the 15th lung generation, and that the flow through the array divides evenly into the 126 parent airways, a flow rate of 0.21 l/min. through the array would correspond to an inhalation flow rate of 27.3 l/min. at the trachea. Alternatively, Phillips et al. (1994) favor a diameter-based reconstruction of the conducting airways, wherein the average velocity through a 0.5 mm diameter airway is approximately 10% of the average velocity through the trachea. With this approach, assuming a tracheal diameter of 1.8 cm (Finlay et al., 2000), the flow rate through the array corresponds to a somewhat lower inhalation flow rate of 21.6 l/min. at the trachea, which is very close to the typical value of 18 l/min. given by Finlay (2001) for adult males breathing tidally through a mouthpiece.

4.2.7. Small Airway Deposition

The experimental apparatus used to measure aerosol deposition in the airway array was identical to that from which aerosol was sampled for particle size measurements, except that the airway array was placed in an aluminum holder positioned at the base of the delivery chamber, as is depicted in figure 4.3. The array was sealed in the holder using vacuum grease. In this position, the parent airways were oriented parallel to the direction of gravity. An absolute filter (Respirgard; Vital Signs, Inc., Totowa, NJ) was placed downstream from the array holder to collect aerosol particles that escaped deposition in the airways. For each experimental run, a CA or CA/magnetite suspension was nebulized, and drawn with additional drying air into the delivery chamber at 10 l/min. for 1.5 minutes. Next, valves connecting to the nebulizer and the vacuum pump were closed, and the butterfly valve at the base of the chamber was opened. Compressed, dry air was then used to maintain a continuous flow of air from the delivery chamber through the airway array for 1 hour, at a flow rate of 0.21 ± 0.02 l/min. As in the particle sizing procedure, the flow rate was monitored using a rotameter. Because the deposition efficiency in the airway array was low, this cycle of filling the delivery chamber and then draining it through the array was repeated twelve times for each experimental run in order to allow a measurable mass of CA to deposit in the array. Three experimental runs were performed for both CA and CA/magnetite with no magnetic field in place, and another three runs were performed for CA/magnetite with a magnetic field aligned across the array, that is, perpendicular to the parent airways.

The magnetic field was generated using neodymium permanent magnets (2" x 2" x 0.5" N42; Indigo Instruments, Waterloo, ON). Pairs of 0.5" thickness magnets were stacked to form two 1" thickness magnets. These two magnets were positioned 13.5 cm apart, so that the center point between them matched the center of the airway array, and the magnetic field was produced perpendicular to the parent airways in the array. The magnetic flux density was measured in the central plane over the region of the airway array using a gauss meter (F.W. Bell 5180; Sypris Test and Measurement, Orlando, FL).

The masses of CA deposited in the array, the array holder, and the downstream filter were determined by washing with 0.01 N sodium hydroxide and subsequent assay by UV spectrophotometry. The deposition efficiency in the array was calculated as the mass of CA deposited in the array as a percentage of the total mass of CA recovered from the array, the holder, and the downstream filter. Only the section of the holder downstream from the array was washed. As the top surface of the array was exposed to the delivery chamber during the experiments, prior to washing the array any aerosol that had settled onto the surface was removed. This was accomplished first using masking tape to repeatedly lift CA off the surface, and then by cleaning the surface with cotton swabs dipped in 0.01 N sodium hydroxide.

4.3. Results

4.3.1. Droplet Size Measurements

Figure 4.6 is a SEM image of CA particles that were successfully nebulized. Droplets produced by the nebulizer were collected onto a polycarbonate membrane filter placed at the nebulizer mouthpiece, after which the water from the droplets evaporated. Clearly, many long particles, up to approximately 30 μm in length, left the nebulizer.

The nebulizer droplets size distributions measured by PDA are shown in figure 4.7 as cumulative, normalized volume distributions. No significant change in droplet sizes was observed over the course of nebulization; therefore, the distributions presented in figure 4.7 are averaged over the complete nebulization time for each experimental run. It is evident in figure 4.7 that nearly all droplets produced by the nebulizers were less than 20 μm in diameter; accordingly, it was initially surprising that CA particles longer than 20 μm exited the nebulizer. However, the initial droplets produced by jet nebulizers are generally estimated to be between about 50 and 100 μm in diameter (Finlay, 2001). These droplets are directed at high speed towards a baffle, where they splash and form smaller droplets. It is therefore possible that the long particles visible in figure 4.6 were suspended in large droplets during their initial production, and then were released into the air during splashing. As these particles have small aerodynamic diameters, dependent mainly on their diameters and only weakly on their lengths, they would easily maneuver secondary baffles used within the nebulizer to filter out secondary droplets above a respirable size. Alternatively, given the curved nature of many of the longer particles visible in figure 4.6, it is possible that they were able to fit inside droplets exiting the

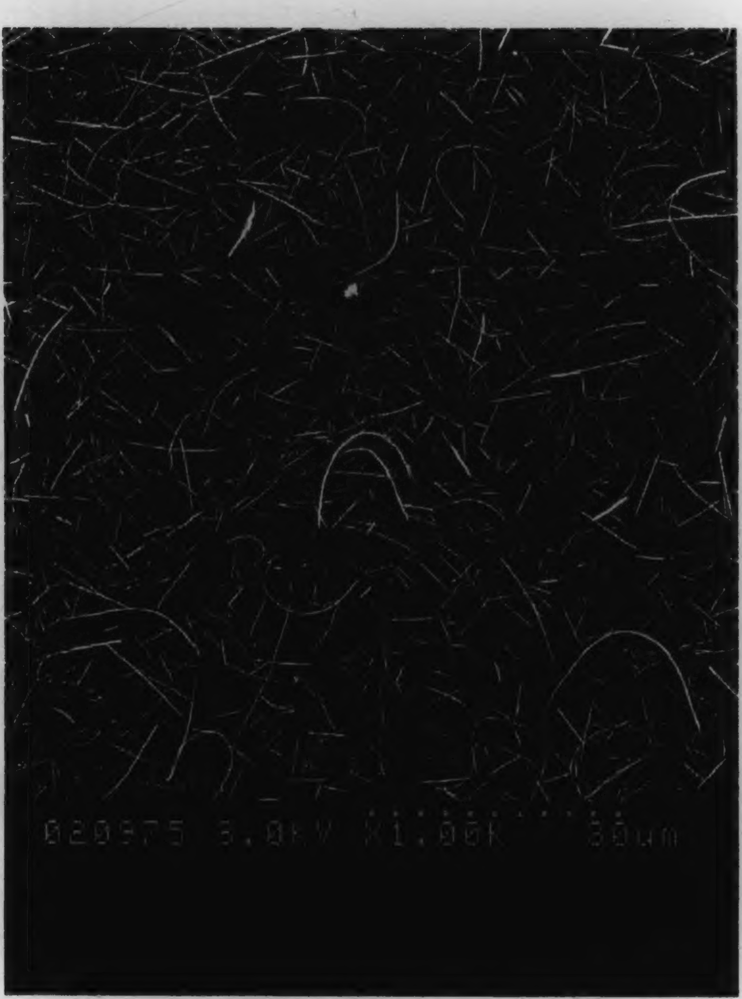
020975 5.0kV X1.00K 30um

Figure 4.6. SEM image of CA particles collected onto a 0.2 μm polycarbonate membrane filter placed at the exit of the nebulizer mouthpiece.

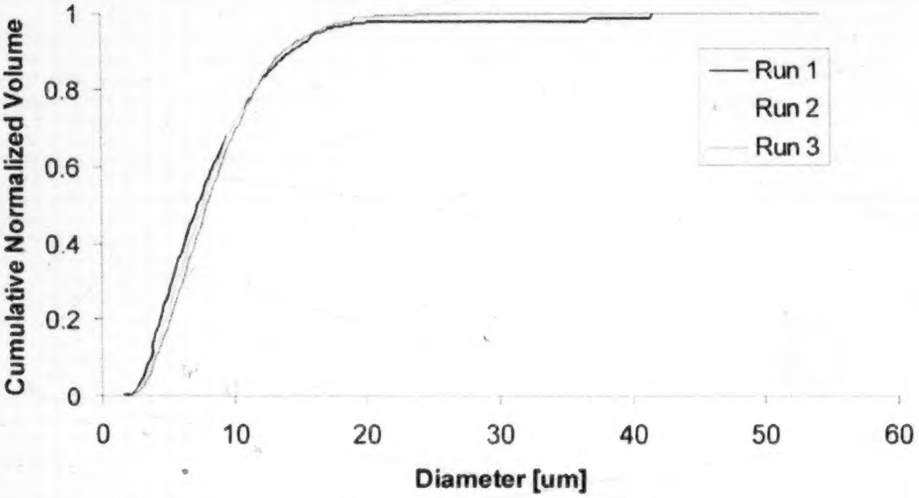

Figure 4.7. Cumulative, normalized volume distributions for droplets produced by the jet nebulizers containing 2 mg/ml suspensions of CA.

nebulizer. However, it is unclear from figure 4.6 whether the observed curvature reflects the original shapes of CA particles in suspension, curling of the particles that occurred as primary droplets pinched off from the air-water interface, or curling that occurred as the sample dried on the polycarbonate membrane.

4.3.2. Penetration through Polycarbonate Membranes

In an effort to demonstrate early on that magnetite loaded high aspect ratio particles would align, in the air, in the direction of a magnetic field, penetration through 5 μm pore size polycarbonate membrane filters was measured for CA particles, and the two different preparations of CA/magnetite particles, with and without a magnetic field produced parallel to the face of the membrane. Figure 4.8 displays measured penetration efficiencies versus the challenge mass of CA for the three aerosols over a number of experimental runs, with and without the magnetic field. The pores of the membrane filters began to plug with particles at fairly low mass loadings, so that measurements could only be obtained for small challenge masses, between approximately 50 and 150

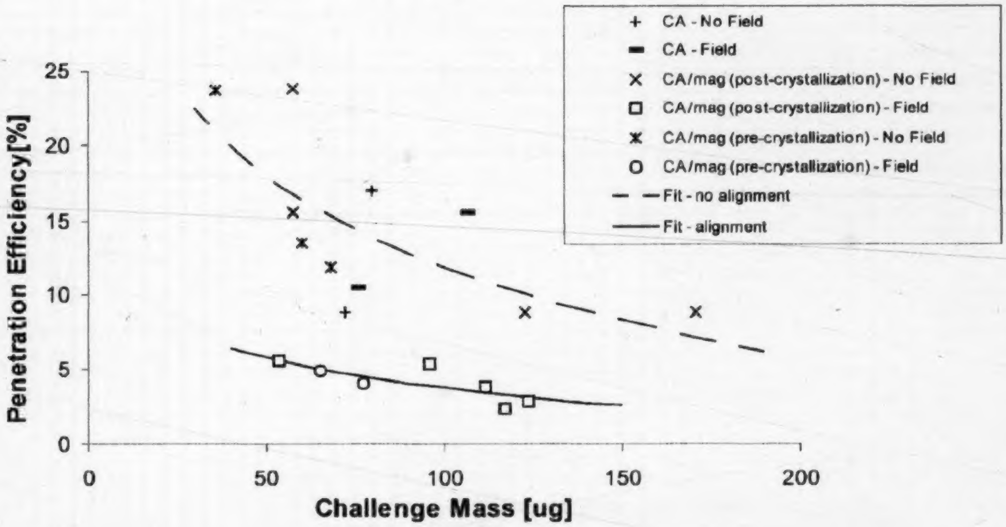

Figure 4.8. Penetration efficiency through 5 μm pore size polycarbonate membrane filters is plotted against challenge mass for CA and CA/magnetite aerosols. Best fit logarithmic curves are shown for those cases where magnetic alignment was expected, and for those where no alignment was expected.

μg. Figure 4.8 clearly indicates that in the two cases where alignment of particles was expected, that is, for the two CA/magnetite aerosols with the magnetic field present, penetration efficiencies were consistently lower than those for the other cases, where no alignment was expected.

In order to make a statistical comparison, penetration efficiencies were considered only for challenge masses between 57 to 106 μg. For each of the six experimental conditions given in figure 4.8, two data points fell within this range. Average penetration efficiencies within the range are given in table 4.1. For each of the three aerosols, there was no statistically significant difference between the average challenge masses with and without the magnetic field ($P > 0.4$ in all cases; two tailed student's *t*-test for independent samples). Average penetration efficiencies with and without the magnetic field were

Table 4.1. Penetration Efficiencies Through 5 μm Pore Size Polycarbonate Membrane Filters with and without Magnetic Fields.

Formulation	**Penetration Efficiency (%)**	
	No field	With field
Cromoglycic Acid (CA)	12.9 ± 5.8	13.0 ± 3.6
CA with magnetite added post-crystallization	19.6 ± 5.8	5.5 ± 0.1
CA with magnetite added pre-crystallization	12.7 ± 1.2	4.5 ± 0.6

All entries expressed as mean ± one standard deviation, n = 2.

compared for each aerosol using directional, one-tailed student's *t*-tests for independent samples (under the assumption that magnetic alignment would decrease the penetration efficiency). As expected, for the formulation of CA alone, there was no significant difference in the penetration of aerosol particles through the membrane with and without the magnetic field. In contrast, for both the formulations containing magnetite, penetration efficiency decreased significantly ($P < 0.05$) when the magnetic field was produced across the face of the membrane. While neither of the two methods for preparing CA/magnetite particles proved clearly superior to the other in terms of reducing penetration through the membranes, from a handling perspective, adding the magnetite prior to crystallization of CA creates as an end product a powder that needs only to be dispersed in water prior to nebulization. For this reason, in preparing CA/magnetite particles used in all further experiments reported in this thesis, magnetite was added before the crystallization of CA. Figure 4.9 shows scanning electron micrographs of CA/magnetite particles captured on membranes with and without the magnetic field produced across the face of the membranes. In either case, individual aerosol particles formed clusters as they were captured at pore sites. Particle alignment in the direction of the magnetic field is clearly visible in figure 4.9b, and, at higher magnification, in figure 4.10.

4.3.3. Nebulization Efficiency

The measured nebulization efficiencies and run times for CA suspension with and without added magnetite are listed in table 4.2. Clearly, for the three Updraft II

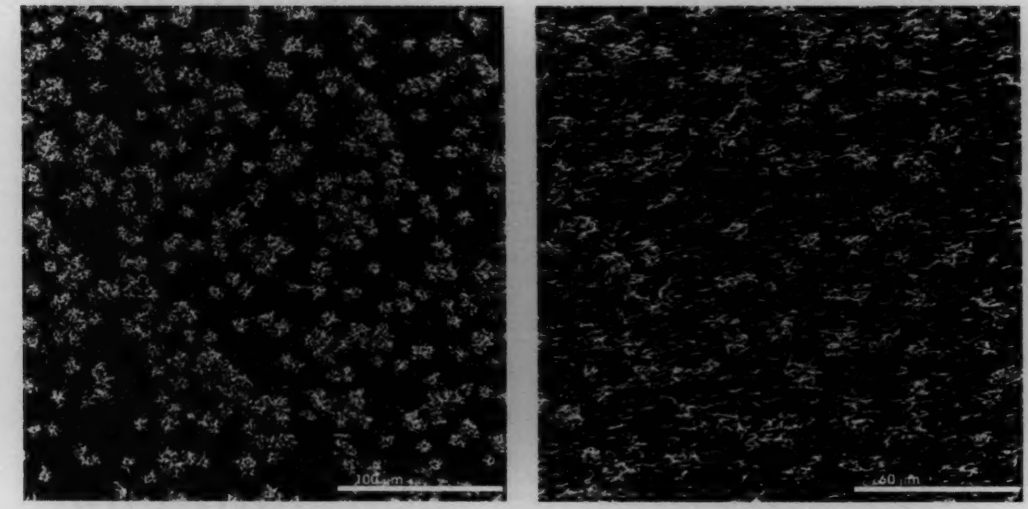

(a) (b)

Figure 4.9. CA particles loaded with magnetite captured in the pores of a 5 µm pore size polycarbonate membrane (a) without a magnetic field across the face of the membrane, and (b) with a magnetic field. As they were captured, individual aerosol particles formed clusters at pore sites.

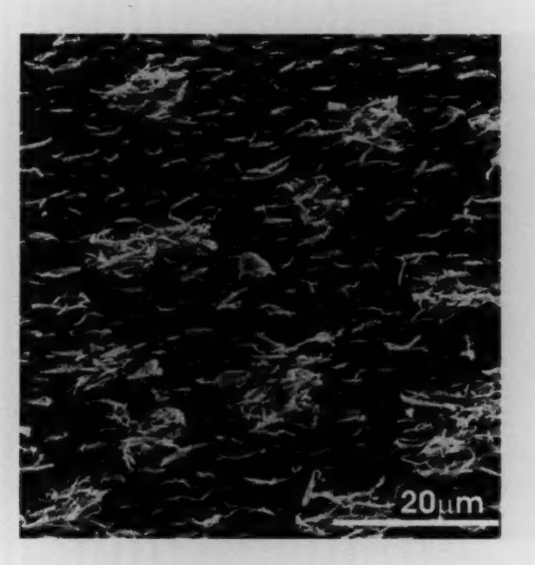

Figure 4.10. Identical to figure 4.9b, but at higher magnification.

nebulizers tested, the addition of superparamagnetic magnetite particles to the suspension did not significantly alter the nebulization efficiency or run time. For the CA suspensions, the nebulization efficiency was 43.3 ± 13.4 %, and the run time was 7.39 ± 0.58 minutes, while for the CA/magnetite suspensions, the nebulization efficiency was 40.5 ± 15.2 %, and the run time was 7.07 ± 0.56 minutes. With reference to table 4.2, it appears that the large standard deviation between runs was due to variation between nebulizers, with nebulizer C considerably less efficient than A or B, as opposed to experimental error.

4.3.4. Particle Size and Concentration

Lognormal length and diameter distributions, and particle number concentrations, were determined for both the CA and CA/magnetite aerosols from SEM images of three samples taken from different locations on the sampling membranes. As an example, figure 4.11 shows one SEM image of CA particles used in the size analysis, and figure 4.12 shows the same image after all particles were counted and marked. Particles with no

TABLE 4.2. Nebulization Efficiencies and Run Times for Cromoglycic Acid Suspensions with and without Magnetite

	Cromoglycic Acid		Cromoglycic Acid with Magnetite	
Nebulizer	Efficiency (%)	Time (min.)	Efficiency (%)	Time (min.)
A	49.3	6.95	49.4	6.87
B	52.6	7.17	49.2	6.63
C	27.9	8.05	23.0	7.70
Average	43.3 ± 13.4	7.39 ± 0.58	40.5 ± 15.2	7.07 ± 0.56

Average values expressed as mean ± one standard deviation, n = 3.

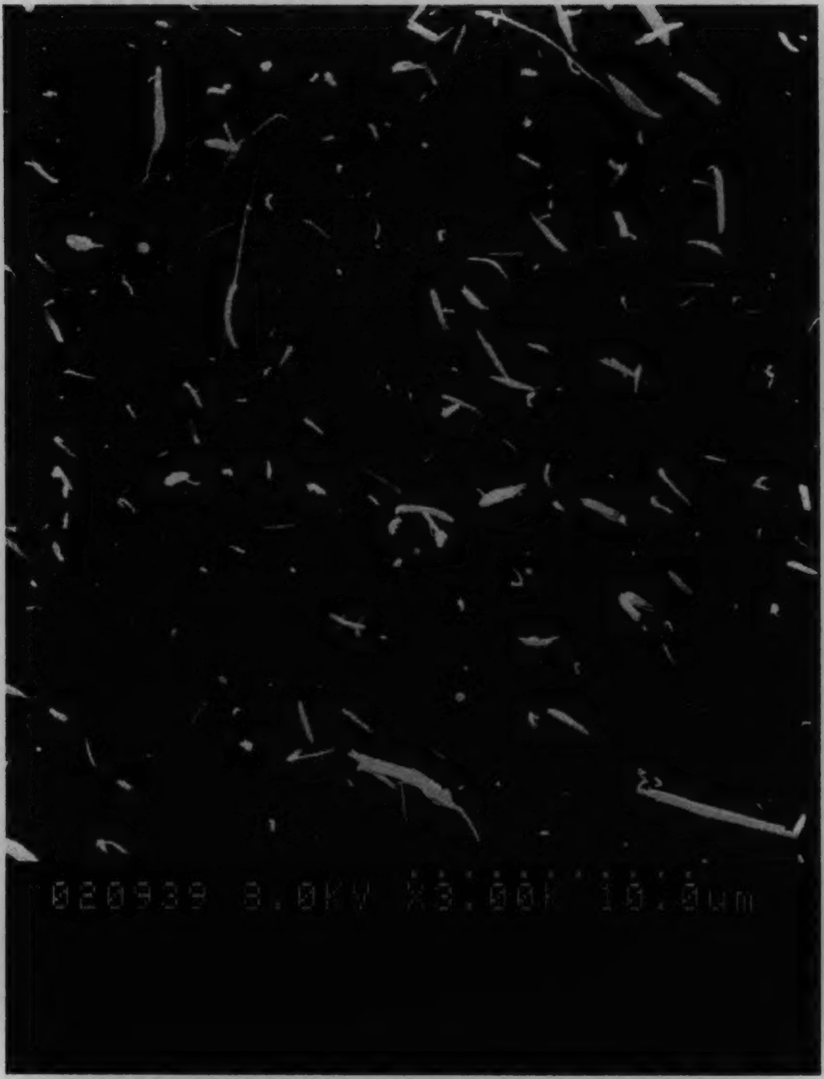
020939 3.0KV X3.00K 10.0um

Figure 4.11. An SEM image of CA particles used in determining length and diameter distributions.

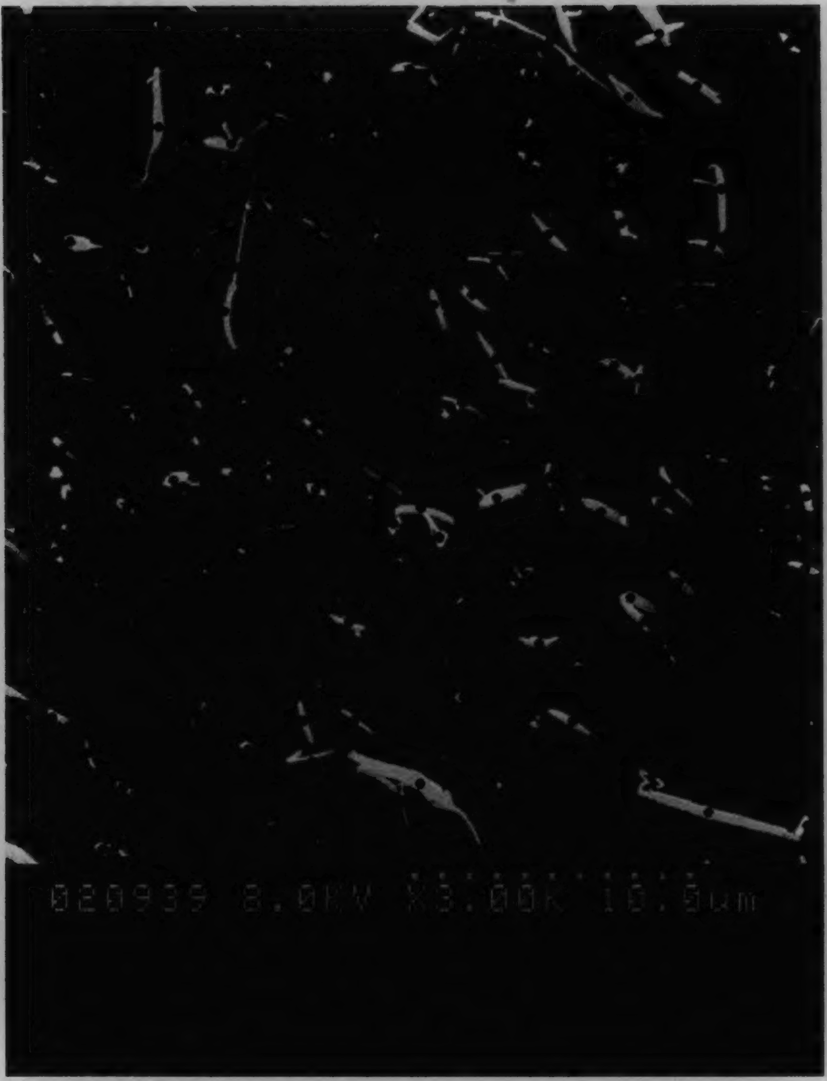
020939 8.0KV X3.00K 10.0um

Figure 4.12. Identical to figure 4.11, but with all sized particles marked with a black dot.

dimension larger than 150 nm were ignored, as these particles were estimated to contribute much less than 1% of the total aerosol volume. In total, over all images, 1773 CA particles, and 2267 CA/magnetite particles were sized.

In order to evaluate any variation in the sizes and concentration of collected aerosol across the membrane, one-way ANOVA for independent samples was used to compare the VMD, VML, σ_L, σ_D, and number concentration (N) across the three membrane samples for each formulation. For CA, no statistically significant differences were found between membrane samples for any of these parameters ($P > 0.05$). For the CA/magnetite, statistically significant ($P < 0.05$) differences in VMD and σ_D were found between two of the samples, and in N between one sample and the other two, while there were no significant differences between samples for the length distribution parameters. VMD ranged from 0.43 ± 0.04 μm to 0.52 ± 0.02 μm between samples, while σ_D ranged from 1.47 ± 0.08 to 1.68 ± 0.02 and N ranged from 22480 ± 1390 cm^{-3} to 29919 ± 2834 cm^{-3}. As these differences, though statistically significant, are reasonably small, for both formulations the mean and standard deviation of each parameter was calculated over values from all nine SEM images taken from the three different membrane samples. These are reported in table 4.3.

In addition, figure 4.13 displays cumulative, normalized volume distributions in both diameter and length for the CA and CA/magnetite aerosols. These distributions were compiled from all measured particles for either aerosol, and are approximated by the

TABLE 4.3. Lognormal Particle Size Distributions and Number Concentrations for Cromoglycic Acid and Magnetite-Loaded Cromoglycic Acid Aerosols

	CA/magnetite	*CA*
VMD [μm]	0.47 ± 0.05	0.34 ± 0.02
σ_D	1.6 ± 0.1	1.5 ± 0.1
VML [μm]	3.0 ± 0.5	2.0 ± 0.4
σ_L	2.1 ± 0.2	2.1 ± 0.1
N [cm^{-3}]	$(2.5 \pm 0.4) \times 10^4$	$(2.0 \pm 0.3) \times 10^4$

Values are expressed as mean ± one standard deviation, n = 9.

VMD, VML are the volume median diameter and length, respectively.

σ_D and σ_L are the geometric standard deviations for diameter and length, respectively.

N is the number of particles per unit volume of sampled air.

lognormal distributions given in table 4.3. Finally, figure 4.14 displays plots of particle length versus diameter for the CA and CA/magnetite aerosols. These plots provide an indication of the correlation between measured particle lengths and diameters.

4.3.5 Small Airway Deposition

The magnetic field generated between the two permanent magnets was measured in the central plane between the two magnets, over the region of space containing the airways. This space constituted a 2 cm by 2 cm square centered at the central point between the magnets. Figure 4.15 displays the measured magnetic flux densities produced across the airways. At the center of this region, the measured flux density was approximately 50 mT. The gradient in the flux density fell from ~1 T/m at the edges of the region of interest to 0 T/m at the center.

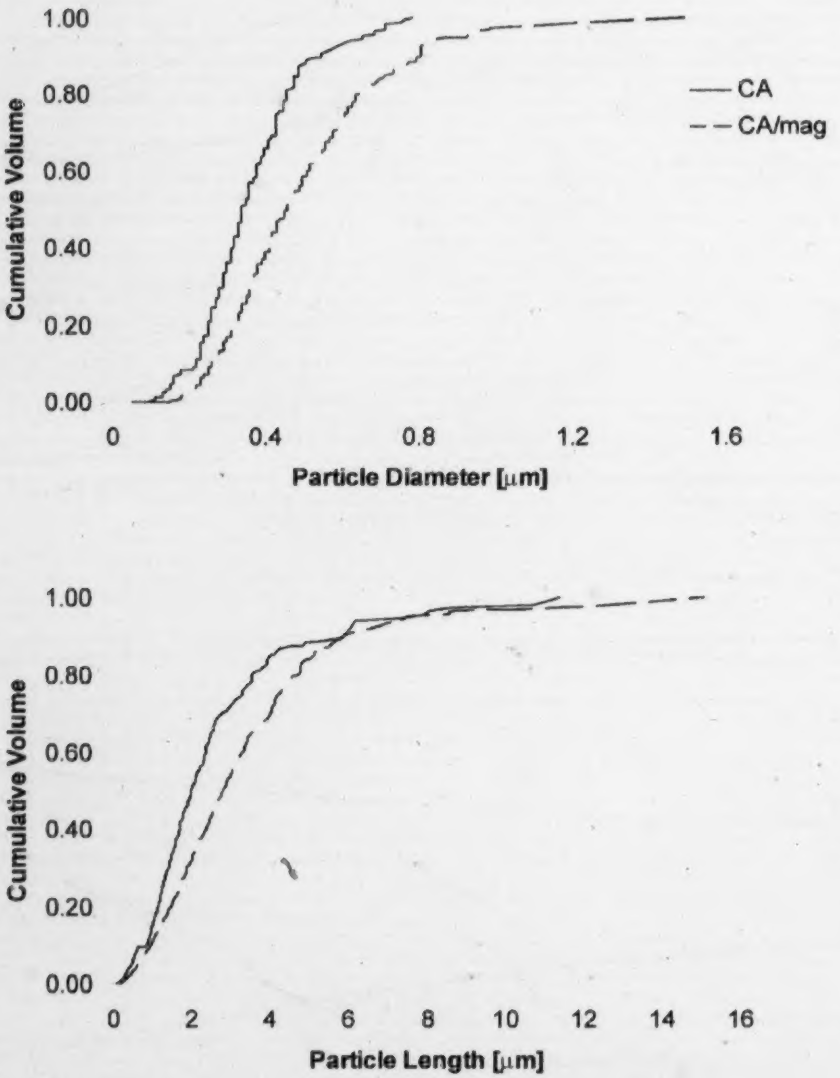

Figure 4.13. Cumulative, normalized volume distributions in diameter and length for CA and CA/magnetite aerosols.

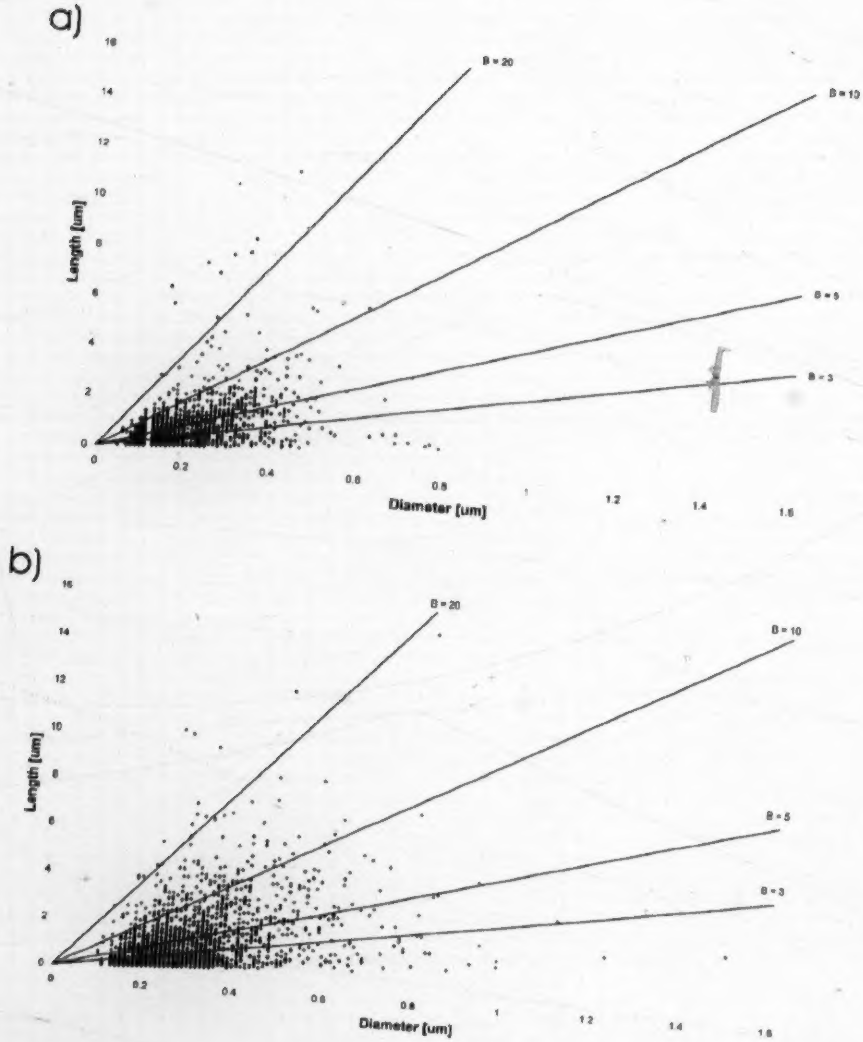

Figure 4.14. Particle length versus diameter for (a) CA aerosol, and (b) CA/magnetite aerosol. The solid lines indicate values of the particle aspect ratio, B.

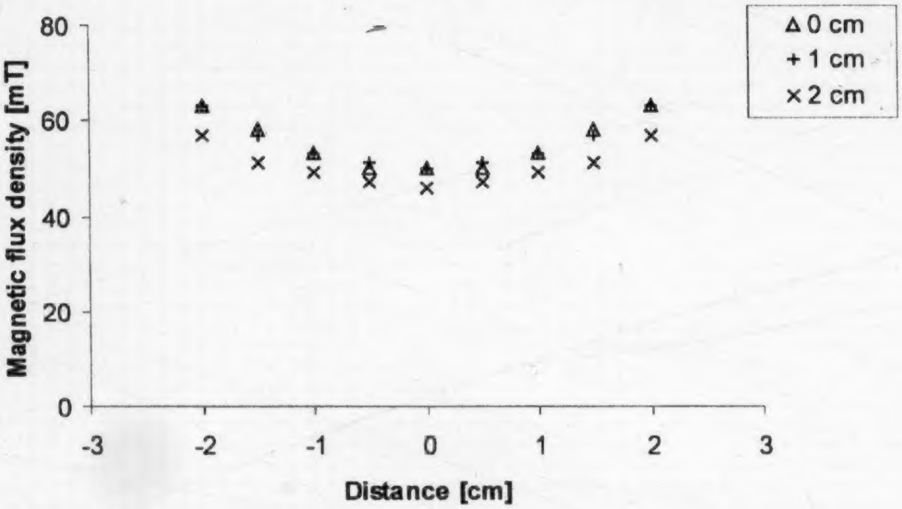

Figure 4.15. The measured magnetic flux density over the region of space containing airways. Measurements were made along the centerline between the two magnets, as well as 1 cm and 2 cm off of the centerline.

The aerosol deposition efficiency in the airway array was calculated as the mass of CA recovered from the array as a percentage of the total mass of CA recovered from the array, the holder, and the downstream filter. The total recovered mass of CA averaged over all experiments was 1.5 ± 0.3 mg (n = 9). There was no significant difference in the total mass recovered between experiments performed for CA, and for CA/magnetite with and without the magnetic field (one way ANOVA, standard weighted means analysis for independent samples; $F = 0.57$).

The deposition efficiencies for the three cases studied are shown in figure 4.16. The deposition efficiency for CA was 0.9 ± 0.2 %, while for CA/magnetite it was 1.9 ± 0.5% with no magnetic field, and increased to 3.3 ± 0.4% with the magnetic field positioned across the array. Employing one way ANOVA, with standard weighted means analysis for independent samples, and the Tukey HSD test, the difference between deposition efficiencies for CA and for CA/magnetite with no magnetic field is not significant ($P > 0.05$), whereas the increased deposition efficiency observed for CA/magnetite in the presence of the external magnetic field is statistically significant ($P < 0.01$).

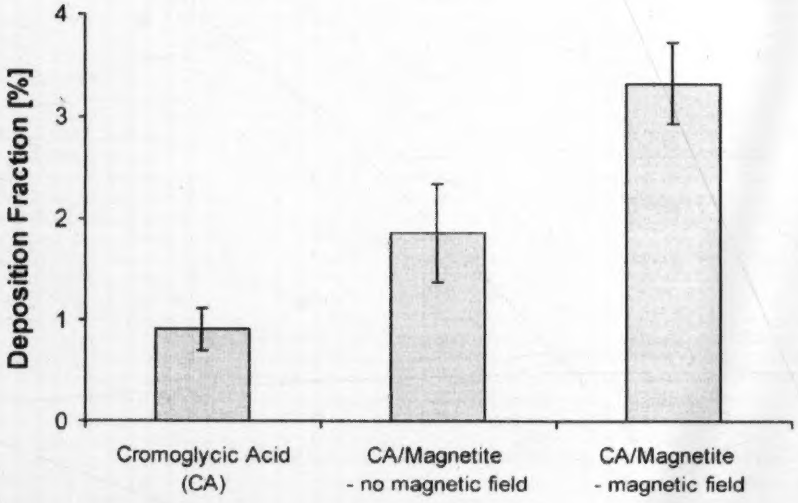

Figure 4.16. Deposition efficiency in the small airway model for cromoglycic acid (CA) aerosol, and for magnetite-loaded CA with and without the magnetic field. Error bars represent one standard deviation (n = 3).

4.4. Discussion

In the present work, it was demonstrated that deposition of magnetite-loaded, high aspect ratio drug particles in small, bifurcating airways can be increased by producing a magnetic field across those airways. Airway dimensions were chosen to be on the same order as those of the terminal bronchioles in the human lung. This region of the lung was modeled because the airway diameters are sufficiently small that interception plays a major role in determining the deposition of particles a few micrometers and longer in length. While airway diameters are smaller still in more peripheral, gas-exchange regions of the lungs, these airways are heavily lined with alveoli, and undergo significant expansion and contraction over a breathing cycle, making the design of an anatomically accurate physical model more difficult. Furthermore, as predicted by the analytical deposition model described in chapter 3, particle residence times in the last few generations of the alveolar region become sufficiently great that deposition due to sedimentation may overshadow the effects of interception on the total airway deposition.

The addition of approximately 15% w/w magnetite to 2 mg/ml suspensions of CA had no impact on the nebulization efficiency of CA from Hudson Updraft II jet nebulizers. However, the VMD and VML of the aerosol sampled from the delivery chamber were both larger for the combined CA/magnetite formulation than for CA alone. This increase in particle size may be due to increased aggregation of suspended CA particles in the presence of colloidal magnetite, and is consistent with the increased deposition efficiency of CA/magnetite in the airway array compared to CA alone, though it must be noted that the latter increase was not statistically significant. Also, while CA particles with lengths up to approximately 30 μm were found exiting the nebulizer, as seen in figure 4.6, particles of comparable length were not collected from the delivery chamber in the aerosol sizing procedure. This suggests that longer particles were lost in the delivery apparatus, and highlights the importance of keeping all experimental parameters, especially the flow rates through the delivery chamber, identical whether sampling onto polycarbonate membranes, or drawing aerosol through the airway array, at the base of the chamber.

Given that airway deposition of high aspect ratio particles was measured in the present work in smaller diameter airways, representative of more distal lung generations, than have previously been studied in physical models, it makes sense to compare the measured results with predictions made by the analytical model described in chapter 3, with a slight modification to include deposition due to diffusion in the parent airways. The measured deposition fractions were of the mass of CA depositing in the airways compared to the total mass of CA entering the airways. As such, a quantitative comparison with the analytical model can only be made for the CA aerosol. For the CA/magnetite aerosol, the deposition fraction cannot be predicted because the fraction of CA in each sized particle is unknown, and is not expected to be constant given the rather arbitrary manner in which CA/magnetite particles were prepared. For example, two nebulized droplets of the same size, containing the same amount of colloidal magnetite but different sizes of CA crystals would dry to form composite particles with different mass fractions of CA.

At any rate, for the CA aerosol, the fraction of aerosol mass deposing in the airways was predicted from the probability of deposition for each sized particle, weighted by the normalized mass of that particle compared to the total mass of all sized particles. Particles were assumed to be aligned parallel with the direction of flow through the airways. The analytical deposition model predicted a deposition fraction of 0.66 %, compared with the measured value of 0.9 ± 0.2 %. Given the approximations made in developing the model, as well as in sizing the particles, this is considered to be quite a good agreement.

Deposition of CA/magnetite aerosols in the airway array increased by a factor of 1.74 (by mass) with the magnetic field aligned perpendicular to the parent airways, as compared to deposition with no magnetic field. Such an outcome demonstrates the feasibility of magnetic alignment of high aspect ratio particles as a means to achieve localized targeting of inhaled aerosols in the small airways. In order to improve upon this initial result, that is, to achieve a larger increase in deposition in future work, a first question to be addressed is the extent to which particles were aligned with the magnetic field. Very good magnetic field alignment was observed when CA/magnetite particles were collected onto the 5 μm pore size polycarbonate membranes, in that a strong majority of particles viewed by SEM imaging were oriented parallel to the direction of magnetic field lines. However, as described in detail in chapter 2, during transit through airways, high aspect ratio particles will be subject to a torque arising from shear in the entraining airflow that tends to align them with their long axes parallel to their direction of motion, and, in the present small airway experiments, perpendicular to the direction of magnetic field lines.

Pertinent, then, in determining particle orientations is the ratio between the aerodynamic torque and the magnetic torque that tends to align the particles parallel to magnetic field lines. This ratio was examined in chapter 2, section 2.7, and it was concluded that for typical flow rates through the small airways of the lung, and for even quite sparse deposits of magnetite on particle surfaces, the estimated magnetic torque is at least an order of magnitude greater than the aerodynamic torque. As such, in the present experiments, the CA/magnetite particles are very likely to be aligned with the magnetic field, so that neither an increase to the magnetic field strength, nor to the concentration of magnetite in suspension (both of which could increase the magnetic torque exerted on particles) is expected to improve upon the measured increase in deposition. Instead, optimization of particle morphology is likely to be the avenue through which deposition in targeted areas is further increased. As predicted by the analytical model described in chapter 3, longer particles of similar diameter would deposit more readily by interception when aligned with magnetic fields, whereas their deposition by impaction or sedimentation would change very little, owing to the weak dependence of aerodynamic diameter on the length of high aspect ratio particles.

Unlike previously proposed techniques for magnetically targeted drug delivery dating back three decades (Widder et al., 1978; Senyei et al., 1978; Mosbach and Schröder, 1979), the present technique does not rely on a magnetic force on particles, but rather on a magnetic torque. Accordingly, no gradient in the magnetic field is required to target particles, eliminating an obstacle typically associated with techniques that rely on a magnetic force (Dobson, 2006). In the present work the magnetic field was relatively constant across the airway array, with the field gradient decreasing from ~ 1 T/m at the edges of the airway array down to 0 T/m at its center. The translational magnetic force exerted on the CA/magnetite particles can be estimated by simplifying equation (2.36) in section 2.6, under the assumption that the field gradient and particle magnetization can be considered constant over the volume of the particle, and taking the component of the field gradient in the same direction as the magnetization (which for aligned particles will be in the direction of the magnetic field). This yields

$$\vec{F}_m = V_m M \mu_0 \nabla H \hat{\mathbf{M}} \tag{4.1}$$

where V_m is the volume of magnetite in the particle, M is the magnetization of magnetite, H is the magnetic field strength, μ_0 is the permeability of free space, and $\hat{\mathbf{M}}$ is a unit vector pointing in the direction of the particle magnetization.

In order to evaluate the effect of the magnetic force given in equation (4.1) on particle trajectories, the particle equation of motion can be nondimensionalized and the resulting coefficients of different terms can be compared. This approach is in direct analogy to the treatment of the electrostatic force acting on charged particles presented by Finlay (2001). In the present case, the particle equation of motion is

$$m\frac{\mathrm{d}\vec{v}}{\mathrm{d}t} = m\vec{g} - 3\pi d_{ae}\mu\left(\vec{v} - \vec{v}_f\right) + M\mu_0 \nabla H \frac{m\phi_m}{\rho_m}\hat{\mathbf{M}} \tag{4.2}$$

where m is the mass of the composite particle, v is the particle velocity, v_f is the fluid velocity, d_{ae} is an equivalent spherical aerodynamic diameter for the particle, μ is the fluid viscosity, ρ_m is the density of magnetite, and ϕ_m is the mass fraction of magnetite in the particle.

Equation (4.2) can be written in nondimensional form as

$$\frac{U^2}{D}\frac{\mathrm{d}\vec{v}'}{\mathrm{d}t'} = g\hat{\mathbf{g}} - \frac{3\pi d_{ae}\mu U}{m}\left(\vec{v}' - \vec{v}'_f\right) + M\mu_0 \nabla H \frac{\phi_m}{\rho_m}\hat{\mathbf{M}} \tag{4.3}$$

where U is the average velocity of air through an airway, and D is the airway diameter.

Dividing equation (4.3) through by the coefficient of the dimensionless drag force then gives

$$Stk\,\frac{\mathrm{d}\vec{v}'}{\mathrm{d}t'} = \frac{v_s}{U}\hat{\mathbf{g}} - \left(\vec{v}' - \vec{v}'_f\right) + Mag\hat{\mathbf{M}} \tag{4.4}$$

where the Stokes number, *Stk*, and settling velocity, v_s, are defined for high aspect ratio particles, and the symbol *Mag* is introduced for the coefficient of the dimensionless magnetic force.

The following two ratios can then be defined

$$\frac{Mag}{Stk} = \frac{M\mu_0 \nabla H \phi_m D}{\rho_m U^2} \tag{4.5}$$

and

$$\frac{Mag}{\left(v_s/U\right)} = \frac{M\mu_0 \nabla H \phi_m}{\rho_m g} \tag{4.6}$$

The ratios in equations (4.5) and (4.6) can be used to estimate the relative influence of the translational magnetic force, compared to particle inertia and the force of gravity, on the trajectories of CA/magnetite particles in transit through the airway array. These ratios are calculated at present assuming a mass fraction of magnetite of 0.15 and a density of magnetite of 5000 kg/m^3. An empirical relationship between magnetization and magnetic field strength for magnetite nanoparticles prepared in an identical manner to that employed in the present thesis was determined by Cheng *et al.* (2005). At field strengths between 50 and 60 mT, such as those produced across the airways of the array, the magnetization has a value of approximately 175 kA/m. Using this magnetization, along with a representative field gradient of 0.5 T/m, an average air velocity through parent airways of 12.8 cm/s, and an airway diameter of 0.5 mm, $Mag/Stk = 0.08$ and $Mag/(v_s/U) = 0.26$. This means that, in the small airway experiments, the effect of the translational magnetic force on particle trajectories was small compared with that of gravity, and very small compared with that of particle inertia. As such, the magnetic force could not have been responsible for the 74% increase in deposition of CA/magnetite aerosols in the presence of the magnetic field, and this deposition can instead be primarily attributed to the effect of magnetic alignment on interception.

As is clear through equations (4.5) and (4.6), increasing the field gradient to larger values would likely result in a greater increase to deposition in the airway array, due to drift of particles towards airway walls resulting from a magnetic force; however, it is uncertain whether such a result could translate to clinical applications in humans because high field gradients are difficult to generate at sufficient depth below the surface of the skin (Dobson, 2006). Recent *in vivo* work in mice by Dames et al. (2007) highlights this issue. These researchers employed a specifically designed electromagnet to generate a field gradient of >100 T/m near the magnet's tip that decreased in magnitude with distance from the tip. With the tip placed 1 mm above the right lung lobes of the mice, deposition of nebulized suspensions containing 12.5 mg/ml magnetite nanoparticles in water was increased on average by 8x in that lobe compared to the left lobe; however, moving the magnet away from the targeted tissue by only a few millimeters reduced the deposition in the targeted lobe to 2.5x that in the non-targeted lobe. Justifiably, these researchers concluded that scale up of their targeting system to a size appropriate for use in humans will be a major challenge (Dames *et al.*, 2007). The approach to magnetic targeting described in this thesis, by aligning high aspect ratio particles, eliminates this difficulty because no field gradient is required.

In conclusion, it has been demonstrated that aerosol deposition of magnetite-loaded, high aspect ratio drug particles in small, bifurcating airways is increased in the presence of a magnetic field. Unlike previous approaches to magnetic drug targeting, no gradient in the magnetic field strength is required to increase deposition by interception through magnetic alignment. This phenomenon shows promise for targeting aerosol drug delivery to specific locations within the lungs, especially if particle diameters and lengths can be optimized based on the theoretical analysis presented in chapter 3.

5. DRY POWDERS CONTAINING HIGH ASPECT RATIO PARTICLES

5.1. Introduction

In the previous chapter, high aspect ratio drug particles were loaded with magnetite nanoparticles by nebulizing suspensions containing both particle types, and then allowing water to evaporate from the nebulized droplets to leave behind dry, composite aerosol particles. Drying of the nebulizer droplets was reasonably straightforward in these experiments because the residence times of the aerosol particles in the delivery chamber, prior to being drawn through the small airway array, were on the order of minutes, whereas micrometer-sized water droplets completely evaporate in at most, for very humid air, a few seconds, provided they don't saturate the entraining air (Willeke and Baron, 1993). However, such a large volume delivery chamber (~16 l) would be impractical for aerosol delivery to patients; instead, the nebulizer output would likely have to be passed though drying tubes containing desiccant, such as silica gel, surrounding the flow path in order to dry the droplets prior to delivery to patients. In addition, the potential for flocculation of high aspect ratio drug particles in suspension, prior to nebulization, limits the concentration of drug that can be nebulized, and therefore will place a limit on the rate of drug delivery to patients.

Given such concerns with nebulization and drying of high aspect ratio particles, it is sensible at this early stage to also consider alternative delivery systems. Dry powder formulations containing elongated, nonspherical particles have previously been explored in a limited number of studies. Zeng *et al.* (2000) prepared several formulations containing carrier lactose particles and micronized, compact salbutamol sulphate in a ratio of 67.5 to 1, by mass. The average aspect ratio of the lactose carriers ranged from 1.3 to 2.1, and the fine particle fraction (defined in this study as the fraction of drug contained in aerosol particles with aerodynamic diameter < 6.4 μm) of salbutamol sulphate from two commercial dry powder inhalers increased with the aspect ratio of the lactose. In a subsequent study conducted by the same research group, Larhrib *et al.* (2003) again prepared formulations containing 67.5 parts lactose to 1 part salbutamol sulphate, by mass, but these formulations were prepared with average lactose aspect ratios of 1.7, 2.0, and 6.3, and with both micronized and needle-like salbutamol sulphate particles. The fine particle fraction of salbutamol sulphate from commercial inhalers again increased with the aspect ratio of the carrier, and was also found to be higher for formulations containing needle-like salbutamol sulphate than for identical formulations containing the micronized, compact salbutamol sulphate. In contrast, the fraction of salbutamol sulphate emitted from the inhalers (that is, the fraction of the nominal dose originally loaded into the inhalers that was emitted) decreased with the carrier aspect ratio, and was lower for needle-like than for micronized salbutamol sulphate. The authors concluded that the powders containing elongated carrier and/or drug particles exhibited poorer dispersion than those containing compact particles, but that this was more than compensated by the lower aerodynamic diameters of the elongated particles compared to mass equivalent compact particles, leading overall to higher fine particle fractions (Larhrib *et al.*, 2003). The suggestion that powders containing elongated particles will exhibit poor dispersion was echoed by Crowder *et al.* (2002), who attributed the effect to large attractive forces between elongated particles in contact along their lengths.

In another study, Ikegami *et al.* (2002) measured fine particle fractions of plate-like and needle-like crystals of the steroid KSR-592 blended with lactose carriers in ratios of 19 to 1, carrier to drug. The fine particle fraction of KSR-592 emitted from commercial dry powder inhalers was found to be much larger for powders containing the needle-like crystals than those containing the plate-like crystals. In contrast to the conclusions of Larhrib *et al.* (2003), Ikegami *et al.* (2002) wrote that unstable contact points between elongated particles lead to relatively easy fluidization and deaggregation. In truth, as depicted schematically in figure 5.1, it is possible to imagine different packing arrangements of elongated particles that would be expected to be more or less easy to

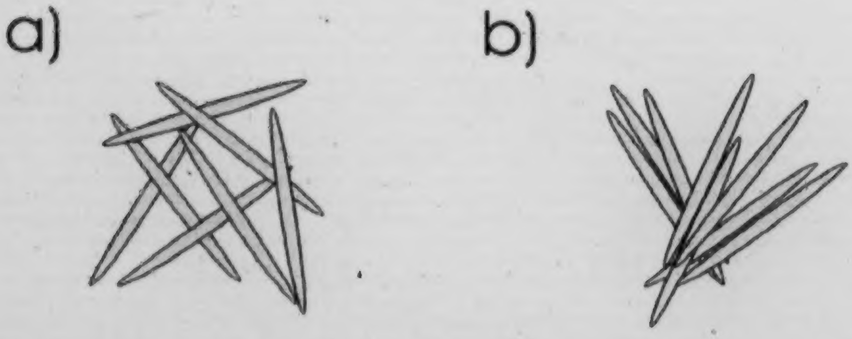

Figure 5.1. Schematic of elongated particles with packing arrangements expected to be relatively easy (a), or difficult (b), to disperse.

disperse. Whereas high void fractions coincide with random particle orientations, very low void fractions may exist when particles stack along their lengths (Dullien, 1997). While the packing arrangements of nonspherical particles are difficult to predict (Dullien, 1997), it is expected that, with all particle properties held constant, powders with lower bulk density will have larger void fractions, and be easier to disperse. Therefore, methods to reduce the density of powders containing high aspect ratio particles may improve their dispersion.

In the work described in this chapter, the dispersion and mouth-throat deposition of powders containing high aspect ratio particles of cromoglycic acid, ciprofloxacin base, and paclitaxel were explored using a commercial dry powder inhaler and idealized model of the mouth and throat airways. Powders were evaluated with and without addition of magnetite nanoparticles, and before and after undergoing lyophilization in order to reduce their bulk densities.

5.2. Experimental Methods

5.2.1. Materials

Cromolyn sodium salt was purchased from Sigma-Aldrich Canada (Oakville, ON). Cromoglycic acid was prepared by crystallization as described in chapter 4. Cromoglycic acid was mixed with lactose (Respitose ML006; DMV Int., Veghel, Netherlands) to form powders. As reported by the manufacturer, the lactose had a median volume diameter of 17 μm, with 90% of the total volume contained in particles under 45 μm. Ciprofloxacin base (Sigma-Aldrich Canada, Oakville, ON) and paclitaxel (Ampac Fine Chemicals, Rancho Cordova, CA) powders containing acicular, micrometer sized crystals were purchased. Magnetite nanoparticles were prepared by precipitation as described in chapter 4.

5.2.2. Cromoglycic Acid/Lactose Powders

After precipitation of high aspect ratio cromoglycic acid (CA) crystals, the resulting suspension was filtered and dried to form a cake of packed crystals. In order to form a powder suitable for aerosol delivery to the lung, this dried CA was ground using a mortar and pestle, and then mixed with lactose in a ratio of 1 to 3, drug to lactose. Next, both the drug and lactose were placed in a 2 ml vial, and blended by agitating for two hours using a wrist-activated shaker (Thermolyne Maxi Mix II; Fisher Scientific Canada, Ottawa, ON) with vibrations set to 80% full scale. This process was repeated for CA with 15 % (w/w) magnetite nanoparticles added prior to crystallization.

5.2.3. Ciprofloxacin and Paclitaxel Powders

As purchased, powders of ciprofloxacin base and paclitaxel contained micrometer scale, needle-like drug crystals. These crystals were suspended in deionized water at a concentration of 10 mg/ml, with and without the addition of 0.9 mg/ml magnetite. The suspensions were placed in baths of liquid nitrogen and stirred until frozen, then lyophilized for 24 hours (FreeZone 4.5, Model 77500; Labconco, Kansas City, MO) until dry. Due to the small batches of powders produced, bulk powder densities were measured before and after lyophilization by placing small powder samples of known mass in graduated, 1.5 ml centrifuge tubes, and tapping the tubes on a bench top until a minimum volume was achieved (that is, until further taps did not decrease the powder volume any more).

5.2.4. *In Vitro* Lung Deposition from a Dry Powder Inhaler

Portions of the powders, with and without added magnetite, were loaded into hard gelatin capsules (size 3; Torpac Inc., Fairfield, NJ), and dispersed using an Aerolizer dry powder inhaler (purchased with Foradil; Novartis Pharma Canada, Dorval, QC) through an idealized adult mouth-throat geometry (Stapleton *et al.*, 2000) at a steady flow rate of 60 l/min, maintained by vacuum pump, for 4 seconds. The interior walls of the mouth-throat geometry were coated with a layer of grease (316 Silicone Release Spray; Dow Corning Corp., Midland, MI) to avoid particle bounce and resuspension. Absolute filters (Respirgard; Vital Signs, Inc., Totowa, NJ) were placed downstream from the mouth-throat in order to collect particles penetrating the geometry. The amounts of drug reaching these filters were deemed the *in vitro* lung doses. For the CA powders, the masses of drug depositing in the mouth-throat and reaching the filter were determined by washing with 0.01 N sodium hydroxide, converting CA to its soluble sodium salt, and subsequent UV spectrophotometry (8452A; Hewlett-Packard, Palo Alto, CA). For ciprofloxacin powders, the mouth-throat and filter were washed with 0.01 N hydrochloric acid, and the concentrations of ciprofloxacin hydrochloride in these washings were determined by UV spectrophotometry. As a comparison, the total aerosol mass delivered to the filter was also measured by gravimetric analysis, weighing each filter before and after every experimental run. For paclitaxel powders, as no straightforward chemical assay was available, the masses of aerosol reaching the filters were measured only by weighing. The experiment was repeated in triplicate for each powder studied. As reported by previous researchers (Nielsen *et al.*, 1997), on occasion the Aerolizer device failed to properly pierce the capsule, or the capsule became stuck in its chamber and was not free to rotate. These experimental runs were discarded, and replaced with additional repetitions.

To compare with the measured *in vitro* lung dose, the aerodynamic size distribution of the as-supplied ciprofloxacin powder was measured in triplicate using an eight-stage cascade impactor (Mark II Andersen Impactor; Thermo Andersen, Smyrna, GA), operated at 60 l/min. for 4 seconds, with a pre-separator placed between the Aerolizer inhaler and the impactor stages to filter out very large particles or particle aggregates. Cut-points for the stages of the Andersen impactor operating at 60 l/min. were taken from Nichols (1998). For each run, the mass of ciprofloxacin depositing on each stage of the impactor, and in the pre-separator and inlet, was determined by washing with 0.01 N hydrochloric acid and subsequent UV spectrophotometry. In addition, for one run, the mass of ciprofloxacin lost between stages in the cascade impactor jets was determined by the same chemical assay.

Finally, in order to qualitatively examine whether ciprofloxacin particles lyophilized together with magnetite nanoparticles were responsive to magnetic fields, these powders were dispersed using the Aerolizer, through the mouth-throat geometry, at 60 l/min. for 4 seconds, into a 4 l chamber, and then drawn at 0.21 l/min from the chamber through a 0.2 μm pore size polycarbonate membrane, with a magnetic field of ~50 mT generated parallel to the face of the membrane using permanent magnets, as described in chapter 4. Samples of the membrane were analyzed by SEM to observe whether or not the ciprofloxacin particles aligned with the magnetic field.

5.3. Results

5.3.1. Cromoglycic Acid/Lactose Powders

The mass of powder loaded into each capsule was 26± 2 mg for the CA/lactose powder, and 24 ± 2 mg for the CA/lactose/magnetite powder (mean ± one standard deviation, n = 3). This corresponded to a nominal drug mass in the capsule of 6.4 ± 0.6 mg and 5.5 ± 0.4 mg for the two powders, respectively. Figure 5.2 shows the percentages of the nominal drug mass emitted from the dry powder inhaler, depositing in the mouth-throat, and reaching the filter for CA/lactose powders with and without magnetite. These percentages were compared between the two powders using a two-tailed student's *t*-test for independent samples. Only the difference in the percentage of CA delivered to the filter, that is, the *in vitro* lung dose, was statistically significant ($P < 0.05$). The *in vitro* lung dose decreased from 23 ± 5% of the nominal dose for the CA/lactose powder, to 12 ± 1% for the CA/lactose/magnetite powder.

The total mass of aerosol delivered to the filters was determined by gravimetric analysis. This mass was considerably higher than the mass of CA recovered from the filters by chemical assay, suggesting that significant amounts of lactose also reached the filters. In fact, the mass of CA expressed as a percentage of the total mass of aerosol on the filters was 38 ± 14% for CA/lactose, and 28 ± 3% for the CA/lactose/magnetite powders.

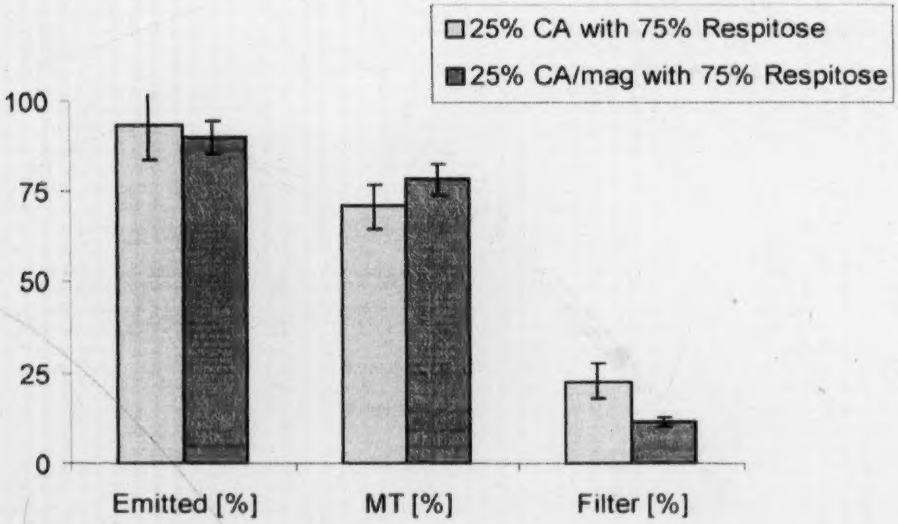

Figure 5.2. The percentages of the nominal (capsule) dose of cromoglycic acid (CA) emitted from the Aerolizer inhaler, depositing in the mouth-throat geometry, and reaching a filter downstream from the mouth-throat. Results are displayed for CA/lactose (Respitose) formulations with and without added magnetite nanoparticles. Error bars represent one standard deviations around the mean values (n = 3).

5.3.2. Ciprofloxacin and Paclitaxel Powders

For each powder studied, table 5.1 displays the measured tap densities, capsule loadings, and percentages of drug emitted from the inhaler, depositing in the mouth-throat, and reaching the filter (the *in vitro* lung dose). For the two lyophilized paclitaxel powders, and the lyophilized ciprofloxacin powder, with no magnetite, the reported capsule loads approached the maximum loads that could be placed in the capsules without compressing

TABLE 5.1. Densities, Capsule Loadings, and Emitted, Mouth-Throat, and Lung Doses for Ciprofloxacin and Paclitaxel Powders

Powder	Bulk Tap Density [g/cm3]	Capsule Load [mg]	Emitted Dose [% nominal]	Mouth-Throat [% nominal]	Lung Dose [% nominal]
Cipro	0.29 ± 0.01	8.7 ± 0.4	66 ± 7	49 ± 9	16 ± 3
Cipro FD	0.062 ± 0.008	4.7 ± 1.0	80 ± 12	58 ± 9	22 ± 3
Cipro/Mag FD	0.14 ± 0.01	9.8 ± 1.9	73 ± 2	55 ± 1	19 ± 1
Cipro	0.29 ± 0.01	25 ± 2	71 ± 3	52 ± 3	19 ± 2
Cipro/Mag FD	0.14 ± 0.01	18 ± 1	71 ± 5	48 ± 4	23 ± 2
Taxol	0.20 ± 0.02	9.9 ± 0.3	–	–	32 ± 7
Taxol FD	0.079 ± 0.003	9.2 ± 0.3	–	–	50 ± 4
Taxol/Mag FD	0.112 ± 0.003	9.2 ± 0.6	–	–	53 ± 2

Cipro = ciprofloxacin; Taxol = paclitaxel; FD = freeze dried (lyophilized)

Results are expressed as mean ± one standard deviation.

Only the lung dose was measured for paclitaxel powders.

the powders. For the remaining two ciprofloxacin powders, that is, the as-supplied ciprofloxacin powder (Cipro, in table 5.1) and the lyophilized powder containing magnetite nanoparticles (Cipro/Mag FD), two capsule loadings were studied, with the higher loading being the maximum possible without compressing the powder. In general, lowering the powder density through lyophilization led to modest improvements in the emitted doses and lung doses of the ciprofloxacin powders, though these trends were not statistically significant (one-way analysis of variance for independent samples with standard weighted means analysis, and Tukey HSD test for significance; $P > 0.05$). For the paclitaxel powders, lung doses were significantly higher for the two lyophilized powders than for the as-supplied powder (one-way ANOVA for independent samples, with weighted means analysis, and Tukey HSD test; $P < 0.01$).

Lung doses for the paclitaxel powders were determined by a simple gravimetric analysis, weighing the filter before and after an experimental run. As a validation of this approach, figure 5.3 compares the mass of ciprofloxacin recovered from filters by chemical assay with that predicted by gravimetry. Results are plotted for experimental runs with powders containing only ciprofloxacin. Reasonably good agreement is seen between the two methods for the majority of data points.

Figure 5.4 compares the emitted and lung (filter) doses measured for the higher capsule loading of the as-supplied ciprofloxacin powder in the idealized mouth-throat geometry with cascade impactor measurements made for the same powder. Both tests were performed at a flow rate of 60 l/min., and duration of 4 sec. The average capsule

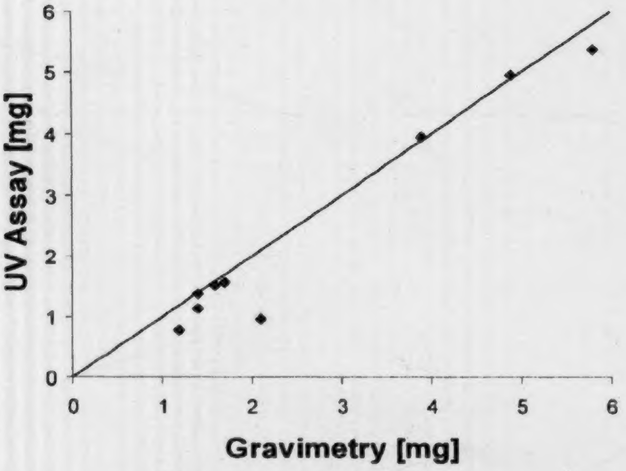

Figure 5.3. The mass of ciprofloxacin on filters measured by gravimetry is compared with measurements of the mass recovered from the same filters by UV spectrophotometry. The solid line is a line of identity.

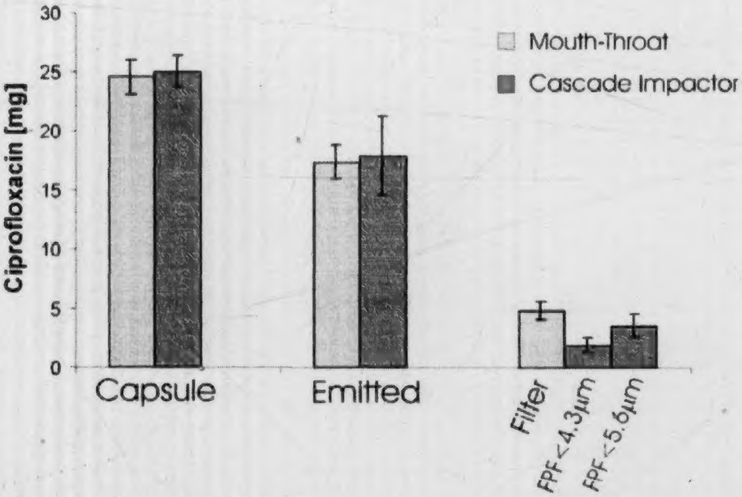

Figure 5.4. Capsule loadings, emitted doses, and estimates of the *in vitro* lung dose measured using the idealized mouth-throat geometry and an Andersen impactor are compared for the as-supplied ciprofloxacin powder.

loadings and emitted doses were nearly identical between the two tests. The *in vitro* lung dose reaching the filter was compared to fine particle fractions (FPFs) less than 4.3 μm and less than 5.6 μm. The FPF is defined here as the total mass of drug recovered from impactor stages with cut-off diameters below the stated aerodynamic diameter. The *in vitro* lung dose was significantly higher than the FPF < 4.3 μm ($P < 0.01$), but the small difference between the *in vitro* lung dose and the FPF < 5.6 μm was not statistically significant ($P > 0.05$; both comparisons made using one-way ANOVA for independent samples, with weighted means analysis, and Tukey HSD test). In the single cascade impactor run where losses in the jets between stages were measured, the total mass of ciprofloxacin recovered from the jets was 0.4 mg, compared to a total mass of 13.5 mg recovered from the cascade impactor plates, pre-separator, and inlet.

In order to gain a better sense of the size and shape of particles penetrating the idealized mouth-throat geometry and reaching the filter, additional experiments were run for the as-supplied and lyophilized ciprofloxacin and paclitaxel powders, where the filter contents were re-suspended in deionized water, and then dried on glass slides for analysis by optical microscopy. Figure 5.5 displays images of ciprofloxacin and paclitaxel particles recovered from the filters in this manner. It should be noted that, in these images, visible clusters of particles may have been present in the collected aerosol, but may also be artifacts from the preparation of slides for viewing. At any rate, it is clear that particles with lengths up to approximately 30 μm penetrated the mouth-throat geometry and reached the filter in all four cases presented in figure 5.5. Furthermore, for ciprofloxacin in particular, lyophilization seems to have broken many of the crystals

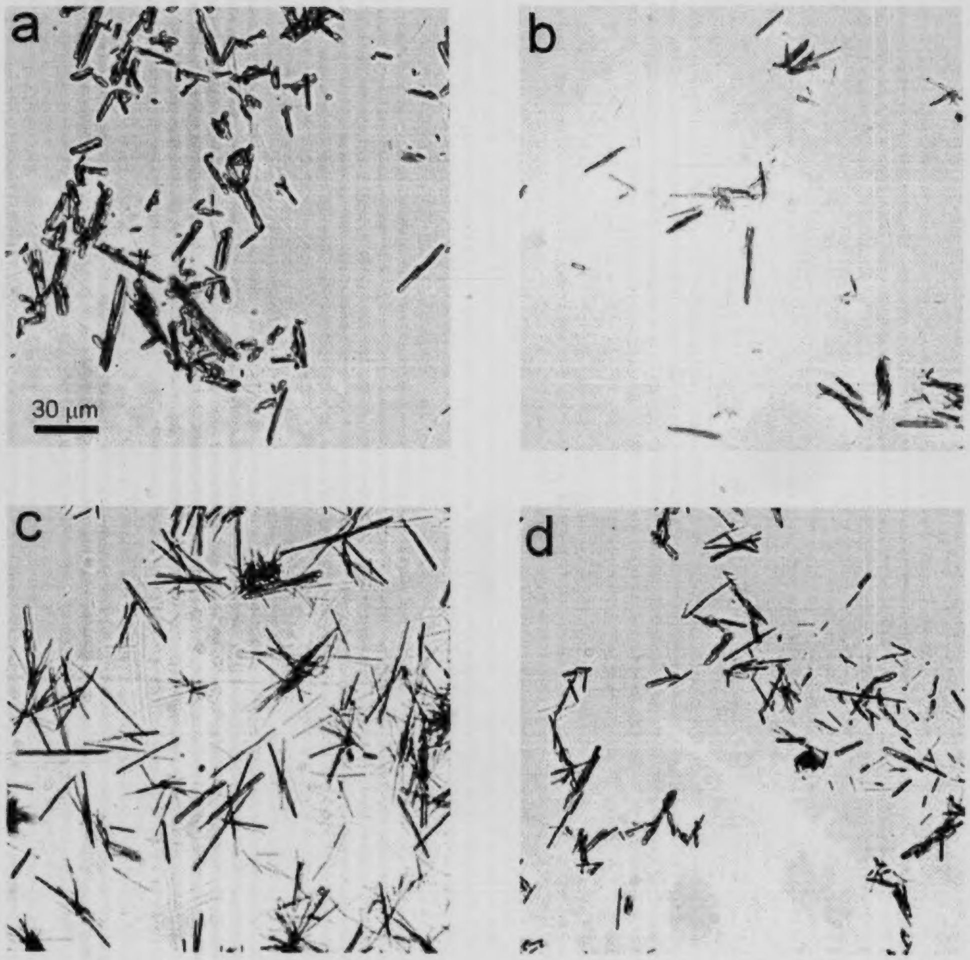

Figure 5.5. Filter samples of (a) as-supplied and (b) lyophilized paclitaxel, and (c) as-supplied and (d) lyophilized ciprofloxacin. Large clusters of particles may be artifacts of the sample preparation (i.e. drying of suspended particles), and are not necessarily indicative of the collected aerosols.

along their lengths.

Figure 5.6 shows an SEM image of ciprofloxacin particles, loaded with magnetite nanoparticles, prepared by lyophilization, and collected on the polycarbonate membrane filter in the presence of a magnetic field. Although the majority of the single, high aspect ratio particles appears to align in the direction of the field, a large fraction of the aerosol that penetrated the mouth-throat geometry and reached the membrane filter exists in agglomerates of many particles. As seen at higher magnification in figure 5.7, though these agglomerates have quite large geometric diameters, they are highly porous, and therefore have low enough aerodynamic diameters to avoid deposition by inertial impaction in the mouth-throat geometry.

Even at the fairly high magnification of figure 5.7, magnetite nanoparticles are not clearly visible on the surfaces of the ciprofloxacin particles; however, the membrane samples were sputter coated with an approximately 10 to 20 nm thick layers of gold in order to be visible by SEM, and this coating may conceal the magnetite nanoparticles. Figure 5.8 is a transmission electron micrograph (TEM) of a single particle from the lyophilized ciprofloxacin/magnetite powder, in which clusters of magnetite are visible on the particle surface. This sample was prepared by dusting a small amount of the powder over a TEM grid.

020967 8.0KV X200
150um

Figure 5.6. A scanning electron microscope image of magnetite loaded ciprofloxacin particles penetrating the mouth-throat geometry, and collected with a magnetic field produced parallel to the face of the membrane filter.

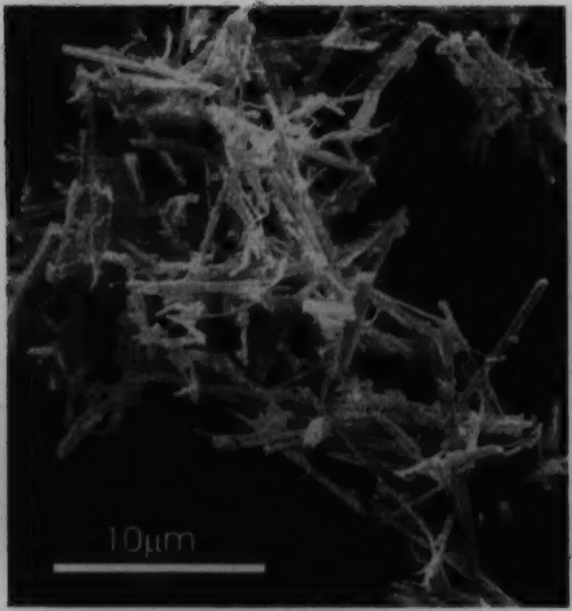

Figure 5.7. Identical to figure 5.6, but at higher magnification.

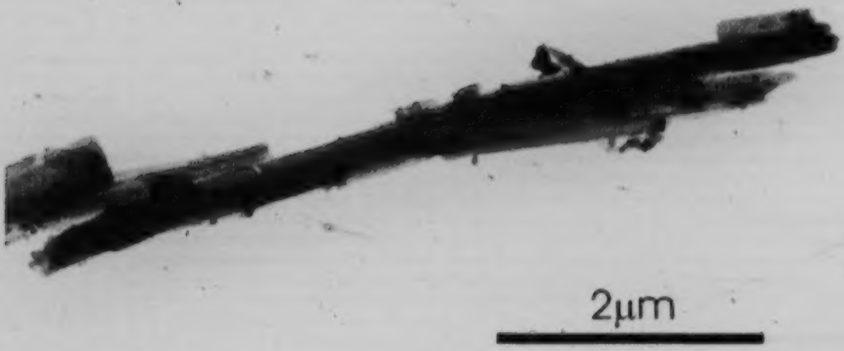

Figure 5.8. Transmission electron microscope image of ciprofloxacin loaded with magnetite. The darker black patches are clusters of magnetite nanoparticles.

5.3. Discussion

The work described above evaluated the suitability of dry powders containing high aspect ratio drug particles for delivery to the lung via inhalation. In addition, the possibility that such powder formulations be used for localized targeting through magnetic alignment was investigated. A simple bench test was employed to determine *in vitro* lung doses, in which the powders were dispersed using a commercial dry powder inhaler through an idealized mouth-throat geometry, and the fraction of drug reaching a filter placed downstream from the mouth-throat was deemed the lung dose. For compact aerosol particles, this test has previously shown good agreement with *in vivo* lung doses from dry powder inhalers and metered-dose inhalers (Zhang *et al.*, 2007), and reasonably good agreement with the FPF < 5.6 μm measured using a cascade impactor (Wang *et al.*, 2006). For one case studied above, that of the high capsule loading of as-supplied ciprofloxacin powder, no significant difference was found between the *in vitro* lung dose and the FPF < 5.6 μm measured by cascade impaction. However, in general, for high aspect ratio particles losses due to interception can occur between cascade impactor stages (Collazo *et al.*, 2002), or on incorrect stage plates. In addition, the aerodynamic diameter of nonspherical particles is dependent on their orientation, and there is no guarantee that the distribution of particle orientations in the cascade impactor will be the same as that during transit through the mouth and throat, so that the simple bench test used here is likely to be a more accurate experimental method than cascade impaction for estimating lung doses of high aspect ratio aerosol particles.

While the powders exhibited varying *in vitro* lung doses, which in some cases were quite high, these lung doses appear to include significant fractions of multiparticle agglomerates. In general, the agglomerates do not share the elongated shape of the individual drug particles; therefore, magnetic alignment is not expected to influence their deposition in the lung. This, of course, would limit the increase in deposition that could be achieved at targeted sites. If powder formulations are to be employed for targeting delivery through magnetic alignment, future work is required in order to improve deaggregation of agglomerates, or to remove them from the inhaled air stream.

Wang *et al.* (2006) improved the performance of a prototypical dry powder inhaler by placing a fine mesh, with 38 μm pore size, at the outlet of the device. This mesh broke up helical vortices in the flow exiting the inhaler that are thought to contribute to high mouth-throat deposition with no mesh present, but also captured and/or deaggregated large agglomerate particles through impaction and interception with the mesh (Wang *et al.*, 2006). Whether a similar approach can be used to remove agglomerates consisting of many high aspect ratio particles from inhaled air streams may merit exploration in future studies. That said, it must be kept in mind that optimal high aspect ratio particles for targeting through magnetic alignment would have smaller diameters than either the ciprofloxacin base or paclitaxel particles studied above, so as to minimize their lung deposition due to impaction and sedimentation. These smaller diameter particles would very likely be more difficult to disperse than either the ciprofloxacin or paclitaxel particles, owing to the increased adhesive forces between smaller particles relative to the aerodynamic lift and drag forces that disperse them (Finlay, 2001). As seen in table 5.1, *in vitro* lung doses were considerably smaller for the ciprofloxacin powders than for the paclitaxel powders. This reduction can likely be attributed to the smaller diameters of the ciprofloxacin crystals compared to the paclitaxel crystals, though other mitigating factors, such as the surface energies of the two compounds, were not evaluated. All else being equal, it is anticipated that further decreases to the diameters of high aspect ratio particles contained in dry powders would lead to further reductions in the dose delivered to the lung due to inefficient powder deaggregation.

On the positive side, for both the ciprofloxacin base and paclitaxel powders, *in vitro* lung doses were improved by lyophilizing the powders supplied by the manufacturers in order to reduce their bulk densities. Furthermore, because these powders were composed entirely of drug, with no excipient carrier particles, the *in vitro* lung dose was as high as nearly 5 mg (for the high capsule loading of ciprofloxacin). The ability to deliver several milligrams of drug to the lung in a single breath is attractive for administration of antibiotics, such as ciprofloxacin, and chemotherapeutic agents, such as paclitaxel, where minimum effective doses are typically much larger than those for therapeutic agents used to treat asthma and COPD. As both ciprofloxacin base and paclitaxel are lipophilic compounds, once deposited, they will dissolve slowly in the fluid lining the lung, and, in the peripheral regions of the lung, be subject to clearance by alveolar macrophages. That said, phagocytosis and clearance of sparingly soluble particles from the alveolar region of the lungs is generally believed to occur over a time scale of at least several days, so that sustained release of drug due to slow dissolution may be possible within this time period. Furthermore, it has previously been proposed that large, porous, spherical particles might avoid phagocytosis if their geometric diameters are on the same order as, or greater than, macrophage diameters (Lombry *et al.*, 2004). Such an argument may extend to high aspect ratio particles with lengths greater than macrophage diameters, approximately 10 to 20 μm, given the established link between the lengths of insoluble fibers and their biopersistence in the peripheral lung (Moolgavkar *et al.*, 2001). In the present work, *in vitro* lung doses of both ciprofloxacin and paclitaxel were shown to contain many particles greater than 20 μm in length. While it may initially seem surprising that such long particles were able to penetrate the idealized mouth-throat geometry, the relatively weak dependence of equivalent spherical aerodynamic diameters on particle lengths is well known, and was discussed in detail in section 2.5 of this thesis.

6. MRI MEASUREMENT OF REGIONAL LUNG DEPOSITION IN ANIMALS

6.1. Introduction

As noted in the background chapter of this thesis, in section 2.6, the potential use of magnetic fields to influence regional lung deposition of inhaled pharmaceutical aerosols has gained considerable attention recently (Coates, 2008; Plank, 2008). Superparamagnetic iron oxide nanoparticles have been used to imbue aerosol particles with high magnetic susceptibility, allowing their trajectories (Dames *et al.*, 2007) to be controlled at a distance using high gradient magnetic fields. While magnetic fields are attractive for external control over particles located within the body, due to their very low attenuation in biological tissue (Wilson and Saffer, 1995), high gradient fields are very difficult to generate at distances of more than a few centimeters from their sources. Therefore, scale up of successful experiments performed using high gradient fields in small animal models to larger animals and humans has traditionally proven difficult (Dobson, 2006). The targeting methodology proposed in the present thesis, that of magnetic alignment of high aspect ratio particles with uniform or low gradient magnetic fields, eliminates this difficulty. In addition, recent numerical work (Shang *et al.*, 2008) has indicated that control over particle shape may be possible using high frequency magnetic fields to induce eddy current heating and thermal bending of inhaled high aspect ratio particles loaded with ferromagnetic nanoparticles. Though considerable hurdles remain before such technologies find clinical application, the ability to noninvasively enhance aerosol deposition at localized sites within the lung, using externally applied magnetic fields, would mark a significant step forward in respiratory drug delivery.

In addition to their potential use in targeting drug delivery, iron oxide nanoparticles are widely used as contrast agents for magnetic resonance imaging (MRI) (Weinmann *et al.*, 2003; Bellin, 2006). Accordingly, for the intravenous route of administration, iron oxide nanoparticles have been used for combined magnetic targeting and subsequent, MRI-based assessment of nanoparticle concentrations within targeted sites in both clinical trials (Lemke *et al.*, 2004) and animal models (Chertok *et al.*, 2008). Very recently, Sood et al. (2008) have used MRI to estimate gadolinium concentrations averaged over the entire lungs of newborn pigs exposed to nebulized solutions containing gadopentetate dimeglumine (Gd-DTPA). The work described in this chapter examines the possibility that MRI might be used to determine the distribution of inhaled iron oxide nanoparticles within the lung. Clearly, measurement of regional deposition patterns by MRI would be ideally suited for *in vivo* evaluation of magnetic drug targeting techniques employing aerosols loaded with iron oxide nanoparticles. The ability to noninvasively quantify the level of targeting achieved in individual patients would be of great benefit, providing researchers with direct feedback on the success or failure of novel magnetic targeting techniques, and enabling correlations to be established between deposition enhancement at targeted sites and clinical outcomes.

In the work decribed below, mice were exposed nose-only to nebulized droplets containing superparamagnetic iron oxide nanoparticles. The feasibility of measuring lung concentrations of iron oxide nanoparticles using MRI was assessed by comparing lung tissue longitudinal, or T_1, relaxation times of exposed mice with those of baseline, non-exposed mice. Regional variation in deposition was assessed by comparing iron concentrations in the left and right lung measured in different axial slices. Subsequently, a very small pilot study was undertaken in mechanically ventilated rabbits exposed intratracheally to iron oxide loaded cromoglycic acid particles. Regional iron concentrations were assessed for rabbits with and without a magnetic field produced across the right lung.

6.2. Experimental Methods

6.2.1. Materials and Animals

Colloidal superparamagnetic iron oxide with an iron concentration of 10 mg/ml, and reported core particle size of 10 nm was purchased (FeREX; BioPAL, Worcester, MA). Cromoglycic acid crystals were prepared as described in chapter 4 of this thesis. Six to eight week old female BALB/c mice were obtained from the Health Sciences Laboratory Animal Services at the University of Alberta. Adult New Zealand White rabbits were obtained from Charles River Laboratories (Wilmington, MA). The animals were housed under conventional conditions under the guidelines of the Canadian Council on Animal Care for one week prior to the study. All animal procedures were approved by the University of Alberta Health Sciences Animal Policy and Welfare Committee.

6.2.2. Aerosol Exposure

The aerosol exposure apparatus used for the mice was nearly identical to that used previously by Nadithe *et al.* (2003). Briefly, LC Star jet nebulizers (PARI GmbH, Starnberg, Germany), operated with Devilbiss PulmoAide compressors (American Allergy Supply, Houston, TX), were used to supply droplets containing colloidal iron oxide nanoparticles to a nose-only inhalation chamber. The vents of the nebulizers were sealed to prevent additional room air from being drawn into the system. The downstream side of the inhalation chamber was connected to a house vacuum in order to maintain atmospheric pressure inside the chamber. Prior to the exposure, the output rate of colloidal iron oxide from the nebulizers was determined by placing three Respirgard filters (Vital Signs, Totowa, NJ) in series at the nebulizer exit. Nebulization was allowed to proceed until completion, and then the filters were weighed to determine the mass of aerosol generated. In addition, the droplet size distribution inside the chamber was also determined, prior to the exposure, using an Aerosizer (Amherst Process Instruments; now TSI, Shoreview, MN) to sample aerosol from the nose ports of the chamber, at a sampling flow rate of 1 l/min. Aerosol was sampled from the six ports later occupied, during the exposure, by mice.

Six mice, weighing 22.5 ± 1.2 g (mean ± one standard deviation), were placed inside restrainer tubes and exposed nose-only to nebulized iron oxide for two hours. Due to the length of the exposure, the nebulizer and compressor were switched out of the circuit and replaced two times. Each time, flow of air through the chamber was maintained using the house vacuum, and less than two minutes elapsed before the new nebulizer and compressor were in place and again producing aerosol. The mice were euthanized immediately after the exposure by intraperitoneal injection of euthanyl, and then placed in a refrigerator, at 4 °C, in supine position, until the time of their MRI scans. The time of death and time of MRI scan was recorded for each mouse.

In addition to the exposed mice, a group of six baseline mice was studied, with mean weight of 22.8 ± 0.3 g. Two of these mice underwent a blank two-hour exposure to isotonic saline, after which they were euthanized together with the remaining four baseline mice, and refrigerated until scanned. As for the exposed mice, times of death and scanning were recorded for each mouse.

For the rabbit exposure, an Aeroneb vibrating mesh nebulizer (Aerogen, now Nektar, San Carlos, CA) and diffusion dryer were inserted into the inspiratory arm of a mechanical ventilation circuit (InfantStar; Infrasonics Inc., San Diego, CA), as is depicted schematically in figure 6.1. For each rabbit, after anesthesia, a tracheostomy was performed, and a 3.5 mm endotracheal tube was inserted into the trachea. The trachea was tied around the endotracheal tube to prevent leaking. Mechanical ventilation was performed using 100% oxygen with a peak inspiratory pressure of 14 cm water, a positive end-expiratory pressure of 2 cm water, a continuous flow of 6 l/min., and an inspiratory time of 0.5 s. The inspired gas was neither warmed nor humidified. The breath frequency was adjusted between 20 and 25 breaths per minute in order to maintain an arterial PCO_2 between 35 and 40 mm Hg.

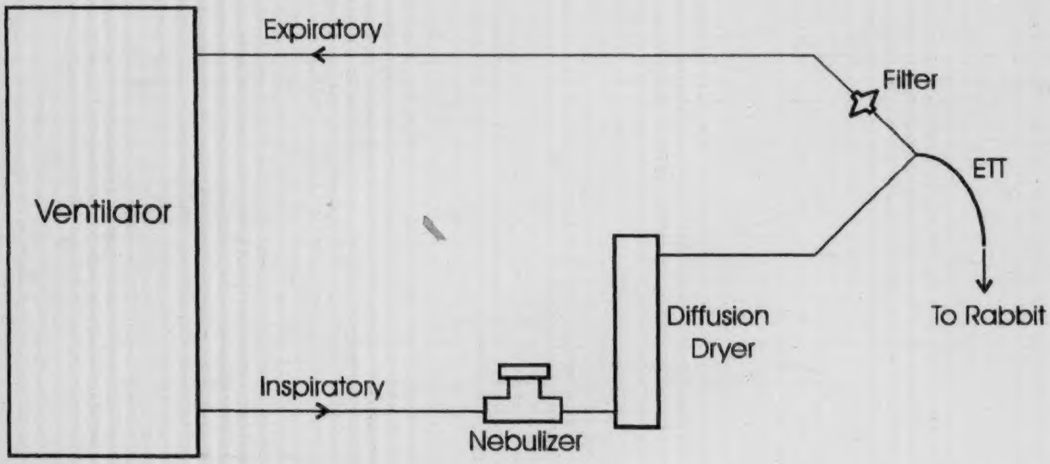

Figure 6.1. Schematic of the ventilator circuit used to expose rabbits to iron oxide loaded cromoglycic acid aerosol (ETT, endotracheal tube).

All rabbits used in the study weighed between 3.4 and 4 kg. A group of three control rabbits underwent mechanical ventilation for approximately 30 min. each, but were not exposed to any aerosol. A second group of three rabbits were exposed during mechanical ventilation to iron oxide loaded cromoglycic acid (CA) particles. These particles were produced in the inspiratory limb of the ventilator by nebulizing suspensions containing 10 mg CA and 150 µl FeREX in 5 ml deionized water, and then allowing all water to evaporate from the nebulized droplets in a diffusion dryer. For each exposed rabbit, two 5 ml doses were delivered; the nebulizer reservoir was refilled after completion of the first dose without interrupting ventilation. A filter (Respirgard; Vital Signs, Totowa, NJ) was inserted into the expiratory limb of the circuit in order to collect all wasted aerosol.

Finally, two rabbits underwent an identical exposure to that outlined above, except that a magnetic field was produced across their right lungs. To produce the field, neodymium permanent magnets (two stacks of three, 2" x 2" x 0.5" magnets; Indigo Instruments, Waterloo, ON) were placed above and below the thorax. The centers of the magnets were positioned approximately in line with the center of the right lung, by eye. The magnets were separated by 20 cm, with the rabbits in supine position and closer to the lower magnet. In this arrangement, any small translational magnetic force associated with field gradients was in the same direction as the gravitational force. The field strength and gradient decreased from approximately 35 mT and 1.5 T/m, respectively, in the dorsal lung to 20 mT and 0.1 T/m in the ventral lung. For all five exposed rabbits, ventilation lasted for 45 ± 9 min., with aerosol produced for 23 ± 1 min. All rabbits were sacrificed upon completion of ventilation. The time between death and MRI scan was held between 40 and 70 min. for all rabbits.

In order to estimate the concentration of aerosol in the ventilator circuit, the mass of iron collected on the expiratory filter was assayed for each exposed rabbit. Iron oxide nanoparticles were dissolved from the filter in concentrated hydrochloric acid, after which iron concentrations were determined by UV spectrophotometry (8452A; Hewlett-Packard, Palo Alto, CA) using the classical method of Fe(III)-thiocyanate complex formation (e.g. Riganakos and Veltsistas, 2003; Suwa *et al.*, 1998). Given that the MRI measurements of lung deposition were also in terms of iron masses, in order to infer regional drug concentrations from iron concentrations it was necessary to demonstrate a reasonably even distribution of iron across the polydisperse CA particles. For this purpose, size distribution measurements were made by drawing iron oxide loaded CA particles from the nebulizer/drying tube combination through a cascade impactor (Mark II Andersen Impactor; Thermo Andersen, Smyrna, GA) at 28.3 l/min. The masses of CA and iron depositing on each stage of the impactor were determined by UV spectrophotometry, using the methods described elsewhere in this thesis. Three experimental repetitions were performed for both the CA assay and the iron assay. For each repetition, the nebulizer was filled with a 5 ml dose containing 10 mg CA and 150 µl FeREX, and nebulization was allowed to proceed to completion.

6.2.3. MRI Imaging and Post-Processing

MRI measurements were made using a Siemens Sonata 1.5 T, 60 cm bore system (Siemens Medical Systems, Erlangen, Germany). Subsequent to the experiments performed in mice, each mouse was oriented prone, in the right to left direction, in a 2.5 cm diameter surface coil, with the center of lung placed at the center of the circular coil to maximize reception sensitivity and uniformity over the lungs. An inversion-recovery fast spin echo pulse sequence with a variable inversion recovery time (T_I ranging from 200 ms to 2000 ms in increments of 200 ms, as well as the case of no inversion, or $T_I = \infty$) was used to quantify the longitudinal relaxation time of the lungs, with the following imaging parameters: 108 x 25 mm field of view, 448 x 105 matrix (240 x 240 µm in-plane spatial resolution, interpolated to 120 x 120 µm), and a 1 mm slice thickness with 12 slices spanning the lung from its apex down to the diaphragm. Two serial experiments, each with 6 slices separated with a 1 mm slice gap, were interleaved to ensure there was no cross-talk between neighboring slices. Other pulse sequence parameters included a repetition time, TR, of 4000 ms, an echo time, TE, of 16 ms, a 150 Hz/pixel bandwidth, a 15.9 ms echo-space with 11 echoes per excitation, and 2 averages. The total acquisition time was approximately 30 minutes for each mouse.

The MRI procedure for the rabbits was very similar to that for the mice, save that a larger surface coil was used to accommodate the larger bodies of the rabbits. In addition, the sequence of inversion recovery times used for the rabbits was T_I = 100, 300, 600, 1000, 1500, 2000, 3000, and 4000 ms, and 24 2.5 mm thick axial slices were used to span the lung, with an in-plane spatial resolution interpolated to 500 x 500 μm. As for the mice, the total acquisition time for each rabbit was approximately 30 minutes.

For post-processing of the mouse images, a MATLAB (The Mathworks, Natick, MA) script was written to calculate average T_1 relaxation times for user-defined regions of interest within the slices. For the analysis reported here, regions of interest encompassing the left and right lung were chosen in each slice. In order to limit the influence of the lung vasculature on T_1 relaxation times, all voxels with signal intensity greater than a threshold value were excluded from the regions of interest. A threshold level equal to 25% of the maximum signal intensity in an image was found to filter out the majority of the vasculature visible in the image. In addition, the average signal intensity (SI) in each region of interest was corrected for noise using the relationship

$$\mathrm{SI} = \sqrt{\mathrm{SI}_0^{\,2} - n^2} \tag{6.1}$$

where SI_0 is the average signal intensity prior to subtraction of the noise, n, measured as the average signal intensity in a region of interest far away from the mouse.

The T_1 relaxation time was determined in each region of interest by fitting average signal intensity versus inversion time data points with the function

$$SI = \mathrm{abs}\left[SI_{\infty}\left(1 - k \cdot e^{-T_i/T_1}\right)\right] \tag{6.2}$$

where SI is the signal intensity at inversion time T_i, and the constants SI_{∞}, k, and T_1 were determined by nonlinear regression.

For the rabbit images, regions of interest encompassing the left and right lung in each slice were also studied; however, in addition, within each slice T_1 values within the lung were mapped over a grid comprised of 15 x 15 voxel (7.5 x 7.5 mm) squares using a MATLAB routine developed by Kelvin Chow and Richard Thompson (Department of Biomedical Engineering, University of Alberta). Gray-level thresholding was applied at the local level, within each grid sub-region, in order to filter out vasculature.

The presence of iron oxide nanoparticles in the lung will decrease the T_1 relaxation time according to the following relationship (Rosenthal *et al.*, 1993; Suwa *et al.*, 1998):

$$\frac{1}{T_1} = \frac{1}{T_{10}} + \alpha \cdot c \tag{6.3}$$

where T_{10} is the baseline relaxation time, c is the tissue concentration of iron, and α is ideally a constant. Evaluation of equation (6.3) allowed the average concentration of iron within chosen regions of interest to be calculated from measured T_1 relaxation times in the exposed and baseline mice. For the iron oxide nanoparticles used in the present study a value of $\alpha = 0.15$ cm^3/(μg Fe·s) was determined by evaluating equation (6.3) using known concentrations of the nanoparticles prepared in agar phantoms and the corresponding T_1 and T_{10} values measured using inversion recovery MRI experiments. The phantoms contained 2% (w/v) agar in deionized water. Iron oxide nanoparticles were added to boiling agar solutions while stirring, and the resulting suspensions were then cooled and poured into 35 mm diameter, 10 mm deep glass petri dishes. Further cooling to room temperature formed agar gels containing well-dispersed suspensions of nanoparticles, with iron concentrations ranging from 0 to 20 μg/ml, over which range α remained constant.

6.3. Results

For the nose-only exposure in mice, the average output rate over the course of nebulization was 0.70 mg Fe/min. Accordingly, over the two-hour exposure, 84 mg of iron was introduced into the inhalation chamber. The size distribution of droplets containing the colloidal iron oxide was determined by sampling aerosol from the nose ports of the inhalation chamber. The mass median aerodynamic diameter (MMAD) of the aerosol was 5.6 ± 0.8 μm, with a geometric standard deviation (GSD) of 1.30 ± 0.03 (both values are expressed as mean ± one standard deviation, $n = 6$).

In the baseline mice, T_1 relaxation times in the right and left lung were measured at different axial positions. Figure 6.2 displays signal intensity images of twelve axial slices a

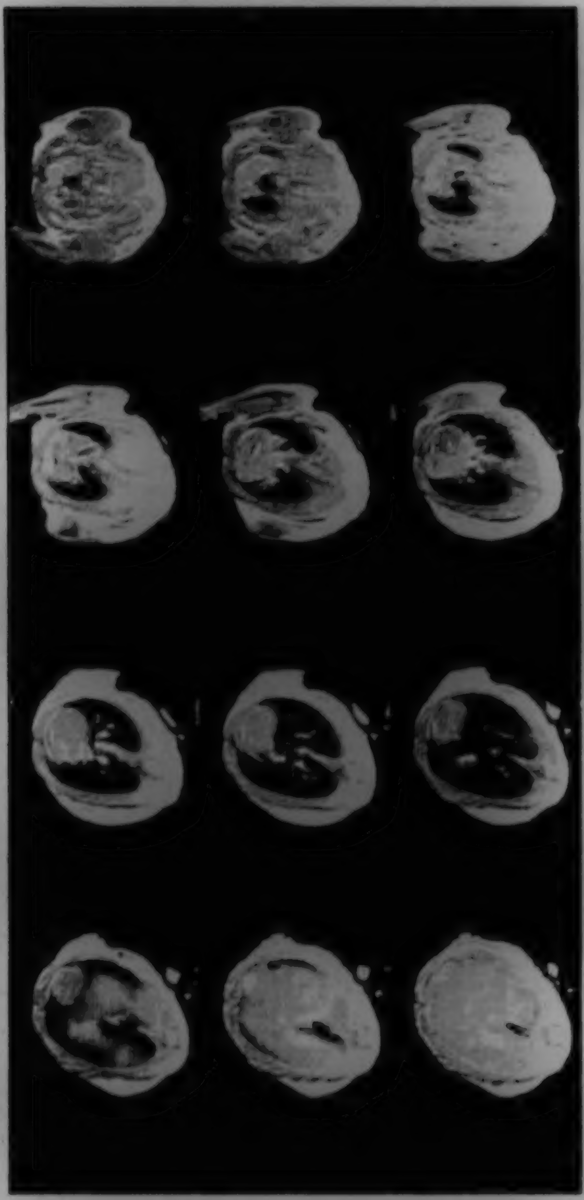

Figure 6.2. Signal intensity images (for $T_1 = \infty$) of twelve axial slices of the lung of a baseline mouse, moving from the trachea down to the diaphragm. Each image represents a 1 mm thick slice. The baseline and exposed mice were indistinguishable in raw signal intensity images such as these.

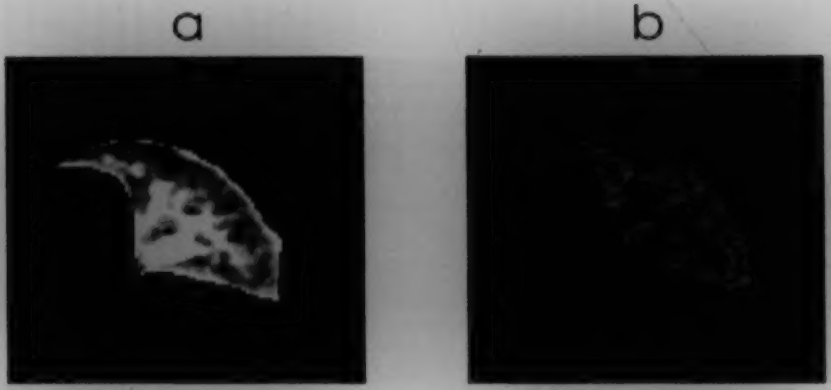

Figure 6.3. Signal intensity images (for $T_I = \infty$) of a specified region of interest (a) before and (b) after gray level thresholding to remove the vasculature, which appears as areas of very high intensity in (a). For the purpose of comparison, the grayscale is held constant between (a) and (b).

from one of the baseline mice, while figure 6.3 demonstrates the use of gray level thresholding to filter out the vasculature from a specified region of interest. In each individual baseline mouse, no variation in the T_1 relaxation time was detected with axial position, nor between the right and left lung. Therefore, for each mouse, the T_1 relaxation time was averaged over the whole lung. As shown in figure 6.4, the average T_1 relaxation time decreased with the time after death at which the MRI scan was performed. The first and the fifth mouse in this series were exposed to nebulized saline prior to euthanasia, but follow the same trend as do the remaining four baseline mice.

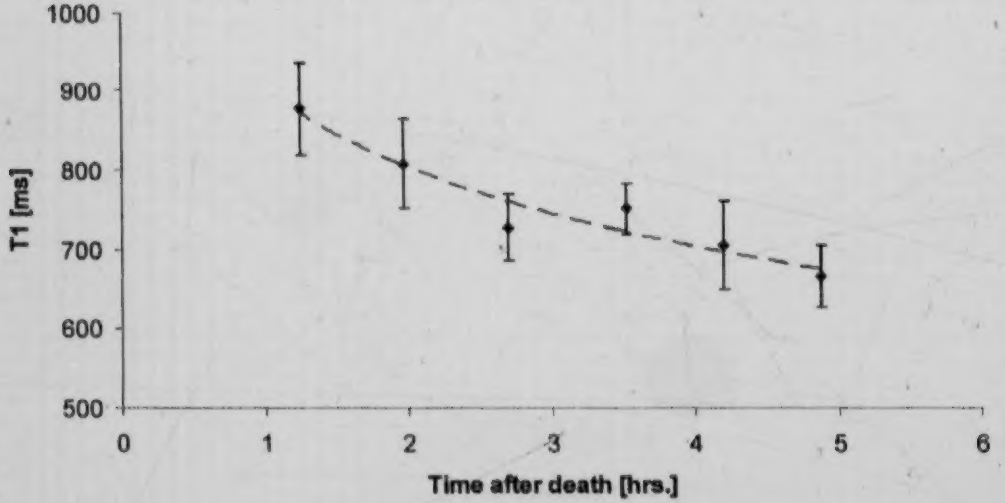

Figure 6.4. Average T_1 relaxation times in the lungs of the baseline mice are plotted against the time after death at which the MRI scan was performed. Error bars represent one standard deviation.

T_1 relaxation times in the exposed mice were also determined in the left and right lung, at each of twelve axial positions. T_1 relaxation times were converted to iron concentrations according to equation (6.3). For each exposed mouse, a unique baseline T_1 relaxation time, T_{10}, was used in equation (6.3) to account for the observed decay in T_{10} following death, as seen in figure 6.4. T_{10} was determined from the time after death of the mouse by interpolating from the data measured in baseline mice, using a best-fit logarithmic curve. Figure 6.5 displays average right and left lung iron concentrations in the exposed mice at different axial positions. In each mouse, moving from the trachea down to the

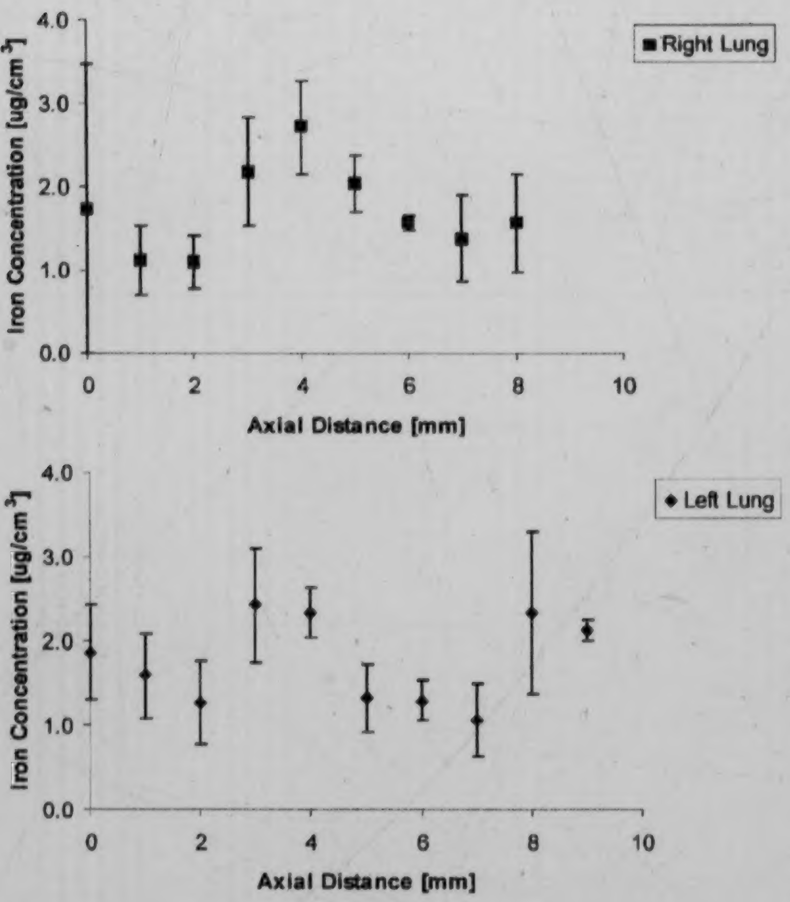

Figure 6.5. Concentrations of iron in the right and left lung, averaged over the six exposed mice, are plotted against the axial distance, moving from the apex to the base of the lung. Errors bars represent the standard error of the mean.

diaphragm, the first axial slice in which peripheral lung was visible was assigned an axial distance of zero, and the positions of subsequent slices were defined based on their axial distances from the zero position. The lung volume and total mass of iron deposited in the lung were determined for each exposed mouse based on the volumes of the defined regions of interest in each axial slice and the measured regional iron concentrations. The average lung volume, after thesholding to exclude voxels containing vasculature, was 0.28 ± 0.08 cm^3 (mean ± one standard deviation, $n = 6$). The average mass of iron deposited in the lungs was 0.5 ± 0.2 μg.

For the pilot study performed in rabbits, CA particles were loaded with iron oxide nanoparticles for the dual purpose of facilitating targeting by magnetic alignment, and enabling regional deposition measurement using MRI. Figure 6.6 displays the results of the cascade impactor experiments, which demonstrated a reasonably even distribution of iron over different sizes of CA particles. Statistically significant differences between iron-weighted and CA-weighted size distributions were observed only for plates 1 through 3, which represented a small fraction of the total aerosol mass.

For each individual control rabbit, the T_1 relaxation time varied little across different regions of the lung. The average T_1 time in the control rabbits was 1309 ± 150 ms (mean ± one standard deviation, $n = 3$). Table 6.1 presents average T_1 times in the left and right lung of the exposed rabbits. In addition, table 6.1 gives average left and right lung iron concentrations calculated from equation (6.3) under the assumption of a baseline T_1 time of 1309 ms, as well as the ratio between these two values.

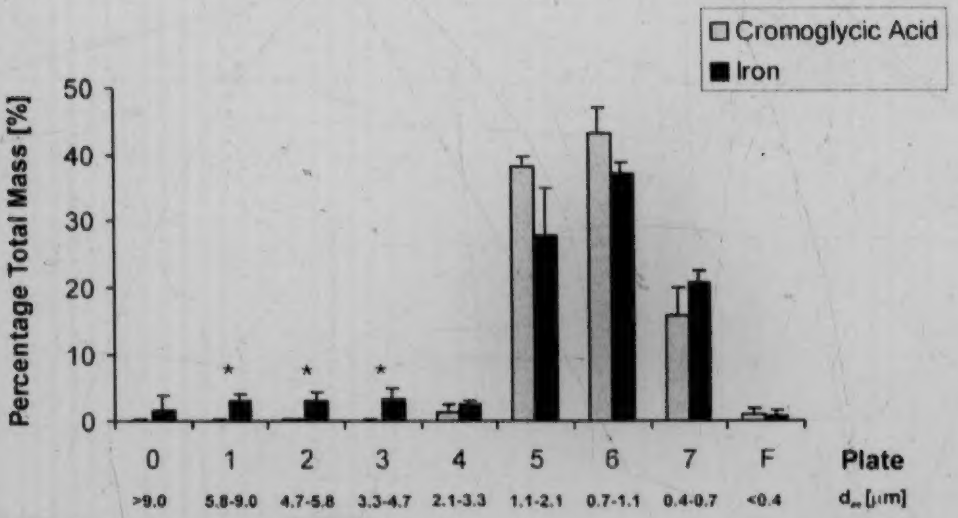

Figure 6.6. Aerodynamic size distributions weighted by mass of iron and mass of cromoglycic acid, as determined by cascade impaction for the iron oxide loaded cromoglycic acid aerosol. Asterisks indicate statistically significant differences between the two distributions ($P < 0.05$; two-tailed student's t-test for independent samples).

Table 6.1. Longitudinal Relaxation Times and Iron Concentrations in the Right and Left Lung of Rabbits Exposed to Iron Oxide Loaded Cromoglycic Acid Aerosol

	Left Lung		*Right Lung*		
Rabbit	T_1 [ms]	[Fe] [µg/cm^3]	T_1 [ms]	[Fe] [µg/cm^3]	$[Fe]_R/[Fe]_L$
Non-targeted 1	1118 ± 68	0.87	1114 ± 51	0.89	1.02
Non-targeted 2	1160 ± 131	0.65	1194 ± 112	0.49	0.75
Non-targeted 3	1238 ± 30	0.29	1206 ± 60	0.43	1.48
Targeted 1	1229 ± 51	0.33	1230 ± 60	0.33	1.00
Targeted 2	1224 ± 73	0.35	1174 ± 64	0.58	1.66

[Fe], lung iron concentration.

T_1 values are mean ± one standard deviation (weighted by voxel number over all axial slices).

Iron concentrations are calculated from equation (6.3) assuming $T_{10} = 1309$ ms.

On average, the ratio between right and left lung iron concentrations was 1.09 ± 0.38 (n = 3) in the non-targeted exposed rabbits, with no magnetic field across the right lung, and 1.32 ± 0.47 (n = 2) in the targeted exposed rabbits.

In addition to average values in the right and left lung, T_1 times were mapped over each axial slice for each rabbit. Figure 6.7 displays T_1 maps from a basal, medial, and apical slice for the second targeted exposed rabbit (Targeted 2 in table 6.1). For the medial and basal slices, T_1 times are lower in the right lung than in the left lung, indicating higher concentrations of iron in the targeted lung.

6.4. Discussion

In the present work, mice were exposed nose-only to nebulized droplets containing colloidal iron oxide. Concentrations of iron in the lungs of exposed mice were measured using MRI, based on reductions to the T_1 relaxation time of the lung tissue, compared to a baseline group of mice. In the baseline mice, the average lung T_1 relaxation time was found to decrease with time after death. These changes are most likely due to postmortem redistribution of water in the alveolar, interstitial and vascular spaces in the lung.

In the exposed mice, the concentration of iron was highest in axial slices containing central regions of the lung. This result is not surprising given the sizes of the aerosol droplets in the inhalation chamber, which had a MMAD of 5.6 ± 0.8 μm. The mathematical lung deposition model presented by Nadithe *et al.* (2003) predicted higher

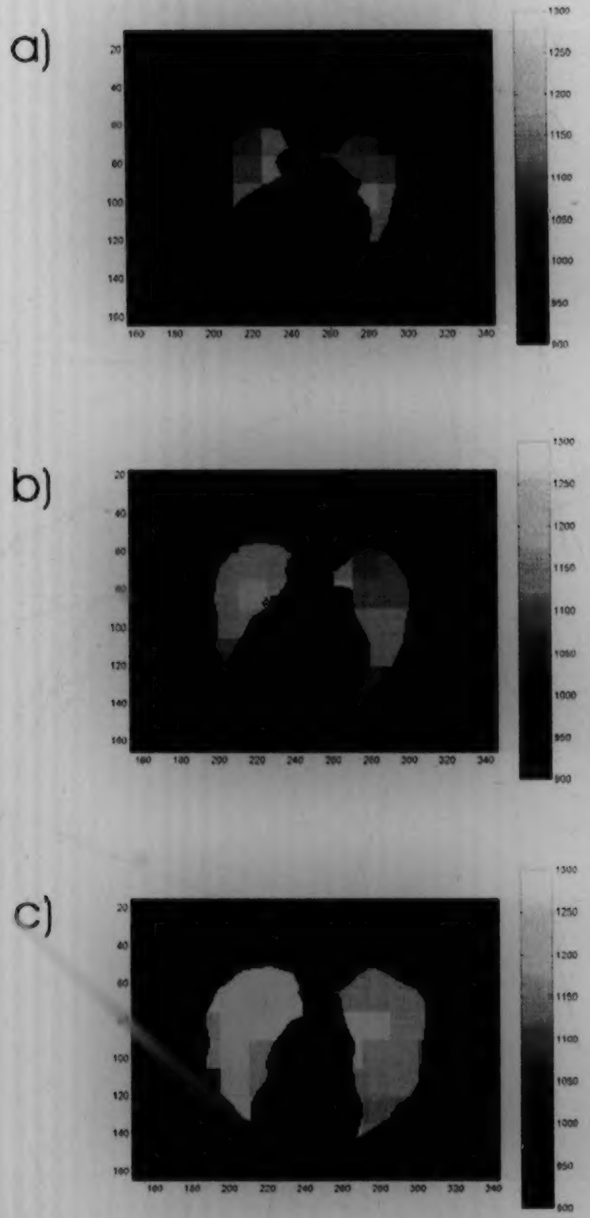
a)
b)
c)
20
40
60
80
100
120
140
160
160
180
200
220
240
260
280
300
320
340
1300
1250
1200
1150
1100
1050
1000
950
900

Figure 6.7. T_1 maps in a) apical, b) medial, and c) basal slices of the lung for one of the targeted exposed rabbits (Targeted 2 in table 6.1). For the medial and basal slices, T_1 times are lower in the right, compared to the left, lung.

tracheobronchial deposition than alveolar deposition in mice inhaling particles of several micrometers in diameter. The present results are consistent with this prediction, in that tracheobronchial airways are expected to be located primarily in the central, as opposed to peripheral, regions of the lung.

The total mass of iron that deposited in the lung of each exposed mouse was only 0.0006 ± 0.0002 % (mean ± one standard deviation, $n = 6$) of the mass of iron introduced into the inhalation chamber. This result is consistent with previous studies, in which nose-only, flow-by inhalation chambers have been shown to be extremely inefficient in terms of the amount of aerosol delivered to the lungs of rodents (Nadithe *et al.*, 2003; Costa *et al.*, 2006). Employing the same model of nebulizer and compressor, and the identical inhalation chamber as in the present study, Nadithe *et al.* (2003) measured the lung deposition of radiolabeled human serum albumin in mice using gamma scintigraphy. As a percentage of the total activity introduced into the chamber, the average lung deposition in each mouse was 0.0018%. This is three times higher than the lung deposition measured in the present study; however, the reported MMAD of the aerosol was lower than that in the present study, 3.9 μm compared to 5.6 μm, so that losses in the chamber, and in the extrathoracic airways of the mice, were likely greater in the present study. In addition, differences in the exposure times and the genetic strains of mice used in the two studies may have contributed to the difference in measured lung deposition.

Based on the observed decrease in T_1 relaxation time with time after death in mice, the time between sacrifice and MRI scan was controlled much more tightly in the rabbit study. Nonetheless, the average T_1 time varied considerably between the control rabbits. This is likely not a post-mortem effect, but rather a reflection of normal intersubject variation in lung T_1 times (e.g. Stadler *et al.*, 2005). Because of this variation, when using equation (6.3) to calculate lung iron concentrations, it would have been preferable to measure baseline and post-exposure T_1 times in the same animal. Unfortunately, the MRI facility at which the present studies were performed does not currently permit experiments to be performed on live animals, so that measurements of T_1 times before and after exposure were not possible.

As was mentioned in the introduction to this chapter, the ability to quantify regional deposition of superparamagnetic iron oxide nanoparticles within the lung is attractive for *in vivo* evaluation of aerosol-based approaches to magnetic drug targeting. In the rabbit study, T_1 times were mapped, albeit at a somewhat coarse resolution, over each axial slice of the lung. The MRI scanner used for this study is a whole body human system, and thus is not optimized for the study of animals. Accordingly, significant improvements in resolution may be possible when detecting regional variations in iron concentration in the study of larger animals and humans. T_1 mapping in the human lung has previously been reported (Arnold *et al.*, 2004; Stadler *et al.*, 2005; Stadler *et al.*, 2008), so that the technical feasibility of such measurements in humans is established.

On average, the ratio between right and left lung iron concentrations was higher in targeted than non-targeted exposed rabbits. While this result was not statistically significant for the very small number of animals used in the pilot study, the increase is in line with expectations based on the analytical model presented in chapter 3 of this thesis. A statistical power analysis was undertaken to estimate the number of rabbits that would be required in a future study to avoid a type II error (that is, a false negative). In this analysis, it was assumed that the right to left lung iron concentration will tend towards unity as the number of non-targeted exposed rabbits increases, and that the standard deviation for the targeted rabbits will decrease somewhat as the sample size increases above 2. Therefore, the power analysis was performed for an estimated ratio of 1.0 ± 0.3 in the non-targeted rabbits, increasing to 1.3 ± 0.3 in the targeted rabbits, based on a one-tailed t-test for independent samples. With these assumptions, 14 rabbits in each group would yield a power of 0.80. If the ratio in the targeted rabbits is, more optimistically, estimated as 1.4 ± 0.3 or 1.5 ± 0.3, a power of 0.80 would be achieved with 8 or 6 rabbits, respectively.

In addition to evaluating regional deposition patterns, MRI measurement of iron concentrations within the lung, and in secondary organs, may be useful for determining clearance rates of insoluble particles *in vivo*. Techniques using gamma scintigraphy are widely used to measure short-term, mucociliary clearance over 24 hours. The observation time in these studies is limited by the short half-life of the radiolabel, usually technetium-99m. In limited cases, clearance has been measured by scintigraphy over several days, and even months, using radiolabels with longer half-life and sensitive counters (Falk *et al.*, 1999; Lindstrom *et al.*, 2005). Alternatively, Möller *et al.* (2004; 2006) measured whole-lung retention of inhaled micrometer-sized iron oxide particles over a time period of nine months, using a superconducting quantum interference device

(SQUID) to detect remanent magnetic fields produced by magnetized particles. Similar studies may be possible using MRI after inhalation of superparamagnetic iron oxide nanoparticles, or larger insoluble particles labeled with a MRI contrast agent, with the added benefit of obtaining regional deposition patterns. If such studies are undertaken, a potential limiting factor is the sensitivity of the T_1 relaxation time of the lung, and of secondary organs, to the tissue concentration of contrast agent. This sensitivity is captured in the parameter α, in equation (6.3). In the present work, iron concentrations in the lung down to 0.33 $\mu g/cm^3$ were estimated using average T_1 times in control animals as baseline values. While smaller concentrations would have been difficult to detect in the present work, the sensitivity would be improved if true baseline T_1 values were measured for each individual animal.

In summary, based on the work described above, it can be concluded that MRI measurement of T_1 relaxation times shows considerable promise as an experimental technique for determining regional lung deposition of inhaled superparamagnetic iron oxide particles. As was demonstrated in a very small pilot study in rabbits, such a technique is well suited for evaluation of aerosol-based magnetic drug targeting to localized sites within the lung, where drug or carrier particles are already loaded with iron oxide nanoparticles in order to increase their magnetic susceptibilities. In addition, as an alternative to scintigraphy, MRI may prove useful in determining particle concentrations in the lung during long-term clearance studies.

7. DISCUSSION OF RESULTS AND SUGGESTIONS FOR FUTURE WORK

The work described in this thesis presents a novel approach to targeting the delivery of inhaled pharmaceutical aerosols to specific, localized regions of the lung. Elongated, high aspect ratio drug particles were loaded with superparamagnetic magnetite nanoparticles so that the composite particles would align in the direction of an externally applied, low gradient magnetic field. Normally, in the airways of the lung, high aspect ratio particles predominantly align with flow streamlines due to the aerodynamic torque that results from shear in the entraining flow. This shear alignment limits deposition of the particles onto airway walls by the interception mechanism because the particles are aligned parallel to the walls, minimizing their effective interception length. As a result, aligning the particles in any other direction, through the application of an external magnetic field, will increase their probability of interception. If the dimensions of the particles are chosen so as to minimize airway deposition due to other mechanisms, including inertial impaction and gravitational sedimentation, the expected increase in interception will lead to an overall increase in deposition. Furthermore, by applying a magnetic field only across a specified region of the lung, local targeting to that region can be achieved. In general, to minimize deposition due to impaction and sedimentation, the diameters, or shortest dimensions, of the high aspect ratio particles should be below approximately one micrometer. Conversely, the lengths, or longest dimensions, of the particles can be extended to tens of micrometers, in order to enhance interception, with little consequence to other deposition mechanisms, owing to the relatively weak dependence of high aspect ratio particle settling velocities and Stokes numbers on particle lengths.

In practice, it will likely be difficult to produce a magnetic field at any preferred orientation with respect to targeted airways. Rather, producing a magnetic field across a collection of randomly oriented airways in the peripheral lung would result in randomly oriented particles with respect to those airways. For this reason, in the analytical model of high aspect ratio particle deposition presented in chapter 3, deposition was compared for particles with random and parallel orientations with respect to airway walls. These two cases were used, respectively, to estimate deposition of particles aligned with a magnetic field, and particles aligned with flow streamlines in the absence of a magnetic field. As was described in chapter 3, the predictions of the analytical model indicated that targeting by magnetic alignment would be most effective at lung generations around the terminal bronchioles, although it was predicted that at least a moderate level of targeting is possible in airways spanning generations 9 through 20, which encompasses a substantial portion of the approximate 23 generations of the lung. Targeting is most effective in generations near the terminal bronchioles because the diameters of these airways are sufficiently small that interception becomes a significant deposition mechanism, but particle residence times in the airways are not so long that gravitational sedimentation becomes dominant.

In chapter 4 of the thesis, *in vitro* deposition experiments were performed using elongated cromoglycic acid crystals as model drug particles. Suspensions containing cromoglycic acid crystals and superparamagnetic magnetite nanoparticles were nebulized and dried to produce an aerosol of magnetite-loaded high aspect ratio drug particles. This aerosol was polydisperse with volume median diameter of 0.47 ± 0.05 μm and volume median length of 3.0 ± 0.5 μm. The geometric standard deviations of lognormal distributions in the diameter and length were 1.6 ± 0.1 and 2.1 ± 0.2, respectively. In light of the analytical predictions presented in chapter 3, these particle dimensions were by no means optimal for maximum targeting by magnetic alignment, but were certainly adequate for providing an experimental demonstration of the concept. Case in point, deposition of the magnetite-loaded cromoglycic acid aerosol in idealized physical replicas of the terminal bronchioles increased by a factor of 1.74 when a low gradient magnetic field was applied across the airways, compared with the deposition observed with no magnetic field applied. This increase was in line with that expected from the analytical model for particles with similar dimensions. As was discussed in chapter 4, it is reasonable to expect that significantly larger increases in deposition will be possible through magnetic alignment of longer, sub-micrometer diameter particles.

Magnetic drug targeting of inhaled aerosols using high gradient magnetic fields to produce translational magnetic forces on particles has also been proposed recently (Ally *et al.*, 2005; Dames *et al.*, 2007). A major obstacle in the application of such approaches lies in the difficulty of producing sufficiently large field gradients within the body to influence particle trajectories (Dames *et al.*, 2007; Coates, 2008; Plank, 2008). For this reason, the experience of researchers using magnetic forces to target intravenous drug delivery has been that experiments performed in small animals, whose entire bodies can be placed very close to magnetic field sources (that is, permanent magnets or electromagnets) and thus in regions of high field gradients, do not translate to successes in larger animals and humans (Dobson, 2006). As can be surmised from the nondimensional analysis of particle motion described in chapter 4 of the present thesis, for relatively modest magnetic field gradients of not more than a few Tesla per meter, which may possibly be generated at depth within the human lung using currently available systems of permanent magnets, the effect of the magnetic force on particle motion will be on the order of that due to gravity. This implies that targeting using a translational magnetic force will be most effective in the most distal generations of the lung's alveolar region, where gravitational sedimentation is dominant, and the magnetic force is used to augment that of gravity (that is, the magnetic force is directed in parallel with that due to gravity). Again, the alternative approach to magnetic targeting examined in the present work, which relies on alignment of high aspect ratio particles, requires no gradient in the magnetic field applied to targeted airways. As was noted above, this type of targeting is likely to be most effective in the bronchioles and upper generations of the alveolar region, where enhanced interception with airway walls is not overshadowed by any other, more dominant, deposition mechanism. It should be noted here that these two approaches to magnetic targeting of inhaled aerosols need not be mutually exclusive; for example, alignment of high aspect ratio particles in the direction of gravity would also enhance sedimentation, as the particles have a maximum settling velocity at such an orientation. In fact, in applications where broad targeting to the entire periphery of a lobe is required, targeting by magnetic alignment of high aspect ratio particles may benefit from the additional effects of small field gradients, which could enhance deposition in the most distal airways, where targeting due to interception is least effective.

In addition to magnetic targeting applications, superparamagnetic iron oxide nanoparticles are widely used as contrast agents in magnetic resonance imaging (MRI). Chapter 6 of this thesis demonstrated the feasibility of measuring regional lung deposition using MRI of mice exposed nose-only to nebulized water droplets containing iron oxide nanoparticles. Such a technique is obviously well suited for evaluation of magnetic drug targeting of inhaled pharmaceutical aerosols to localized sites within the lung, where drug or carrier particles are already loaded with iron oxide nanoparticles in order to increase their magnetic susceptibilities. As a demonstration, a very small pilot study was conducted in mechanically ventilated rabbits exposed intratracheally to iron oxide loaded cromoglycic acid aerosols. A magnetic field was positioned over the right lung in order to increase deposition over that occurring with no magnetic field in place. Lung iron concentrations were measured by MRI in rabbits exposed with and without magnetic targeting. On average, the ratio of right lung to left lung iron concentration was higher with the magnetic field applied, than without; however, this result was not statistically significant for the very small number of animals studied. As such, a statistical power analysis was performed in order to estimate the number of animals that would be required to avoid type II errors in a larger, future study. It is recommended that such a study be conducted in animals no smaller than the rabbits used in the present thesis. A larger total lung volume allows magnetic fields to be produced more easily across localized regions of the lung. In addition, larger rates of ventilation limit waste of continuously generated aerosols, and, furthermore, larger animals can more readily be exposed via intubation and mechanical ventilation, eliminating losses in the extrathoracic airways, which are particularly high for animals that are obligate nose breathers. Given these advantages, larger animal models seem attractive for future studies of localized targeting using magnetic alignment of inhaled, high aspect ratio particles. MRI is a logical choice for measuring regional deposition in such studies, and could also be used for noninvasive, *in vivo* assessment of magnetic targeting in human patients during clinical studies.

In the introduction to this thesis, lung cancer was identified as a disease that might benefit from the development of technologies that improve localized targeting of inhaled pharmaceutical aerosols. The vast majority of drugs used for chemotherapy are toxic not only to cancerous cells, but also to healthy cells; therefore, minimizing the exposure of healthy tissue to these drugs is critical in limiting side effects. Currently, delivery of chemotherapeutic agents to the lung through the inhalation route using conventional aerosol delivery systems is receiving considerable attention, and has generated some debate. A recent review of aerosolized chemotherapy was presented by Gagnadoux *et al.* (2008). Compared with systemic administration, delivery of chemotherapeutic agents directly to the lung seems a very logical approach to treating both primary and metastatic lung cancers. Inhaled chemotherapy has the potential to increase drug exposure in the lung, while limiting systemic side effects. However, the delivery of chemotherapeutic agents directly to the lung increases the risk of pulmonary toxicity that is not observed during systemic administration (Otterson *et al.*, 2007; Wittgen *et al.*, 2007; Gagnadoux *et* *al.*, 2008). In at least one clinical trial (Otterson *et al.*, 2007), pulmonary toxicity was dose-limiting. It is possible that improved targeting to localized disease sites, through technologies such as that described in the present thesis, will limit pulmonary toxicity by reducing exposure in healthy regions of the lung.

Inhaled chemotherapy may reach cancerous cells either through the local blood supply, or through direct, topical penetration of carcinomas (Gagnadoux *et al.*, 2008). With the latter mechanism in mind, bronchioloalveolar carcinoma (BAC), a lung cancer subtype that tends to spread along the walls of peripheral airways (Hodges and Kalemkerian, 2000), has been identified as a potential indication for inhaled chemotherapy (Gagnadoux *et al.*, 2008). The incidence of BAC relative to other types of lung cancer has increased substantially over the past several decades, with BAC comprising up to approximately 20% of total lung cancers as of 1990 (Aurebach and Garfinkel, 1991; Barsky *et al.*, 1994). Patients with BAC tend to be younger than those with other types of non-small-cell lung cancer (Hodges and Kalemkerian, 2000), and approximately one third are non-smokers (Osann, 1991; Barkley and Green, 1996). Barsky *et al.* (1994) reported that in 91.4% of the BAC patients they studied, tumors were confined to a single lobe of the lung, while only 2.8% of cases involved tumors in both the right and left lung. Furthermore, BAC appears to leave the underlying airway architecture relatively unobstructed (Jung *et al.*, 2001; Patsios *et al.*, 2007), so that affected lobes remain ventilated, at least to some extent. As such, the ability to target the delivery of inhaled chemotherapy to the peripheral airways of a specified lobe seems to be well suited for the treatment of BAC, either as a primary option, or as adjuvant therapy in combination with surgery or systemic chemotherapy.

One of the main challenges in developing aerosol systems for targeting by magnetic alignment will be in the formulation of desired drugs into the requisite high aspect ratio particle morphology. In many instances, it will likely be necessary to incorporate drug into a high aspect ratio carrier; however, paclitaxel was identified in chapter 5 of this thesis as a chemotherapeutic agent with a natural acicular crystal habit. Nebulized, solution formulations of paclitaxel have been explored for inhalation in the past (Hershey *et al.*, 1999; Koshkina *et al.*, 2001; Knight *et al.*, 2004). Hershey *et al.* (1999) observed tumor regression in some, but not all, dogs treated with inhaled paclitaxel, with no reported systemic or pulmonary toxicity, whereas occurrences of pulmonary toxicity were observed in dogs treated with inhaled doxorubicin. In addition, Koshkina *et al.* (2001) observed an antitumor effect in mice exposed to nebulized liposomal formulations of paclitaxel. While the paclitaxel crystals studied in chapter 5 were larger in diameter than is optimal for targeting by magnetic alignment, smaller diameter paclitaxel crystals have been prepared by rapid expansion of supercritical fluids (Yildiz *et al.*, 2007), and simply by diluting the commercial paclitaxel injection concentrate (Taxol; Bristol-Meyers Squibb, Princeton, NJ) in phosphate buffered saline (Szebeni *et al.*, 2001). In the latter case, sub-micrometer diameter paclitaxel crystals with lengths extending to tens of micrometers were observed in tenfold and fifteen-fold dilutions. Accordingly, there is some reason to be optimistic that it will be possible to develop formulations containing high aspect ratio paclitaxel particles of appropriate dimensions for optimal targeting by magnetic alignment.

In summary, the present thesis has detailed a novel approach for targeting inhaled pharmaceutical aerosols to localized regions of the lung. Such targeting is not possible using currently available aerosol delivery systems, and it is anticipated that localized targeting will be useful in treating diseases that tend to be confined to single lobes of the lung, as is the case for certain types of lung cancer. The approach relies on magnetic field alignment of elongated, high aspect ratio drug particles loaded with iron oxide nanoparticles. As the magnetic torque acting on a nonspherical particle depends on the magnetic field strength, and not the gradient in the field strength, magnetic alignment can be accomplished within the lung using uniform or low gradient fields produced by external sources.

Proof of concept experiments were performed in idealized physical replicas of the small, bifurcating airways found in the peripheral lung, and demonstrated enhanced deposition due to magnetic field alignment of model drug particles. In addition, the feasibility of measuring regional lung deposition of iron oxide nanoparticles using MRI was verified in mice exposed nose-only to nebulized droplets containing colloidal iron oxide, and in rabbits exposed intratracheally to iron oxide loaded, high aspect ratio drug particles. The combination of magnetic targeting with MRI deposition measurements is well suited for future studies in animal models or human patients. The ability to target inhaled pharmaceutical aerosols to specified regions of the lung would be a significant step forward in respiratory drug delivery, and would be particularly well suited for treatment of bronchioloalveolar carcinoma. It is anticipated that, through the methods presented in this thesis, such targeting will be possible. In addition, the ability to noninvasively quantify the level of targeting achieved in patients using MRI will be of considerable benefit in correlating deposition enhancement at targeted sites with clinical outcomes.

REFERENCES

Adair, RK. 1990. *The Physics of Baseball.* Harper-Collins Publishers, New York.

Allen, MD, and OG Raabe. 1985. Slip correction measurements of spherical solid aerosol particles in an improved Millikan apparatus. *Aerosol Sci. Technol.* 4: 269-286.

Ally, J, B Martin, MB Khamesee, W Roa, and A Amirfazli. 2005. Magnetic targeting of aerosol particles for cancer therapy. *J. Magn. Magn. Mat.* 293: 442-449.

Arnold JFT, Fidler F, Wang T, Pracht ED, Schmidt M, and Jakob PM. 2004. Imaging lung function using rapid dynamic acquisition of T_1-maps during oxygen enhancement. *MAGMA.* 16: 246-253.

Asgharian, B, and CP Yu. 1988. Deposition of inhaled fibrous particles in the human lung. *J. Aerosol Med.* 1: 37-50.

Asgharian, B, CP Yu, and L Gradon. 1988. Diffusion of fibers in a tubular flow. *Aerosol Sci. Tech.* 9: 213-219.

Asgharian B, and CP Yu. 1989. A simplified model of interceptional deposition of fibers at airway bifurcations. *Aerosol Sci. Tech.* 11: 80-88.

Aurebach, O, and L Garfinkel. 1991. The changing pattern of lung adenocarcinoma. *Cancer.* 68: 1973-1977.

Balashazy, I, TB Martonen, and W Hofmann. 1990. Fiber deposition in airway bifurcations. *J. Aerosol Med.* 3: 243-260.

Barkley, JE, and MR Green. 1996. Bronchioloalveolar carcinoma. *J. Clin. Oncol.* 14: 2377-2385.

Barsky, SH, R Cameron, KE Osann, D Tomita, and EC Holmes. 1994. Rising incidence of bronchioloalveolar carcinoma and its clinicopathological features. *Cancer.* 73: 1163-1170.

Bellin, M-F. 2006. MR contrast agents, the old and the new. *European Journal of Radiology.* 60(3): 314-323.

Bennett, WD, KL Zeman, and AM Jarabek. 2008. Nasal contribution to breathing and fine particle deposition in children versus adults. *J. Toxicol. Env. Health.* 71: 227-237.

Becquemin, MH, CP Yu, M Roy, and A Bouchikhi. 1991. Total deposition of inhaled particles related to age: comparison with age-dependent model calculations. *Radiation Protection Dosimetry.* 38: 23-28.

Brody, AR, LH Hill, B Adkins, and RW O'Connor. 1981. Chrysotile asbestos inhalation in rats: deposition pattern and reaction of alveolar epithelium and pulmonary macrophages. *Am. Rev. Respir. Dis.* 128: 670-679.

Brown, WF. 1962. *Magnetostatic principles in ferromagnetism.* North-Holland Publishing Company, Amsterdam.

Brown, RA, and LS Schanker. 1983. Absorption of aerosolized drugs from the rat lung. *Drug Metab. Dispos.* 11: 355–360.

Cai, FS, and CP Yu. 1988. Inertial and interceptional deposition of spherical particles and fibers in a bifurcating airway. *J. Aerosol Sci.* 19: 679-688.

Canadian Cancer Society/National Cancer Institute of Canada. 2007. *Canadian Cancer Statistics.* Toronto.

Chan, TL, and M Lippmann. 1980. Experimental measurement and empirical modeling of the regional deposition of inhaled particles in humans. *Am. Ind. Hyg. Assoc. J.* 41: 399-409.

Chan, HK, and I Gonda. 1989. Aerodynamic properties of elongated particles of cromoglycic acid. *J. Aerosol Sci.* 20: 157-168.

Cheng, FY, CH Su, YS Yang, CS Yeh, CY Tsai, CL Wu, MT Wu, and DB Shieh. (2005). Characterization of aqueous dispersions of Fe_3O_4 nanoparticles and their biomedical applications. *Biomaterials.* 26: 729-738.

Cheng, YS, SM Smith, HC Yeh, DB Kim, KH Cheng, and DL Swift. 1995. Deposition of ultrafine aerosols and thoron progeny in replicas of nasal airways of young children. *Aerosol Sci. Tech.* 23: 541-552.

Cheng, YS, QH Powell, SM Smith, and NF Johnson. 1995. Silicon carbide whiskers: characterization and aerodynamic behaviors. *Am. Ind. Hyg. Assoc. J.* 56: 970-978.

Chertok B, Moffat BA, David AE, Yu F, Bergemann C, Ross BD, and Yang VC. 2008. Iron oxide nanoparticles as a drug delivery vehicle for MRI monitored magnetic targeting of brain tumors. *Biomaterials.* 29: 487-496.

Chow, AHL, HHY Tong, P Chattopadhyay, and BY Shekunov. 2007. Particle engineering for pulmonary drug delivery. *Pharm. Res.* 24: 411-435.

Clark, DJ, and BJ Lipworth. 1997. Dose-response of inhaled drugs in asthma - An update. *Clinical Pharmacokinetics*. 32: 58-74.

Coates, AL. 2008. Guiding aerosol deposition in the lung. *New Engl. J. Med.* 358: 304-305.

Collazo, H, WA Crow, L Gardner, BL Phillips, VA Marple, and B Olson. 2002. Inertial impactor to measure aerodynamic diameters of man-made organic fibers. *Aerosol Sci. Tech.* 36: 166-177.

Coin, PG, VL Roggli, and AR Brody. 1992. Deposition, clearance, and translocation of chrysotile asbestos from peripheral and central regions of the lung. *Exp. Lung Res.* 58: 97-116.

Costa DL, Lehmann JR, Winsett D, Richards J, Ledbetter AD, and Dreher KL. 2006. Comparative pulmonary toxicological assessment of oil combustion particles following inhalation or instillation exposure. *Toxicological Sciences*. 91(1): 237-246.

Crowder, TM, JA Rosati, JD Schroeter, AJ Hickey, and TB Martonen. 2002. Fundamental effects of particle morphology on lung delivery: predictions of stokes' law and the particular relevance to dry powder inhaler formulation and development. *Pharm. Res.* 19: 239-245.

Crowe, C, M Sommerfeld, and Y Tsuji. 1998. *Multiphase Flows with Droplets and Particles*. CRC Press, Boca Raton, FL.

Crystal, RG. 1991. Alveolar macrophages. In, RG Crystal, and JB West (eds.). *The Lung: Scientific Foundations*. Raven Press, New York.

Dames, P, B Gleich, A Flemmer, K Hajek, N Seidl, F Wiekhorst, D Eberbeck, I Bittmann, C Bergemann, T Weyh, L Trahms, J Rosenecker, and C Rudolph. 2007. Targeted delivery of magnetic aerosol droplets to the lung. *Nature Nanotechnology*. 2: 495-499.

Darquenne, C, M Paiva, JB West, and GK Prisk. 1997. Effect of microgravity and hypergravity on deposition of 0.5- to 3-um-diameter aerosol in the human lung. *J. Appl. Physiol.* 83: 2029–2036.

Darquenne, C, and GK Prisk. 2004. Aerosol deposition in the human respiratory tract breathing air and 80:20 heliox. *J. Aerosol Med.* 17: 278–285

Dullien, FAL. 1997. Structural properties of packings of particles. In, ME Fayed, and L Otten (Eds.). *Handbook of Powder Science and Technology. 2nd Edition.* Chapman & Hall, New York.

Dobson, J. 2006. Magnetic nanoparticles for drug delivery. *Drug Dev. Res.* 67: 55-60.

Ehtezazi, T, KW Southern, D Allanson, I Jenkinson, and C O'Callaghan. 2005. Suitability of the upper airway models obtained from MRI studies in simulating drug lung deposition from inhalers. *Pharm. Res.* 22: 166-170.

Einstein, A. 1905. On the motion required by the molecular kinetic theory of heat of small particles suspended in a stationary liquid. *Annalen der Physik.*

Elliott, S. 1998. *The Physics and Chemistry of Solids.* John Wiley and Sons, Chichester, West Sussex, England. Pages 570-573.

Emmett, PC, RJ Aiken, and WJ Hannan. 1982. Measurement of the total and regional deposition of inhaled particles in the human respiratory tract. *J. Aerosol Sci.* 13: 549-560.

Falk R, Philipson K, Svartengren M, Bergmann R, Hofmann W, Jarvis N, Bailey M, and Camner P. 1999. Assesment of long-term bronchiolar clearance of particles from measurements of lung retention and theoretical estimates of regional deposition. *Exp. Lung Res.* 25: 495-516.

Findeisen, W. 1935. Uber das absetzen kleiner, in der luft suspendierter teilchen in der menschlichen lunge bei der atmung. *Arch. Ges. Phsiol.* 236: 367-379.

Finlay, WH, and KW Stapleton. 1995. The effect on regional lung deposition of coupled heat and mass transfer between hygroscopic droplets and their surrounding phase. *J. Aerosol Sci.* 26: 655-670.

Finlay, WH, KW Stapleton, HK Chan, P Zuberbuhler, and I Gonda. 1996. Regional deposition of inhaled hygroscopic aerosols: in vivo SPECT compared with mathematical modeling. *J. Appl. Physiol.* 81: 374-383.

Finlay, WH, CF Lange, M King, and D Speert. 2000. Lung delivery of aerosolized dextran. *Am. J. Respir. Crit. Care Med.* 161: 91-97.

Finlay, WH. 2001. *The Mechanics of Inhaled Pharmaceutical Aerosols.* Academic Press, London.

Finlay, WH. 2003. Lung deposition simulation. In: AJ Hickey (Ed.). *Pharmaceutical Inhalation Aerosol Technology, 2nd Edition.* Marcel Dekker, New York.

Finlay, WH, and AR Martin. 2008. Recent advances in predictive understanding of respiratory tract deposition. *J. Aerosol Med.* In press.

Fleming, JS, BP Epps, JH Conway, and TB Martonen. 2006. Comparison of SPECT aerosol deposition data with a human respiratory deposition model. *J. Aerosol Med.* 19: 268-278.

Foord, N, A Black, and M Walsh. 1978. Regional deposition of 2.5-7.5 μm diameter inhaled particles in healthy male non-smokers. *J. Aerosol. Sci.* 9: 323-357.

Fuchs, NA. 1964. *The Mechanics of Aerosols.* Dover Publications, New York.

Gagnadoux, F, J Hureaux, L Vecellio, T Urban, A Le Pape, I Valo, J Montharu, V Leblond, M Boisdron-celle, S Lerondel, C Majoral, P Diot, JL Racineux, and E Lemarie. 2008. Aerosolized chemotherapy. *J. Aerosol Med.* 21: 61-70.

Gallily, I, and AH Cohen. 1979. On the orderly nature of the motion of nonspherical aerosol particles. II. Inertial collision between a spherical large droplet and axially symmetrical elongated particle. *J. Colloid Interface Sci.* 68: 338-356.

Gans, KR. 1928. *Ann. Phys.* 86: 628-656.

Gormley, PG, and K Kennedy. 1949. Diffusion from a stream flowing through a cylindrical tube. *Proc. Roy. Irish Soc.* 52A: 163.

Grgic, B, AF Heenan, PKP Burnell, and WH Finlay. 2004. In vitro intersubject and intrasubject deposition measurements in realistic mouth-throat geometries. *J. Aerosol Sci.* 35: 1025-1040.

Griffiths, DJ. 1999. *Introduction to Electrodynamics. Third Edition.* Prentice Hall, Upper Saddle River, New Jersey.

Haefeli-Bleuer, B, and ER Weibel. 1988. Morphometry of the human pulmonary acinus. *Anatom. Rec.* 220: 401-424.

Haik, Y, J Chatterjee, and CJ Chen. 2005. *Alignment on carbon nanotubes using magnetic particles*. US Patent Application No. 20050239948.

Hammersley, JR, and DE Olson. 1992. Physical models of the smaller pulmonary airways. *J. Appl. Physiol.* 72: 2402-2414.

Happel, J, and H Brenner. 1965. *Low Reynolds Number Hydrodynamics*. Prentice-Hall, Englewood Cliffs, N.J.

Harris, RL. 1972. *A Model for Deposition of Microscopic Fibers in the Human Respiratory Tract*. PhD thesis, University of North Carolina.

Harris, RL, and DA Fraser. 1976. A model for the deposition of fibers in the human respiratory system. *Am. Ind. Hyg. Assoc. J.* 37: 73-89.

Haussermann, S, AG Bailey, MR Bailey, G Etherington, M Youngman. 2002. The influence of breathing patterns on particle deposition in a nasal replicate cast. *J. Aerosol Sci.* 33: 923-933.

Hershey, AE, ID Kurzman, LJ Forrest, CA Bohling, M Stonerook, ME Placke, AR Imondi, and DM Vail. 1999. Inhalation chemotherapy for macroscopic primary or metastatic lung tumors: proof of principle using dogs with spontaneously occurring tumors as a model. *Clin. Cancer Res.* 5: 2653-2659.

Heyder, J, and J Gebhart. 1977. Gravitational deposition of particles from laminar aerosol flow through inclined cylindrical tubes. *J. Aerosol Sci.* 8: 289-295.

Heyder, J, J Gebhart, G Rudolf, CF Schiller, and W Stahlhofen. 1986. Deposition of particles in the human respiratory tract in the size range 0.005–15 μm. *J. Aerosol Sci.* 17:811–825.

Hinds, WC. 1999. *Aerosol Technology.* John Wiley & Sons, New York.

Hodges CM, and GP Kalemkerian. 2000. Bronchioloalveolar carcinoma masquerading as pneumonia. *Primary Care and Cancer.* 20. 7.

Horsfield K, and G Cumming. 1967. Angles branching and diameters of branches in the human bronchial tree. *Bull. Math Biophys.* 29: 245-259.

Horsfield, K, Dart, G, Olson DE, Filley, GF, Cumming, G. 1971. Models of the human bronchial tree. *J. Appl. Physiol.* 31: 207-217.

Hou, Y, J Yu, and S Gao. 2003. Solvothermal reduction synthesis and characterization of superparamagnetic magnetite nanoparticles. *J. Mater. Chem.* 13: 1983-1987.

Ikegami, K, Y Kawashima, H Takeuchi, H Yamamoto, N Isshiki, D Momose, and K Ouchi. 2002. *Pharm. Res.* 19: 1439-1445.

International Commission on Radiological Protection (ICRP). 1994. ICRP publication 66: human respiratory tract model for radiological protection. *Annals of the ICRP.* 24.

Israel, E. 2000. Assessment of therapeutic index of inhaled steroids. *The Lancet.* 356: 527-528.

Jeffery, GB. 1922. The motion of ellipsoidal particles immersed in a viscous fluid. *Proc. Roy. Soc. Lond.* A102: 161-179.

Johnson, DL, and TB Martonen. 1994. Behavior of inhaled fibers: potential application to medicinal aerosols. *Part. Sci. Technol.* 12: 161-173.

Jung, JI, H Kim, SH Park, HH Kim, MI Ahn, HS Kim, *et al.* 2001. CT differentiation of pneumonic-type bronchioloalveolar cell carcinoma and infectious pneumonia. *Br. J. Radiol.* 74: 490-494.

Kelly, JT, B Asgharian, JS Kimbell, and BA Wong. 2004. Particle deposition in human nasal airway replicas manufactured by different methods. Part I: Inertial regime particles. *Aerosol Sci. Tech.* 38: 1063-1071.

Kim, CS, and TC Kang. 1997. Comparative measurement of lung deposition of inhaled fine particles in normal subjects and patients with obstructive airway disease. *Am. J. Respir. Crit. Care Med.* 155: 899-905.

Kim, CS, and PA Jaques. 2004. Analysis of total respiratory deposition of inhaled ultrafine particles in adult subjects at various breathing patterns. *Aerosol Sci. Tech.* 38:525–540.

Kim, CS, and PA Jaques. 2005. Total lung deposition of ultrafine particles in elderly subjects during controlled breathing. *Inhalation Toxicology*. 17: 387–399.

Kim, CS and SC Hu. 2006. Total respiratory tract deposition of fine micrometer-sized particles in healthy adults: Empirical equations for gender and breathing pattern. *J. Appl. Physiol.* 101:401–412.

Kim, JY, FE Osterloh, H Hiramatsu, RK Dumas, and K Liu. 2005. Synthesis and real-time magnetic manipulation of a biaxial superparamagnetic colloid. *J. Phys. Chem. B.* 109: 11151-11157.

Knight, V, NV Koshkina, E Golunski, LE Roberts, and BE Gilbert. 2004. Cyclosporin A aerosol improves the anticancer effect of paclitaxel aerosol in mice. *Trans. Am. Clin. Climatol. Assoc.* 115: 395-404.

Kohler, E, V Sollich, R Schuser-Wonka, and G Jorch. 2005. Lung deposition after electronically breath-controlled inhalation and manually triggered conventional inhalation in cystic fibrosis patients. *J. Aerosol Med.* 18: 386-395.

Koshkina NV, JC Waldrep, LE Roberts, E Golunski, S Melton, and V Knight. 2001. Paclitaxel liposome aerosol treatment induces inhibition of pulmonary metastases in murine renal carcinoma model. *Clin. Cancer Res.* 7: 3258-3262.

Labiris, NR, and MB Dolovich. 2003. Pulmonary drug delivery. Part I: Physiological factors affecting therapeutic effectiveness of aerosolized medications. *Br. J. Clin. Pharmacol.* 56: 588-599.

Landahl, HD. 1950. On the removal of airborne droplets by the human respiratory tract. I. The lung. *Bull. Math. Biopys.* 12: 43-56.

Larhrib, H, GP Martin, C Marriott, and D Prime. 2003. The influence of carrier and drug morphology on drug delivery from dry powder formulations. *Int. J. Pharm.* 257: 283-296.

Lemke A-J, von Pilsach MIS, Lubbe A, Bergemann C, Riess H, and Felix R. 2004. MRI after magnetic drug targeting in patients with advanced solid malignant tumors. *Eur. Radiol.* 14: 1949-1955.

Lindstrom M, Camner P, Falk R, Hjelte L, Philipson K, and Svartengren M. 2005. Long-term clearance from small airways in patients with cystic fibrosis. *Eur. Respir. J.* 25: 317-323.

Lippmann, M. 1977. Regional deposition of particles in the human respiratory tract. In, Lee DHK *et al.* (eds.). *Hanbook of Physiology – Reaction to Environmental Agents.* American Physiological Society, Bethesda, MD. 213-232.

Liu, Y, EA Matida, J Gu, and MR Johnson. 2007. Numerical simulation of aerosol deposition in a 3-D human nasal cavity using RANS, RANS/EIM, and LES. *J. Aerosol. Sci.* 38: 683-700.

Lombry, C, DA Edwards, V Preat, and R Vanbever. 2004. Alveolar macrophages are a primary barrier to pulmonary absorption of macromolecules. *Am. J. Phsiol. Cell Mol. Physiol.* 286: L1002-L1008.

Martin, AR. 2004. *The Effect of Humidity on Aerosol Drug Delivery from Metered-Dose Inhalers.* M.Sc. Thesis. University of Alberta. Edmonton, Alberta, Canada.

Martin, AR, and Finlay, WH. 2007. A general, algebraic equation for predicting total respiratory tract deposition of micrometer-sized aerosol particles in humans. *J. Aerosol Sci.* 38: 246-253.

McCaig, M, and AG Clegg. 1987. *Permanent Magnets in Theory and Practice.* Pentech Press, London.

Mendelsohn, LI, FE Luborsky, and TO Paine. 1955. Permanent-magnet properties of elongated single-domain iron particles. *J. Appl. Phys.* 26: 1274-1280.

Möller W, Häubinger K, Winkler-Heil R, Stahlhofen W, Meyer T, Hofmann W, and Heyder J. 2004. Mucociliary and long-term particle clearance in the airways of healthy nonsmoker subjects. *J. Appl. Physiol.* 97: 2200-2206.

Möller W, Häubinger K, Ziegler-Heitbrock L, and Heyder J. 2006. Mucociliary and long-term particle clearance in airways of patients with immotile cilia. *Respiratory Research.* 7: 10.

Moolgavkar, SH, RC Brown, and J Turim. 2001. Biopersistence, fiber length, and cancer risk assessment for inhaled fibers. *Inhalation Toxicol.* 13: 755-772.

Morgan, A, A Black, N Evans, A Holmes, and JN Pritchard. 1980. Deposition of sized glass fibers in the respiratory tract of the rat. *Ann. Occup. Hyg.* 23: 353-366.

Mosbach, K, and U Schröder. 1979. Preparation and application of magnetic polymers for targeting of drugs. *FEBS Lett.* 102: 112-116.

Myojo, T. 1987. Deposition of fibrous aerosol in model bifurcating tubes. *J. Aerosol Sci.* 18: 337-347.

Myojo, T. 1990. The effect of length and diameter on the deposition of fibrous aerosol in a model lung bifurcation. *J. Aerosol Sci.* 21: 651-659.

Myojo, T. 1997. Deposition of fibrous aerosol in a model of a human lung bifurcation under cyclic flow conditions. *Ann. Occup. Hyg.* 41, Suppl. 1: 142-147.

Myojo, T, and M Takaya. 2001. Estimation of fibrous aerosol deposition in upper bronchi based on experimental data with model bifurcation. *Industrial Health.* 39: 141-149.

Nadithe V, Rahamatalla M, Finlay WH, Mercer JR, and Samuel J. 2003. Evaluation of nose-only aerosol inhalation chamber and comparison of experimental results with mathematical simulation of aerosol deposition in mouse lungs. *J. Pharm. Sci.* 92: 1066-1076.

Nichols, SC, DR Brown, and M Smurthwaite. 1998. New concept for the variable flow rate Andersen cascade impactor and calibration data. *J. Aerosol Med.* 11: S133-S138.

Nielsen, KG, M Skov, B Klug, M Ifversen, and H Bisgaard. 1997. Flow-dependent effect of formoterol dry-powder inhaled from the Aerolizer. *Eur. Respir. J.* 10: 2105-2109.

Olson, DE. 1971. *Fluid mechanics relevant to respiration – flow within curved or elliptical tubes and bifurcating systems.* PhD thesis, Imperial College.

Osann, KE. 1991. Lung cancer in women: the importance of smoking, family history of cancer and medical history of respiratory disease. *Cancer Research.* 51: 4893-4897.

Osborn, JA. 1945. Demagnetizing factors of the general ellipsoid. *Phys. Rev.* 67: 351-357.

Osterloh, FE, H Hiramatsu, RK Dumas, and K Liu. 2005. Fe_3O_4-$LiMo_3Se_3$ nanoparticle clusters as superparamagnetic nanocompasses. *Langmuir.* 21: 9709-9713.

Otterson, GA, MA Villalona-Calero, S Sharma, MG Kris, A Imondi, M Gerber, DA White, MJ Ratain, JH Schiller, A Sandler, M Kraut, S Mani, and JR Murren. 2007. Phase 1 study of inhaled doxorubicin for patients with metastatic tumors to the lungs. *Clin. Cancer Res.* 13:1246-1252.

Oyabu, T, H Yamato, A Ogami, Y Morimoto, I Akiyama, S Ishimatsu, H Hori, and I Tanaka. 2004. *J. Occup. Health.* 46: 382-390.

Patsios, D, HC Roberts, NS Paul, T Chung, SJ Herman, A Pereira, and G Weisbrod. 2007. Pictorial review of the many faces of bronchioloalveolar cell carcinoma. *Br. J. Radiol.* 80: 1015-1023.

Patton JS, and PR Byron. 2007. Inhaling medicines: delivering drugs to the body through the lungs. *Nature Reviews Drug Discovery.* 6: 67-74.

Phillips CG, SR Kaye, and RC Schroter. 1994. A diameter-based reconstruction of the branching pattern of the human bronchial tree. *Respir. Physiol.* 98: 193-217.

Plank C. 2008. Nanomagnetosols: magnetism opens up new perspectives for targeted aerosol delivery to the lung. *Trends in Biotechnology.* 26 (2): 59-63.

Platek, SF, Riley, RD, and Simon, SD. 1992. The classification of asbestos fibres by scanning electron microscopy and computer digitizing tablet. *Ann. Occup. Hyg.* 36: 155-171.

Prodi, V, DT Zaiacomo, D Hochrainer, and K Spurny. 1982. Fibre collection and measurement with the inertial spectrometer. *J. Aerosol Sci.* 13: 49-58.

Rader, DJ. 1990. Momentum slip correction factor for small particles in nine common gases. *J. Aerosol Sci.* 21: 161-168.

Riganakos, KA, and PG Veltsistas. 2003. Comparative spectrophotometric determination of the total iron content in various white and red Greek wines. *Food Chem.* 82: 637-643.

Robinson, RJ, MJ Oldham, RE Clinkenbeard, and P Rai. 2006. Experimental and numerical smoke carcinogen deposition in a multi-generation human replica tracheobronchial model. *Ann. Biomed. Eng.* 34: 373-383.

Rosenthal SG, Willich HC, Ebert W, and Conrad J. 1993. The demonstration of human tumors on nude mice using gadolinium-labeled monoclonal antibodies for magnetic resonance imaging. *Invest. Radiol.* 28: 789-793.

Rudolf, G, R Kobrich, and W Stahlhofen. 1990. Modelling and algebraic formulation of regional and aerosol deposition in man. *J. Aerosol Sci.* 21, Suppl. 1: S403-S406.

Sauret, V, Halson, PM, Brown, IW, Fleming, JS, and Bailey, AG. 2002. Study of the three-dimensional geometry of the central conducting airways in man using computer tomographic (CT) images. *J. Anat.* 200: 123-134.

Schanker, LS, EW Mitchell, and RA Brown. 1986. Species comparison of drug absorption from the lung after aerosol inhalation or intratracheal injection. *Drug Metab. Dispos.* 14: 79–88.

Schiller-Scotland, CHF, R Hlawa, J Gebhart, R Wönne, and J Heyder. 1992. Total deposition of aerosol particles in the respiratory tract of children during spontaneous and controlled mouth breathing. *J. Aerosol Sci.* 23 (Suppl. 1): S457–S460.

Senyei, A, Widder K, and Czerlinski, C. 1978. Magnetic guidance of drug carrying microspheres. *J. Appl. Phys.* 49: 3578-3583.

Shang, YH, Finlay, WH, and Moussa, WA. 2008. Numerical analysis of thermally induced micro fiber deformation using a high frequency magnetic field in human lung. *J. Comp. Theor. Nanosci.* 5: 294–301.

Shevchenko, IT, and GE Resnik. 1968. Inhalation of chemical substances and oxygen in radiotherapy of bronchial cancer. *Neoplasma.* 15: 419-426.

Shine, AD, and RC Armstrong. 1987. The rotation of a suspended axisymmetric ellipsoid in a magnetic field. *Rheol. Acta.* 26: 152-161.

Skomski, R, and JMD Coey. 1999. *Permanent Magnetism.* Institute of Physics Publishing, Bristol and Philadelphia.

Skomski, R, GC Hadjipanayis, and DJ Sellmyer. 2007. Effective demagnetizing factors of complicated particle mixtures. *IEEE Trans. Magn.* 43: 2956-2958.

Sosnowski, TR, A Moskal, and L Gradon. 2006. Dynamics of oropharyngeal aerosol transport and deposition with the realistic flow pattern. *Inhal. Toxicol.* 18: 773-780.

Stadler A, PM Jakob, M Griswold, M Barth, and AA Bankier. 2005. T_1 mapping of the entire lung parenchyma: influence of respiratory phase in healthy individuals. *J. Magn. Reson. Imaging.* 21: 759-764.

Stadler A, PM Jakob, M Griswold, L Stiebellehner, M Barth, and AA Bankier. 2008. T_1 mapping of the entire lung parenchyma: Influence of respiratory phase and correlation to lung function test results in patients with diffuse lung disease. *Magn. Reson. Med.* 59: 96-101.

Stahlhofen, W, J Gebhart, and J Heyder. 1980. Experimental determination of the regional deposition of aerosol particles in the human respiratory tract. *Am. Ind. Hyg. Assoc. J.* 41: 385-395.

Stahlhofen, W, J Gebhart, and J Heyder. 1981. Biological variability of regional deposition of aerosol particles in the human respiratory tract. *Am. Ind. Hyg. Assoc. J.* 42: 348-352.

Stahlhofen, W, J Gebhart, J Heyder, and G Scheuch. 1983. New regional deposition data of the human respiratory tract. *J. Aerosol Sci.* 14: 186-188.

Stahlhofen, W, G Rudolf, and AC James. 1989. Intercomparison of experimental regional aerosol deposition data. *J. Aerosol Med.* 2: 285-308.

Stapleton, KW, E Guentsch, MK Hoskinson, and WH Finlay. 2000. On the suitability of k-ω turbulence modeling for aerosol deposition in the mouth and throat: A comparison with experiment. *J. Aerosol Sci.* 31: 739–749.

Stokes, GG. 1851. *Trans. Cambridge Phil. Soc.* 9: 8.

Sussman, RG, BS Cohen, and M Lippmann. 1991. Asbestos fiber deposition in a human tracheobronchial cast. I. Experimental. *Inhal. Toxicol.* 3: 145-160.

Suwa T, Ozawa S, Ueda M, Ando N, and Kitajima M. 1998. Magnetic resonance imaging of esophageal squamous cell carcinoma using magnetite particles coated with anti-epidermal growth factor receptor antibody. *Int. J. Cancer.* 75: 626-634.

Swift, DL. 1996. Use of mathematical aerosol deposition models in predicting the distribution of inhaled therapeutic aerosols. In: AJ Hickey (Ed.). *Inhalation Aerosols*. Marcel Dekker, New York.

Szebeni, J, CR Alving, S Savay, Y Barenholz, A Priev, D Danino, and Y Talmon. 2001. Formation of complement-activating particles in aqueous solutions of Taxol: possible role in hypersensitivity reactions. *Int. Immunopharmacol.* 1: 721-735.

Tatsumura, T, S Koyama, M Tsujimoto, M Kitagawa, and S Kagamimori. 1993. Further study of nebulisation chemotherapy, a new chemotherapeutic method in the treatment of lung carcinomas: fundamental and clinical. *Br. J. Cancer*. 68: 1146-1149.

Timbrell, V, and JW Skidmore. 1971. The effect of shape on particle penetration and retention in animal lungs. In: WH Walton (Ed.). *Inhaled Particles III*. Unwin, Old Woking, Surrey.

Timbrell, V. 1972. Alignment of carbon and other man-made fibers by magnetic fields. *J. Appl. Phys.* 43: 4839-4840.

Timbrell, V. 1982. Deposition and retention of fibers in the human lung. *Ann. Occup. Hyg.* 26: 347-369.

Van Dyke, R, and K Nikander. 2007. Delivery of iloprost inhalation solution with HaloLite, Prodose, and I-Neb adaptive aerosol delivery systems: an in vitro study. *Respir Care*. 52: 184–190.

Verschraegen CF, BE Gilbert, AJ Huaringa, R Newman, N Harris, FJ Leyva, L Keus, K Campbell, T Nelson-Taylor, and V Knight. 2000. Feasibility, phase I, and pharmacological study of aerosolized liposomal 9-nitro-20(S)-camptothecin in patients with advanced malignancies in the lungs. *Ann. N.Y. Acad. Sci.* 922: 352-354.

Verschraegen CF, BE Gilbert, E Loyer, A Huaringa, G Walsh, RA Newman, and V Knight. 2004. Clinical evaluation of the delivery and safety of aerosolized liposomal 9-nitro-20(S)-camptothecin in patients with advanced pulmonary malignancies. *Clin. Cancer Res.* 10: 2319-2326.

Wang, ZL, B Grgic, and WH Finlay. 2006. A dry powder inhaler with reduced mouth-throat deposition. *J. Aerosol Med.* 19: 168-174.

Weibel ER. 1963. *Morphometry of the Human Lung*. Academic Press, New York.

Weinmann H-J, Ebert W, Misselwitz B, and Schmitt-Willich H. 2003. Tissure-specific MR contrast agents. *European Journal of Radiology*. 46(1): 33-44.

Widder, KJ, Senyei, AE, and Scarpelli, DG. 1978. Magnetic microspheres: a model system for site specific drug delivery in vivo. *Proc. Soc. Exp. Biol. Med.* 58: 141-146.

Wilson BW, and Saffer JD. 1995. Extremely low frequency electromagnetic fields and cancer. In, Acros JC (Ed.), *Chemical Induction of Cancer: Modulation and Combination Effects*. Birkhauser, Boston.

Willeke, K, and PA Baron. 1993. *Aerosol Measurement*. Van Nostrand Reinhold, New York.

Wittgen, BPH, PWA Kunst, K van der Born, AW van Wijk, W Perkins, FG Pilkiewicz, R Perez-Soler, S Nicholson, GJ Peters, and PE Postmus. 2007. Phase 1 study of aerosolized SLIT cisplatin in the treatment of patients with carcinoma of the lung. *Clin. Cancer Res.* 13: 2414-2421.

Woodward, RM, ML Brown, ST Stewart, KA Cronin, and DM Cutler. 2007. The value of medical interventions for lung cancer in the elderly. *Cancer*. 110: 2511-2518.

Xi, J, and PW Longest. 2007. Effects of oral airway geometry on the diffusional deposition of inhaled nanoparticles. *ASME J. Biomech. Eng.*

Yeh, HC, RF Phalen, and OG Raabe. 1976. Factors influencing the deposition of inhaled particles. *Environ. Health Perspect.* 15: 147-156.

Yildiz N, S Tuna, O Doker, and A Calimili. 2007. Micronization of salicylic acid and taxol (paclitaxel) by rapid expansion of supercritical fluids (RESS). *J. Supercritical Fluids.* 41: 440-451.

Yu, CP, B Ashgharian, and BM Yen. 1986. Impaction and sedimentation deposition of fibers in airways. *Am. Ind. Hyg. Assoc. J.* 47: 72-77.

Yu, CP, L Zhang, MH Becquemin, M Roy, and A Bouchiki. 1992. Algebraic modeling of total and regional deposition of inhaled particles in the human lung of various ages. *J. Aerosol Sci.* 23: 73-79.

Zamankhan, P, G Ahmadi, Z Wang, PK Hopke, YS Cheng, WC Su, and D Leonard. 2006. Airflow and deposition of nano-particles in a human nasal cavity. *Aerosol Sci. Tech.* 40: 463-476.

Zanen, P, and BL Laube. 2002. Targeting the lungs with therapeutic aerosols. In, H Bisgaard, C O'Callaghan, and GC Smaldone (eds.). *Drug Delivery to the Lungs.* Marcel Dekker, New York.

Zauscher, S, and PE Humphrey. 1997 . Orienting lignocellulosic fibers and particles by means of a magnetic field. *Wood and Fiber Sci.* 29: 35-46.

Zeng, XM, GP Martin, C Marriott, and J Pritchard. 2000. The influence of carrier morphology on drug delivery by dry powder inhalers. *Int. J. Pharm.* 200: 93-106.

Zhang, H, G Ahmadi, FG Fan, and JB McLaughlin. 2001. Ellipsoidal particles transport and deposition in turbulent channel flows. *Int. J. Multiphase Flow.* 27: 971-1009.

Zhang, Y, WH and Finlay. 2005. Measurement of the effect of cartilaginous rings on particle deposition in a proximal lung bifurcation replica. *Aerosol Sci. Tech.* 39:394-399.

Zhang, Y, K Gilbertson, and WH Finlay. 2007. In vivo-in vitro comparison of deposition in three mouth-throat models with Qvar® and Turbuhaler® inhalers. *J. Aerosol Med.* 20: 227-235.

Zhou, Y, and YS Cheng. 2005. Particle deposition in a cast of human tracheobronchial airways. *Aerosol Sci. Tech.* 39: 492-500.